



REPORT

Modelling and Analysis of KSMMA - Induced Seismic Events to Advance Event Mitigation Strategies

Submitted to:

BC Oil & Gas Research & Innovation Society

PO Box 9331 – Stn Prov Govt
Victoria BC V8W 9N3

Attn.: Ines Piccinino – OGRIS Fund Manager

Submitted by:

WSP Canada Inc.

Suite 200 - 2920 Virtual Way, Vancouver BC V5M 0C4 Canada

+1 604 296 4200

Reference No. 2252864-005-R-Rev0-1000

12 May 2023



Distribution List

Electronic copy – BC Oil & Gas Research & Innovation Society

Electronic copy – WSP Canada Inc.

Executive Summary

When pressurized fluid is injected into deep reservoirs during hydraulic fracturing, the effective stresses on faults and other structures can change. This may result in slip, which in turn can release energy as seismic events. The project described in this document (led by WSP alongside the University of British Columbia [UBC]), has assessed this process by considering the following components that collectively induce a seismic event: the injection of high-pressure fluid; the pathway for fluid and pressure to migrate; the stresses and pore pressures in the surrounding regions; and the faults that may be reactivated. To date, most research into Induced Seismicity (IS) has not fully considered the well completions and the connectivity of the well to the reservoir. Access to three high-quality Montney Formation data sets from within KSMMA enabled a multi-faceted examination into the causes of IS, more than has been typically possible before.

The analysis had three main objectives:

- Interpret, characterize, and model the geometry of inferred, reservoir-scale, geological structures and the nature of their connectivity from the two drill pads.
- Analyze and model fracture pathway geometries and hydraulic data to: (a) constrain possible hydraulic properties of structures, and (b) to understand their role in pressure communication and seismic event triggering.
- Build upon the objectives above with numerical simulations to suggest possible operational mitigation methods that could help reduce IS events.

The results are briefly summarised below.

Structural Connectivity

Both of the drill pads studied show strong evidence of intersecting reservoir scale structures with strike lengths of 10s to 100s of meters. These populations exhibit Power Law distributions and the height of structures was variable. Some structures are strata-bound within their host Montney Formation. Other structures seem to extend from the Upper Montney to the Lower Montney formations. Injection into the Upper Montney Formation (in Operation 1) results in the generation of IS events down in the Lower Montney Formation. This challenges the perception that the Upper Montney Formation is less prone to seismicity and isolated from the Lower Montney.

The dominant strike orientation of inferred, seismically active, geological structures is NE-SW. Both the analysis of IS event to stage connection pathways and the stochastic simulations of reservoir structures support the presence of aseismic structures that result in a higher level of connectivity. It is thought that these structures have natural permeability that isn't dependent on stimulation.

Hydraulic Diffusivity and Pathway Properties

The IS events were analyzed to determine their straight-line distance from an active stage and the time taken for a triggering pressure to arrive at that location. This was to determine the hydraulic diffusivity of that pathway, to in turn provide insight into the dynamic characteristics of reservoir scale fractures within the Montney Formation. Diffusivity inferred fracture transmissivities are found to be in the 10s-100s mD.m range, with peak values in the order of 1000 mD.m. The range of hydraulic diffusivity values calculated are consistent with those reported from observed fracture connections elsewhere. The largest events were typically associated with fewer apparent fluid migration pathways and higher diffusivity values. This is consistent with the envisaged effect of rapid pressure diffusion along a small number of geological structures, resulting in a greater chance of triggering a larger event. Where more fluid migration pathways were inferred, fewer IS events were recorded.

Analysis of seismic energy efficiency (the ratio between cumulative seismic energy release and the input of hydraulic energy) in hydraulic fracture operations is typically less than 10^{-5} . However, the data from both operating companies showed seismic energy efficiency values in the range of 10^{-4} to 10^{-3} (10 to 100 times higher). These higher values are within the range reported for hydro-shearing associated with pressurized fluid injection that specifically targets pre-existing geological structures. Hydraulic fracture simulations (using Fracman software) suggest that hydroshearing is the most likely mechanism to cause IS. Additionally, the hydraulic fracture simulations indicated that the nature of any induced fracture is strongly controlled by the stresses and stiffnesses of the input layer. Depending on whether fluid was injected into a low stress or high stress layer, the result could be a long (strike) and short (height) fracture with limited pressure leakage, or a short (strike) and tall (height) fracture that propagates through, and directly connects, several geological rock formations.

Potential Mitigation Methods

Stochastic DFN simulations were used to test whether open hole or cased hole completions resulted in increased connectivity to the wider reservoir structures. These results showed that with the system as modelled, it was the frac length, rather than completion that controlled connectivity. However, it was found that switching from open hole to cased completions, effectively stopped any direct connection of the well to reservoir structures. Simulations indicated that the three Lower Montney wells on the Operator 3 pad, connected on average to ~12 structures. Switching to cased hole effectively stops this direct connection between the well and structures.

What this study has shown is that much of the induced seismicity observed is consistent with having been triggered by pressure diffusion through a partially connected network of structures. Failure to capture this aspect of the system into other numerical simulations or analysis, will not adequately represent the Montney hydraulic system. Whilst there are a lot of natural structures presumed present on both the OP1 and OP3 pads, it seems that only a relatively small percentage of these structures appeared to have orientations that resulted in them being inflated under injection conditions and providing a potential positive impact on production. The majority of structures that were stimulated resulted in hydroshearing only. Whilst this might provide some positive permeability increase, it is certainly not as productive as proppant receiving inflated fractures.

The geometry of a hydraulic fracture, connecting to a small number of fractures where a large seismic event was observed, was built in the numerical simulation software XSite. Initially the conditions for the original seismic event were reasonably matched and then a number of potential mitigation options were tested, and the resultant seismicity considered:

- **Injection Rate:** Numerical simulation studies suggest that higher injection rates can result in higher induced events magnitude. Lowering the injection rate can instead cause the seismic moment release in the form of many small events.
- **Variable Injection Rate:** Numerical modeling shows that varying the pumping rate during the injection resulted in a larger seismic energy release. However, this is more likely due to consequent pressure pulses. Such injection rate alteration and pressure pulses are more common during open hole completion.
- **Pressurisation Rate:** Simulation analyses revealed that the pressurization rate of the fracture showed a significant impact on the seismicity response of the reservoir. This agrees with the laboratory studies and numerical simulation studies of the water impoundment induced seismicity.
- **Fluid Viscosity:** Numerical simulation of increasing frac fluid viscosity showed a favourable reduction in the amount of seismicity relative to the base case. However, the modelling formulation is not 100% correct and needs further examination.

Future work will test these mitigation strategies further, with a view to the reduction of seismicity in the BC KSMMA.

Study Limitations

WSP Canada Inc. (WSP) has prepared this document in a manner consistent with that level of care and skill ordinarily exercised by members of the engineering and science professions currently practising under similar conditions in the jurisdiction in which the services are provided, subject to the time limits and physical constraints applicable to this document. No warranty, express or implied, is made.

This document, including all text, data, tables, plans, figures, drawings and other documents contained herein, has been prepared by WSP for the sole benefit of BC Oil & Gas Research & Innovation Society (BCOGRIS). It represents WSP's professional judgement based on the knowledge and information available at the time of completion. WSP is not responsible for any unauthorized use or modification of this document. All third parties relying on this document do so at their own risk.

The factual data, interpretations, suggestions, recommendations and opinions expressed in this document pertain to the specific project, site conditions, design objective, development and purpose described to WSP by BCOGRIS, and are not applicable to any other project or site location. In order to properly understand the factual data, interpretations, suggestions, recommendations and opinions expressed in this document, reference must be made to the entire document.

This document, including all text, data, tables, plans, figures, drawings and other documents contained herein, as well as all electronic media prepared by WSP are considered its professional work product and shall remain the copyright property of WSP. BCOGRIS may make copies of the document in such quantities as are reasonably necessary for those parties conducting business specifically related to the subject of this document or in support of or in response to regulatory inquiries and proceedings. Electronic media is susceptible to unauthorized modification, deterioration and incompatibility and therefore no party can rely solely on the electronic media versions of this document.

Acknowledgements

This work wouldn't have been possible without the support of BC OGRIS and the generous donation of subsurface data by several Montney operators. Additionally, we would like to acknowledge the technical support and feedback from the BC Oil and Gas Commission (now the BC Energy Regulator).

Table of Contents

STUDY LIMITATIONS.....	iv
1.0 INTRODUCTION	1
2.0 SUBSURFACE DATA SETS	3
2.1 Introduction.....	3
2.2 Operator 1 Data Set Summary.....	4
2.3 Operator 3 Data Set Summary.....	7
2.4 Summary of Induced Seismicity Data Sets.....	10
3.0 MAPPING STRUCTURAL CONNECTIVITY	11
3.1 Introduction.....	11
3.2 Stochastic Simulation of Induced Events.....	12
3.2.1 Introduction	12
3.2.2 Characterising the Geometry of Connected Montney Structures	14
3.2.2.1 Introduction	14
3.2.2.2 Orientation Definition	14
3.2.2.3 Structural Size Definition.....	16
3.2.2.4 Building a DFN Description of the Montney Structures	17
3.2.2.5 Geomechanics Scheme.....	19
3.2.2.6 Identifying Connected Seismically Active Structures.....	19
3.2.2.7 Calibration/Validation of the DFN Model.....	20
3.2.3 Discussion.....	22
3.3 Characterisation of Montney Structures through Interpretation of Induced Seismic Lineaments.....	22
3.3.1 Introduction	22
3.3.2 Mapping of Deterministic Structures	23
3.3.3 Characterisation of Smaller Scale Structures	28
3.3.3.1 Introduction	28
3.3.3.2 Structural Size Distribution.....	28
3.3.3.3 Orientation Distribution	29

3.3.3.4	Intensity Definition.....	30
3.3.4	Summary.....	31
3.4	Reproduction of Induced Seismicity Patterns using Connectivity Analysis	31
3.4.1	Introduction	31
3.4.2	Connectivity Analysis	31
3.4.3	Summary.....	36
4.0	CHARACTERISATION OF PATHWAY PROPERTIES BY HYDRAULIC DIFFUSIVITY	37
4.1	Introduction.....	37
4.2	Hydraulic Diffusivity Analysis – OP3 (Open Hole Completion)	39
4.3	Hydraulic Diffusivity Analysis – OP1 (Cased Hole Completion)	46
4.4	Synthesis.....	52
5.0	NUMERICAL SIMULATION OF HYDRAULIC FRACTURING AND INDUCED EVENTS	57
5.1	Introduction.....	57
5.2	Hydraulic fracture Simulations – OP1	58
5.2.1	Model Set Up	58
5.2.2	Modelling Results.....	60
5.2.2.1	Frac Shape	60
5.2.2.2	Frac Length.....	62
5.2.2.3	Interaction with existing structures.....	63
5.2.2.4	Hydro-shearing structures.....	65
5.3	FracMan Simulation of Hydraulic Fracture Operations – OP3.....	67
6.0	ANALYSIS TO SUPPORT EVENT MITIGATION	70
6.1	Stochastic simulation to Test Completion Styles	70
6.2	Numerical Simulation of Hydraulic Diffusivity.....	72
6.2.1	Hydraulic Diffusivity of a Single Fracture (FracMan Hydraulic Model)	72
6.2.2	Fracture Intensity Impact on Hydraulic Diffusivity Modelling (XSite™).....	73
6.2.2.1	Model set up	73
6.2.2.2	Results and Discussion.....	75
6.3	Simulation studies of potential mitigation strategies	78

6.3.1	The Impact of Injection Rate Ramp-up on Seismicity	78
6.3.2	Impact of Alternating Injection Rates on Seismicity	80
6.3.3	Model Calibration of Stage 12 of OP3 Well A2	83
6.3.4	The Impact of Pressurisation Rate on Seismicity	88
6.3.5	The Impact of Fluid Viscosity on Seismicity	91
7.0	KEY LEARNINGS & CONCLUSIONS	96
8.0	RECOMMENDATIONS FOR FUTURE WORK	100
9.0	CLOSURE	101
9.1	Collaboration	101
REFERENCES	103

TABLES

Table 1: General Characteristics of Induced Events	10
Table 2: DFN Size Distribution	29
Table 3: Summary of Fracture Intensity Properties	31
Table 4: Summary of DFN Properties for Stochastic Structure Generation	31
Table 5: Summary of Key Inputs for FracMan Hydraulic Fracture Simulations	57
Table 6: Input properties used for the FracMan model simulation of hydraulic diffusivity in a single fracture.	72
Table 7: Input properties for XSite™ models used to investigate fluid-injection-induced seismicity sensitivity to reservoir fracture intensity	75

FIGURES

Figure 1: KSMMA Region, Source British Columbia Energy Regulator	3
Figure 2: Plan view and sectional view of induced seismic events with size scaled by magnitude (max magnitude 2.2) and coloured by the wells they are associated with. All wells are within the Upper Montney with the Upper bench wells being E, G & I and the Lower Bench wells being D, F & H	4
Figure 3: Top; Orientation of Image Log Derived Breakout Orientation and Drilling Induced Fracture Orientations. Bottom; Summary of Stress and Pore Pressure Gradients	5
Figure 4: Top; Histograms of the radial distance induced events are from their active stage for OP1 (The solid red and dashed orange lines indicate the mean and median values, respectively). Bottom; Cumulative distribution of event radial distance	6
Figure 5: Plan View and Section View of Induced Seismic Events for OP3; Size Scaled by Magnitude (max magnitude M=3.1) and Coloured by the Wells they are Associated with. Section View Shows Major Stratigraphic Surfaces and the Lower Montney Wells.	7

Figure 6: Top; Histograms of the radial distance induced events are from their active stage for OP3. The solid red and dashed orange lines indicate the mean and median values, respectively..... 8

Figure 7: Treatment versus Magnitude Data for OP3 with Breakdown Pressure (Right) and Average Rate (Left), Lower Wells A2, A4, and A6 are Denoted by Heavier Lines. The upper two graphs represent Phase 1 and the lower two graphs represent Phase 2 stimulation phase..... 9

Figure 8: Summary of Stress and Pore Pressure Gradients for Operator 3. Note that the depths of stratigraphic surfaces within the Montney Formation (i.e., top Middle Montney and top Lower Montney) were estimated based on well tops from nearby drilling. 10

Figure 9: The induced seismicity causation pathway, after Rogers 2018. 11

Figure 10: Alternative triggering mechanisms for induced seismic events, a) poroelastic response, b) pressure diffusion through a ubiquitous joint fabric and c) pressure diffusion through a partially connected network of structures. 12

Figure 11: Distribution of induced seismic events coloured, showing estimated vertical location and spatial distribution across the pad. Events coloured and scaled by moment magnitude..... 13

Figure 12: (a) Unique connections between the centre point of interpreted seismic lineaments and the active stages that caused the events, each different colour represents one lineament. (b) Rose diagram of the connection paths showing distinct bimodal orientation trend..... 15

Figure 13: Orientation characteristics of interpreted induced seismic lineaments. Grid squares are 500 x 500 m. In addition, a rose diagram of induced lineaments from an adjacent pad is included, showing the same NE-SW Set 1, but also a conjugate NW-SE Set 2..... 16

Figure 14: Power law plot of the length of measured structures (red), compared against the simulated length of DFN structures (red). The Cartoon on the right shows how the seismic resolution is at about 100 m, with structures longer than that being imaged and those less than 100 m not imaged..... 17

Figure 15: Plan view (a) and oblique view (b) plan view and (c) oblique view along the wellbore. Set 1 (dark), set 2 (light), and the short hydraulic fracs at the well are displayed..... 18

Figure 16: Basic geomechanics scheme (a) for determining seismic potential of structures (b). NE-SW structures (1) have high shear stress, reactivate readily and create seismicity. NW-SE structures (2) have very low shear stress, high normal stress and result in no-low seismicity. NE-SW hydraulic fractures (3) are tensile opening mode fractures with low shear stress and low seismic potential..... 19

Figure 17: Workflow for simulating induced seismic events. Generate Set 1, Set 2 and hydraulic fracs (a). Identify all fractures that directly or indirectly connect back to the wells (b). Decimate NE-SW fractures into 100 m² elements representing potential induced events (c). Sample these points and stochastically assign event magnitudes to reflect the observed induced seismicity distribution (d). The distribution of synthetic induced events is compared against actual events in the inset window (d). 20

Figure 18: A) Relationship between simulated volumetric fracture intensity (P32) and length of simulated seismic lineaments, and B) Comparison between the distance between the wells and both actual and simulated induced events..... 21

Figure 19: Three equip-probable realisations of simulated induced seismic events compared against the observed events (top left)..... 21

Figure 20: Side View looking west of OP1 Wells; Upper and Lower Bench Array with Wells Completed in Upper Montney. Seismic Events (Points) are Sized by their Associated Magnitude..... 23

Figure 21: Workflow for Interpretation of Seismic Structures in Leapfrog from OP1 dataset. a) Dominant Trend Identified and Lineament Generated; b) Extents of Wireframe Extended to include all Associated Events; c) Wireframe and Stratigraphy Compared 24

Figure 22: Consideration of Segmentation. Early Simulations Show Highly Connected Network from North to South; Final Simulations Produced More Realistic Results in Connectivity Simulations..... 24

Figure 23: Major Known Stratigraphy Compared with the Extents of Interpreted Seismic Structures (Yellow Wireframes) from Induced Seismic Events 25

Figure 24: Interpreted Structures Activated by Different Wells 25

Figure 25: a) Array of Induced Seismic Events Coloured by Magnitude; b) Interpreted Seismic Structures; c) Interpreted Structures by Dominant Trend..... 26

Figure 26: Calculation of P21 areal intensity for the interpreted structures at major Montney surfaces..... 27

Figure 27: a) Power Law Size Distribution for OP1 in red (OP3 Displayed in blue for Comparison); b) Simulated Size Distribution range of Smaller Structures (Green) relative to the mapped structures (red)..... 29

Figure 28: Structure orientation (Strike) for each set. The local vector orientation is developed from the variation of structure orientations within each set (see bottom right image) and so better reflects the overall orientation pattern for a set than simply assigning a constant trend. 30

Figure 29: Example of Connectivity Analysis in FracMan on the G Well (OP1) Using Four Different Levels of Connection. Brown structures are deterministic and green are stochastic..... 32

Figure 30: Preliminary Connectivity Analysis OP1: a) Well D Connectivity with Low Fracture Intensity and Low Connection Level; b) Well E Connectivity with High Fracture Intensity and Low Connection Level..... 33

Figure 31: Example of Connectivity Analysis; D Well, Stages 1 to 5. Induced Events are Coloured by Magnitude. Connected Network is Split into Stochastic (light purple) and Interpreted (dark purple) Structures to Highlight their Relationship to the Seismic Events. 34

Figure 32: a) Toe of the I Well Not Stimulated to Mitigate Seismicity; b) Induced Seismicity Associated with F and G Well Injection; c) Induced Seismicity Associated with I Well Injection..... 35

Figure 33: I Well Connectivity Analysis, Results using Connection Level 5 and 7 Displayed. Events Sized and Coloured by Magnitude. 36

Figure 34: Calculation of the spatio-temporal distribution of fluid-injection induced seismicity events. a) Illustration of the active stage (red) and radial distance r (dashed line) to the biggest event from the injection source. Also shown is the previous stage and associated events (grey). b) Illustration of the temporal filtering of events, assigning them to the active stage (red) or previous stage (grey), where the solid and dashed horizontal lines show the fluid injection and shut-in intervals, respectively. c) Typical seismic event distribution pattern of a hydraulic fracturing stage in the Horn River, BC (modified after Hummel and Shapiro, 2013). 38

Figure 35: The difference between pressure perturbation front in a porous medium (left) and a vertical fault (right). For the same amount of injected fluid (ΔV) with the same rate (Q) over the same time (t), the pressure fronts distance from the injection point are shown by the two headed dashed arrows ($r_P \ll r_F$). k_F , S_F and k_P , S_P refer to permeability and storage coefficient of fault and porous media, respectively ($S_F \ll S_P$ and $k_F \gg k_P$). 39

Figure 36: a) Full view of the induced seismicity with the corresponding r - t plot for well A2 of OP3. b) Example of stage 12 of well A2 that does not follow classical parabolic signature in r - t space.

Events are colored by the time of occurrence (color bar). The size of each point scales to the seismic event magnitude as indicated in the legend..... 40

Figure 37: Plot of distribution of hydraulic diffusivity values coloured according to their corresponding seismic event magnitude ranges, for the first phase of OP3 data. The solid red and dashed orange vertical lines correspond to the mean (4.5 m²/s) and median (2.3 m²/s) values, respectively. The adjacent illustrations depict a potential explanation for the observed trends between low diffusivity values (left) and high diffusivity values (right). See text for explanation. For both illustrations, the grey solid line represents the susceptible/activated fault, the red segment of the fault shows the shear slip extent corresponding to a larger magnitude event ($M_w \geq 2$), the blue solid lines represent the fracture intensity transporting the fluid pressure, and the dashed blue line shows the hydraulic fracture intersecting the fracture network propagated from the active hydraulic stage (red box). Also shown is the Mohr-diagram of the reservoir in-situ stress state where the red dot represents the normal and shear stress acting on the fault relative to its shear strength (red line). Both scenarios depicted assume the same fault orientation and strength, injection volume, and radial distance from the injection source (i.e., $r_1 = r_2$). 41

Figure 38: The event distribution and hydraulic diffusivity values on the identified structures for the first phase of injection in the OP3 dataset. The red ellipse bounds hydraulic diffusivity values of 4.5 m²/s and greater, and the blue ellipse bounds diffusivity values lower than 4.5 m²/s (i.e., highly fractured). 42

Figure 39: Values of effective hydraulic permeability and aperture calculated for structures activated during the first phase of OP3 fluid injection. The box plots show the properties for each structure, and the overall distributions of the properties are shown to the right, where the solid red and dashed orange vertical lines illustrate the mean and median values, respectively. 44

Figure 40: Seismic Energy Efficiency Calculated for OP3 Well A2 with Full Hydraulic Stimulation. a) and c) Show the hydraulic seismic injection efficiency, I_{eff} , as function of lapsed time since the injection start. b) and d) illustrate the cumulative radiated seismic energy release relative to the input hydraulic energy into the reservoir; the dashed black line represents the case where all the injected hydraulic energy is transformed to radiated seismic energy. 45

Figure 41: Full view of the induced seismicity recorded for well F of OP1 with the corresponding r-t plot. Events are coloured by their time of occurrence and the size of each point shows the seismic event magnitude, as denoted in their respective legends. Note that the top left figure (“Top View”) displays Wells D to I from top to bottom, respectively. 46

Figure 42: a) Full induced seismicity event distribution for stage 1, well F, OP1, with its corresponding atypical seismic event distribution in r-t space. b) Seismic event distribution for stage 25 with its corresponding classical parabolic distribution in r-t space. Events are coloured by their time of occurrence and the size of each point shows the seismic event magnitude, as denoted in their respective legends. 47

Figure 43: The distribution of hydraulic diffusivity colored by their magnitude ranges for OP1. The solid red and dashed orange vertical lines illustrate the mean (1.14 m²/s) and median (0.7 m²/s) values, respectively. 48

Figure 44: Plot of the effective hydraulic permeability and aperture calculated for all structures activated during the fluid injection for OP1. The box plots show the properties for each structure, and the overall distributions of the properties are shown to the right, where the solid-red and dashed-orange vertical lines indicate the mean and median values, respectively. 49

Figure 45: Hydraulic diffusivity values calculated for each event superimposed on the identified activated structures for OP1. Wells D to I are from top to bottom, and the hydraulic stages are shown as grey cylinders. 49

Figure 46: Seismic energy efficiency calculated for OP1 over the full hydraulic stimulation. Shown is the hydraulic seismic injection efficiency, I_{eff} , as a function of lapsed time since the start of injection. 51

Figure 47: Seismic event distributions in r-t space for well F of OP1. Both parabolic and non parabolic signatures are shown by the blue and red boxes, respectively. The adjacent illustrations show the pressure perturbation front from the injection point. The red intensity represents the pressure distribution from highest (red) to lowest (white). For both reservoir geometries the injected volume is the same but the pressure front distance, r_2 , is larger for the case where fluid flow is confined to a single structure orientation as opposed to the case with high fracture intensity, where the intersecting structures distribute pressure more radially, with distance r_1 . Also shown are the Mohr-circle representations for both injection scenarios assuming the same fault orientation and shear strength (red line), where the blue arrow shows the increased pressure perturbation due to fluid injection. The profile of the aperture, a , due to injection into the fracture transmitting fluid pressure and volume is shown in purple. The aperture of the fracture highly intersected with other fractures, a_1 , and the aperture of the same fracture not intersecting other structures, a_2 , are relative (i.e., $a_2 > a_1$) but exaugerated for illustration purposes. 53

Figure 48: a) View of all induced seismicity data for well F of OP1 with the corresponding r-t plot. Events are coloured by the average injection pressure, and the size of each point shows the seismic event magnitude, as denoted in their respective legends. In the top view plot, the east and west of the reservoir is separated by a dashed grey line, which approximately separates areas where the injection pressures are larger than 60 MPa (East) and lower than 60 MPa (West). b) The same as plots as in a) except the events are coloured by the average injection rate (m^3/min). 55

Figure 49: Relationship between hydraulic diffusivity, the connectivity of the structures with each corresponding stage, seismic event magnitude and the average injection pressure for OP1. The grey line shows the inverse relationship between hydraulic diffusivity and the number of connected structures with the hydraulic fracture. 56

Figure 50: Plan and section view of OP1 grid with stress properties. 58

Figure 51: Scale of modelling grid and population of stress properties using the Eaton equation. 59

Figure 52: View of the upper and lower bank of wells within the Upper Montney, displayed against the SHmin property showing the variable stress in the Upper Montney. 59

Figure 53: Wellbore axial view of hydraulic fracture shape showing the long skinny fracs forming in the lower stiffness layer from the lower bench of wells and the more radial fracs forming from the upper bench stimulation into the higher stiffness layer. Coloured property shows static Young's Modulus. 60

Figure 54: Cross sectional view from the south, with events coloured by their triggering well and differentiated into upper and lower wells. Histogram of event frequency also differentiated into upper and lower wells. 61

Figure 55: View of the FracMan hydraulic simulation results. Upper view oblique view from the south and Lower view, plan view. The direction of SHmax is shown on the lower image, with the aligned fractures being the induced hydraulic fractures. The other fractures are inflated natural structures and are discussed below. 62

Figure 56: Basic geomechanics of injection (modified from Figure 16) to include inflated natural structures (No 4). 63

Figure 57: Plan view showing those natural structures that were inflated during stimulation (green) and the total population of interpreted structures (grey). The rose diagrams show the orientation trends for the top populations as indicated by the colour of the outline. Induced seismic events greater than $M=0$ is also shown. 64

Figure 58: Hydro-shearing results for each well. The dark green dots represent the observed induced seismic events for the specific well. The light grey structures represent the total set of interpreted structure. 66

Figure 59: Plan and section view of OP3 grid with stress properties & stratigraphy. The grid displays SHmin property. Top right shows views of the Lower Montney DFN model described more fully in Section 3.2.2. 67

Figure 60: Simulated seismicity associated with fault reactivation for 4 realisations of the OP1 developed DFN model. Actual events are coloured in red. The smaller more regular points represent the simulated events. 68

Figure 61: Comparison between left) open hole completions and right) limited entry completions. 70

Figure 62: Total connected seismic fault length for limited entry and 4 hydraulic frac length scenarios ($2 \times X_f$). 70

Figure 63: Comparison between left) open hole completions and right) limited entry completions. 71

Figure 64: FracMan well test modelling, studying the physical concept of hydraulic diffusivity values for injection along a single fracture. a) Model geometry and the location of the observation wells (blue) relative to the injection well (red). b) Pressure distribution along the fracture after two hours of injection simulation. c) Pressure profile during the injection time at each well. d) Plots of the hydraulic diffusivity as a function of pressure perturbation. 73

Figure 65: Representation of the fracture intensity connection with the active stage used to construct the XSite™ models. The blue box represents the high fracture intensity area of the reservoir, where the structures are well connected. The red box illustrates the low fracture intensity area of the reservoir, which incorporates only a few connected structures. 74

Figure 66: Impact of fracture intensity on XSite™ modelling of fluid-injection-induced seismicity. a) Pressure distribution after 1 hour of injection into the low fracture intensity model (LFIM), left, and high fracture intensity model (HFIM), right. b) Comparison of the bottom hole injection pressure and cumulative seismic moment release during fluid injection for both models. c) Seismic energy efficiency for both models during the full injection time record. 76

Figure 67: $r - t$ plot, hydraulic diffusivity and induced seismicity magnitude distributions for the LFIM (top row) and HFIM (bottom row) models. The solid red and dashed orange lines indicate the mean and median values, respectively. 77

Figure 68: a) Simulated injection rate inputs for the rapid and slow ramp-up models. b) Injection pressure and cumulative seismic moment release over the injection time. c) seismic energy efficiency for each model. 79

Figure 69: Aperture distribution after 15 minutes of fluid injection (top row) and pressure propagation at the end of injection simulation (bottom row), for the rapid (left column) and slow (right column) ramp-up scenarios. 79

Figure 70: From left to right: hydraulic diffusivity, hypocenter distance from injection source, event occurrence delay since the injection start, and seismic event magnitude distribution, for the rapid (top) and slow (bottom) ramp-up models. The solid red and dashed orange lines indicate the mean and median values, respectively. 80

Figure 71: a) Shows the injection scheme in all three simulation cases, note that the same amount of fluid was injected (300 m^3) and the injection time therefore is varying (the longest injection time is for the constant injection pressure). b) Illustrates the injection in the first 13 stages of OP3 well A2. Each stage duration is shown by the black horizontal segmented line, the color of the curve matches its corresponding axis. 80

Figure 72: a) Bottomhole pressure and cumulative seismic moment release during fluid injection for three cases: small versus large alternating injection rates versus constant injection rate. b) Seismic energy efficiency during the same simulated injections..... 81

Figure 73: a) Bottomhole pressure and cumulative seismic moment release during fluid injection for three cases: small versus large alternating injection rates versus constant injection rate. b) Seismic energy efficiency during the same simulated injections..... 82

Figure 74: XSite™ model for Stage 12 of OP3 well A2 used for calibration exercise. In this scenario, a hydraulic fracture (HF) is connected to natural fractures NF1 and NF2 in series. The dimension of the model is shown, and the top of the model is located at 1.4 km depth. 84

Figure 75: Comparison of the field-measured cumulative seismic moment release for stage 12 of OP3's well A2 and that achieved in the calibrated model. The red circles show the event magnitude, and the red solid arrows indicate the occurrence time for each event..... 84

Figure 76: a) Injection volume ramp-up rates implemented in models comparing a fast and slow injection ramp-up to that for the calibrated base case. b) Injection pressure and cumulative seismic moment release over the injection time. The dashed magenta-coloured ellipses on the cumulative moment release curves identify sudden moment seismic releases in the form of large slip events. c) seismic energy efficiency curves for each of the three models. Note that the base model refers to the calibrated model. 85

Figure 77: Plan view of the shear slip magnitudes (top row) and pore pressures (bottom row) on the fault after 25 minutes of fluid injection for the rapid (left column) and slow (right column) ramp-up volume rates relative to the calibrated base model (middle column). The location of the pressure perturbation front is shown by the red arrows. 86

Figure 78: Results for the rapid (top row), calibrated (middle row) and slow (bottom row) injection volume ramp-up rate models, showing from left to right, hydraulic diffusivity, hypocenter distance from injection source, event occurrence delay since the injection start, and seismic event magnitude distribution. The solid red and dashed orange lines indicate the mean and median values, respectively. 87

Figure 79: Bottom hole injection pressure and moment release for different injection pressure rates tested using the calibrated model. 88

Figure 80: Plan view of the shear slip magnitudes on the seismogenic structure after 45 minutes of fluid injection for the different injection pressure rates tested using the calibrated model. 89

Figure 81: Results for the rapid (top row), intermediate (middle row) and slow (bottom row) injection pressure ramp-up rates, showing from left to right, hydraulic diffusivity, hypocenter distance from injection source, event occurrence delay since the injection start, and seismic event magnitude distribution. The solid red and dashed orange lines indicate the mean and median values, respectively. 89

Figure 82: Schematic illustration of the pressurization rate and its effect on seismic energy response along a vertical fault. The graphs on the bottom show the injection ramp-up from initial pressure, P_{iny} , to the targeted injection pressure, P_{inj} , for rapid and slow pressurization rates..... 90

Figure 83: Sensitivity of hydraulic diffusivity in parameter space for the given fracture permeability and porosity of 10^4 mD and 10%, respectively. FR stands for "Friction Reducer" additive. Red circles compare the diffusivity values by fixing the compressibility of the system (5×10^{-8} Pa⁻¹; see black dashed line) and varying the viscosity. Green triangles show the diffusivity values for keeping the viscosity constant (20 cP; see solid black curve) and changing the compressibility. 91

Figure 84: Bottom hole injection pressure and moment release for the injection fluid viscosity sensitivity analysis using the XSite™ calibrated model. 92

Figure 85: Plan view of the shear slip magnitude (top row) and pressure (bottom row) on the fault after 25 minutes of fluid injection for scenarios based on the XSite™ calibrated model using different injection fluid viscosities. The red arrows show the pressure front location. 93

Figure 86: Plan view of the shear slip magnitude (top row) and pressure (bottom row) on the fault after 45 minutes of fluid injection for scenarios based on the XSite™ calibrated model using different injection fluid viscosities. The red arrows show the pressure front location. 94

Figure 87: Results testing different injection fluid viscosities using the calibrated base model, showing from left to right, hydraulic diffusivity, hypocenter distance from injection source, event occurrence delay since the injection start, and seismic event magnitude distribution. The solid red and dashed orange lines indicate the mean and median values, respectively..... 95

1.0 INTRODUCTION

Pressurized fluid, injected into deep reservoirs during hydraulic fracturing, changes the effective stresses on faults and other structures that may cause slip, releasing energy as seismic events. Our project has sought to consider this process by thinking about the components required to induce a seismic event: initial conditions at the well (susceptibility); the injection of high-pressure fluid; the pathway for fluid and pressure to migrate; the stresses and pore pressures in the surrounding regions; and the faults that may be reactivated.

The Kiskatinaw Seismic Monitoring and Mitigation Area (KSMMA) has been identified as an area prone to frequent induced seismic tremors. On 14 May 2018, the BC Oil and Gas Commission (BCOGC) issued a Special Project Order under Section 75 of the Oil and Gas Activities Act to address notification to stakeholders and to set up a process aimed at minimizing induced seismic events associated with operations in this area. Increased levels of industry well completion activity in induced seismicity (IS) prone areas has resulted in events continuing to occur, including a series of magnitude 4.5 and lower events on and around 29 November 2018 which were subsequently linked to hydraulic fracturing operations. In response, identification of key controls and influences on induced seismicity will improve the development and effectiveness of mitigation strategies that might be deployed to reduce the frequency of IS events.

To date, research efforts into Induced Seismicity have not fully considered the well completions and the connectivity of the well to the subsurface. Within the BC Montney, operators have been reluctant to release detailed subsurface data to researchers, limiting analyses to conceptual studies considering only regional constraints. Having gained access to three high-quality data sets from within KSMMA, an opportunity presented itself to examine the causes of IS from a more holistic perspective than has been possible before, where only events were available with only limited subsurface data. These data are confidential and referred to as Operator 1 (OP1), Operator 2 (OP2) and Operator 3 (OP3), with no location referenced. As the data is confidential, data sources, contractors etc. have not been referenced. Only OP1 and OP3 have been considered within this report. With access to these Montney IS data sets, specific research questions have been considered including:

- Do conventional geomechanical analyses explain the observed seismicity (e.g., critically stressed faults)?
- Is there a relationship between the observed seismicity, structural patterns, and completion type?
- Can the observed response of operational controls on stimulation be modelled to understand the physics of the fault reactivation process and the dynamics of fluid injection?
- Can advanced numerical models calibrated to field observations be used to inform quantitative rankings of IS mitigation strategies?
- Can these learnings be used to guide and inform the Province's regulatory environment?

Previous research and work on IS within the Montney can be divided up into several broad themes, namely:

- Data collection and compilation of stress data, geomechanics and basic analysis largely using public data, e.g., Enlighten 2019, 2021.
- Analysis of seismology data focusing on event magnitude distribution, moment tensors and stresses, e.g., Mahani et al. 2020.
- Modelling/simulation of conceptual induced events based on synthetic stratigraphy and plausible but unconstrained faults, e.g., Mehrabifard et al. 2021.

- Machine learning and statistical analysis of geological and operational controls on fluid injection and their likelihood to cause IS, e.g., Amini & Eberhardt 2018, 2021, Fox et al 2019.

A gap in all these analyses is the ability to take this integrated view of the subsurface involving geology, geophysics, geomechanics, engineering and hydraulics to try to establish key controls and influences on IS, such that mitigation can even be considered and effectively implemented.

For this project involving WSP and the University of British Columbia (UBC), the OP1 and OP3 datasets have been focussed on where induced seismic events were observed – one from the stimulation of the Lower Montney and one from Upper Montney stimulation. For these data sets, issues around how structures, interpreted from the induced events, connect back to active stages have been examined as have the hydraulic diffusivity properties of these connections. Additionally certain observations have been numerically simulated to attempt to back analyse critical properties of the pathways and faults and to explore potential mitigation options.

This report seeks to document these analyses and has been divided into the following sections:

- Section 2.0: An overview of the two datasets considered.
- Section 3.0: Mapping structural connectivity and the stochastic simulation of induced seismic events through Discrete Fracture Network (DFN) based analysis.
- Section 4.0: Characterisation of fracture pathways by hydraulic diffusivity.
- Section 5.0: Numerical simulation of hydraulic fracturing and induced events.
- Section 6.0: Analysis and numerical simulations to support efforts to migration the current level of induced seismicity.
- Section 7.0: Key learnings and recommendations for further work.

Our goal has been to attempt to better characterise the nature of the subsurface in terms of its structural fabric, to better understand the process of pressure communication such that practical engineering solutions can be developed to help achieve economic seismic mitigation (i.e., the minimum loss of resource value). Research into induced seismicity mitigation strategies, including informing these through comprehensive numerical modelling calibrated to field observations, was one of the clear recommendations of the Scientific Review of Hydraulic Fracturing in British Columbia (2019), this work aligns well with the provincial strategy.

2.0 SUBSURFACE DATA SETS

2.1 Introduction

Data was originally received from three operators (Operator 1, 2, and 3) from within the KSMMA boundary, shown in Figure 1. The KSMMA area represents a zone within northeastern British Columbia (BC), situated between Fort St. John in the northwest and Dawson Creek in the southeast.

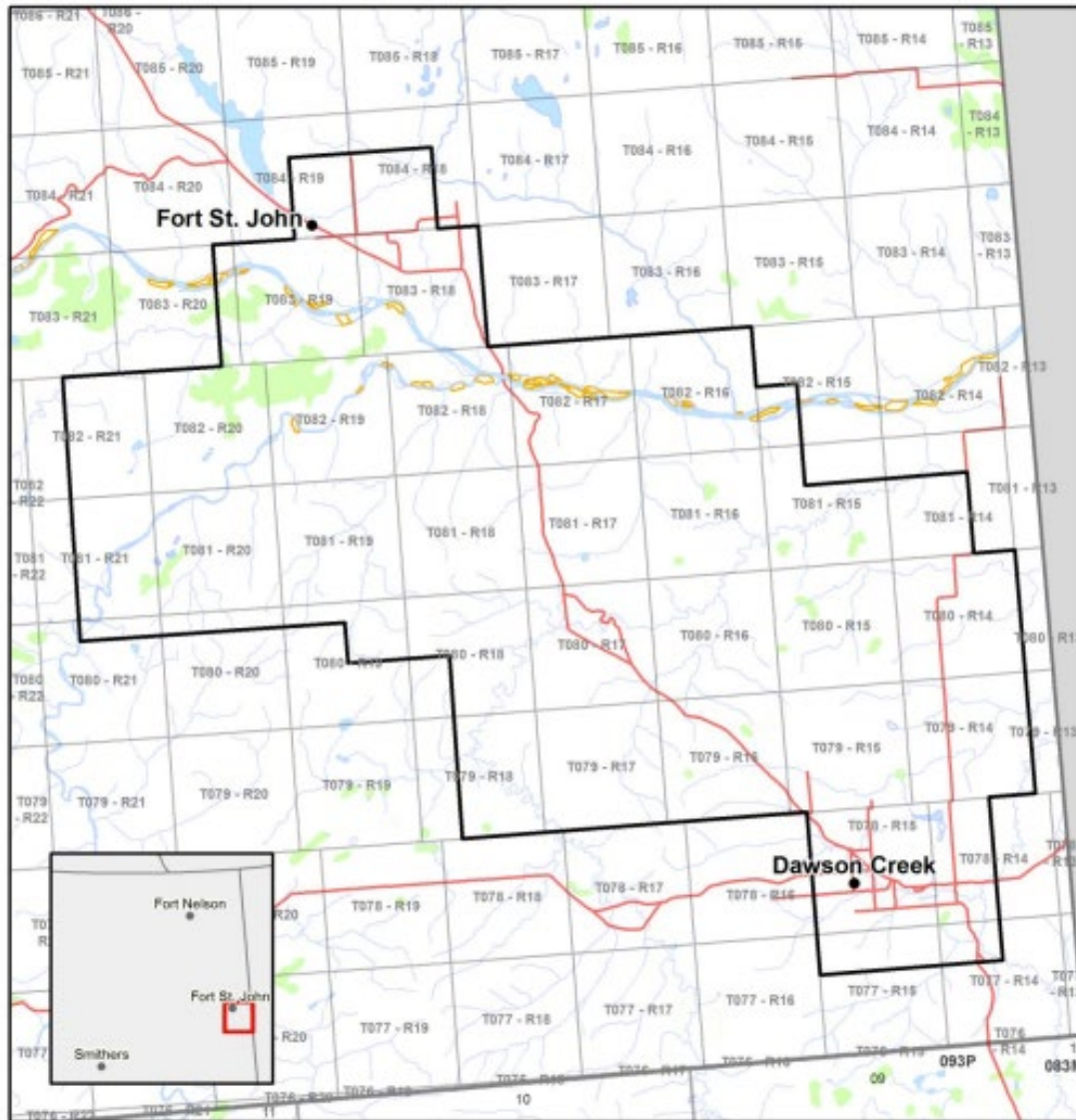


Figure 1: KSMMA Region, Source British Columbia Energy Regulator

These data were reviewed under a previous project supported by the British Columbia Energy Regulator (previously the British Columbia Oil & Gas Commission) and reported in Golder 2021. Based upon this review, data sets from Operator 1 and Operator 3 were selected for more detailed investigation. Operator 1 represented a six well pad, completed in two benches of the Upper Montney. Operator 3 represented a seven-well pad with four wells completed in the upper Montney and three in the Lower Montney. The following sections summarise the two data sets that have been investigated.

2.2 Operator 1 Data Set Summary

The data set for Operator 1 (OP1) is derived from the treatment of six east-west orientated wells, all completed in the Upper Montney using a plug and perf completion. A total of 4,434 of induced seismic events were recorded by an operator-owned shallow buried array, with moment magnitudes between -0.922 and 2.246 being observed. Induced events have been associated with the active stages from the wells using a simple temporal filter, Figure 2.

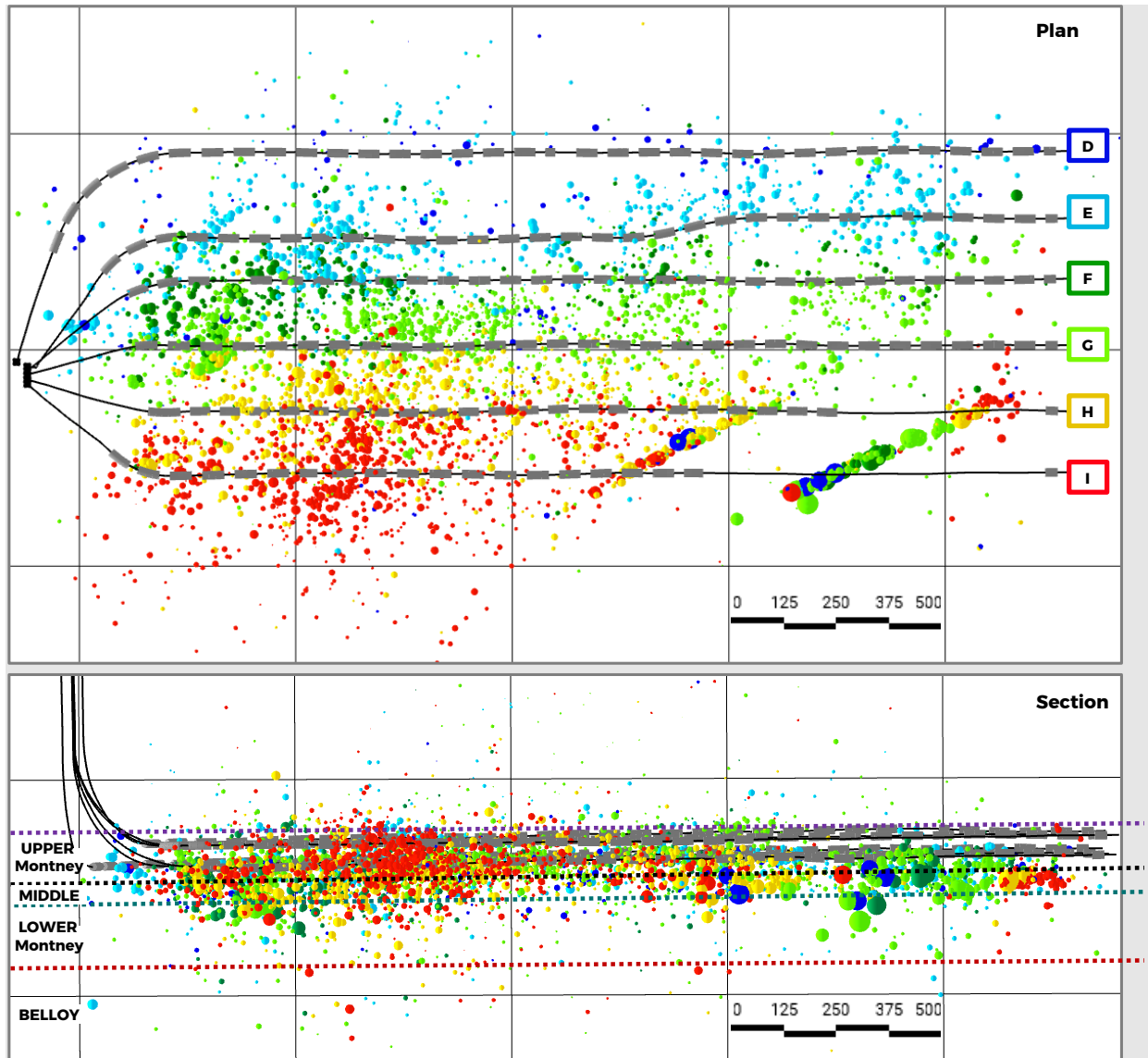


Figure 2: Plan view and sectional view of induced seismic events with size scaled by magnitude (max magnitude 2.2) and coloured by the wells they are associated with. All wells are within the Upper Montney with the Upper bench wells being E, G & I and the Lower Bench wells being D, F & H.

The spatial distribution of events reveals strongly aligned patterns of seismic lineaments with multiple trends being present, with the main trends being 055, 025, and 115 degrees. More details about the orientation patterns of interpreted seismic lineaments are found later in this report in Section 3.3.2.

Geomechanics data was available for this pad and stress and pore pressure gradients have been derived. An image log was available that provided the orientation of borehole breakouts and tensile drilling induced fractures, yielding an average direction of SHmax of 044 deg, Figure 3.

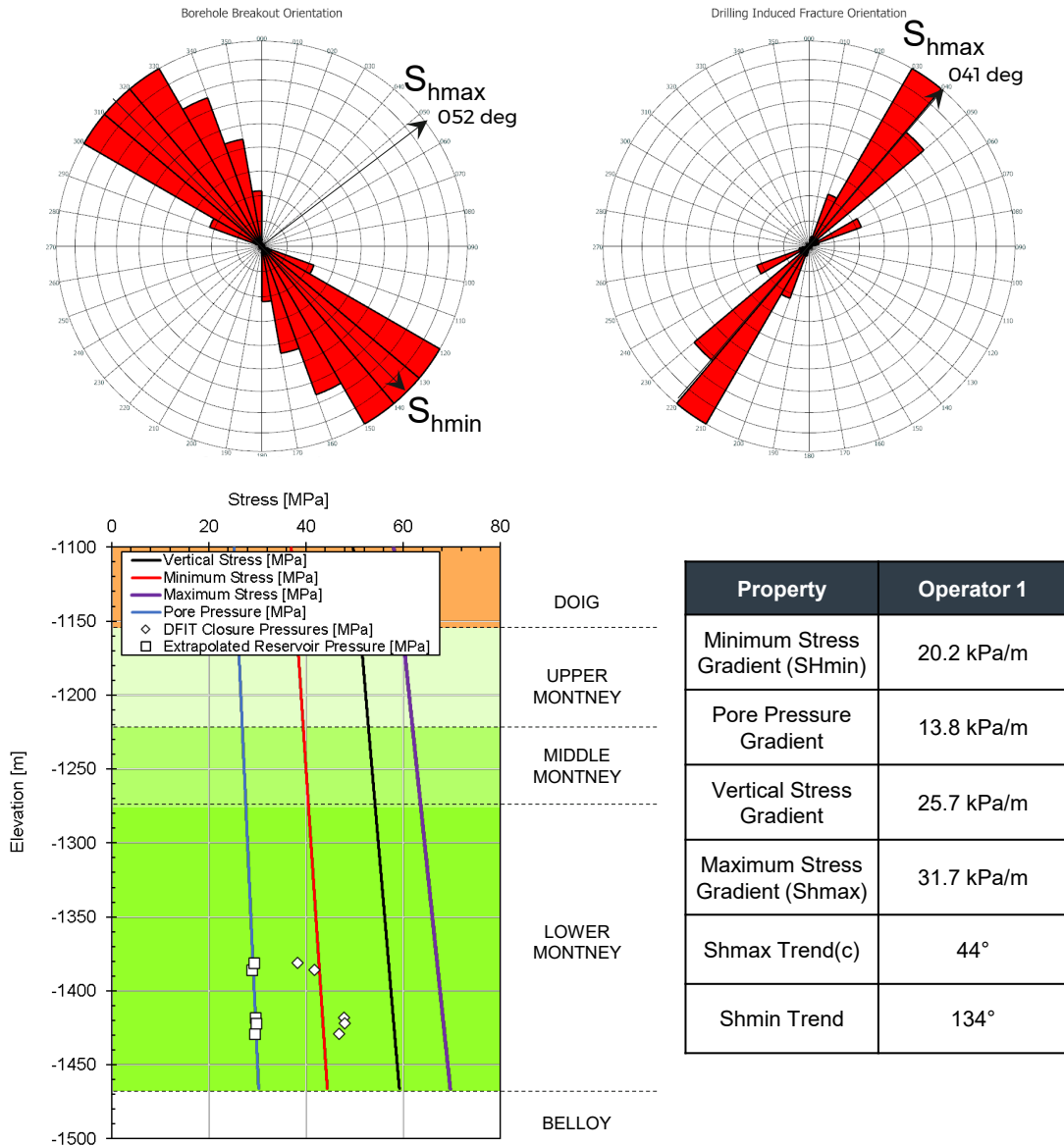


Figure 3: Top; Orientation of Image Log Derived Breakout Orientation and Drilling Induced Fracture Orientations. Bottom; Summary of Stress and Pore Pressure Gradients.

The distribution of the distance events occur from their triggering stage is found in Figure 4.

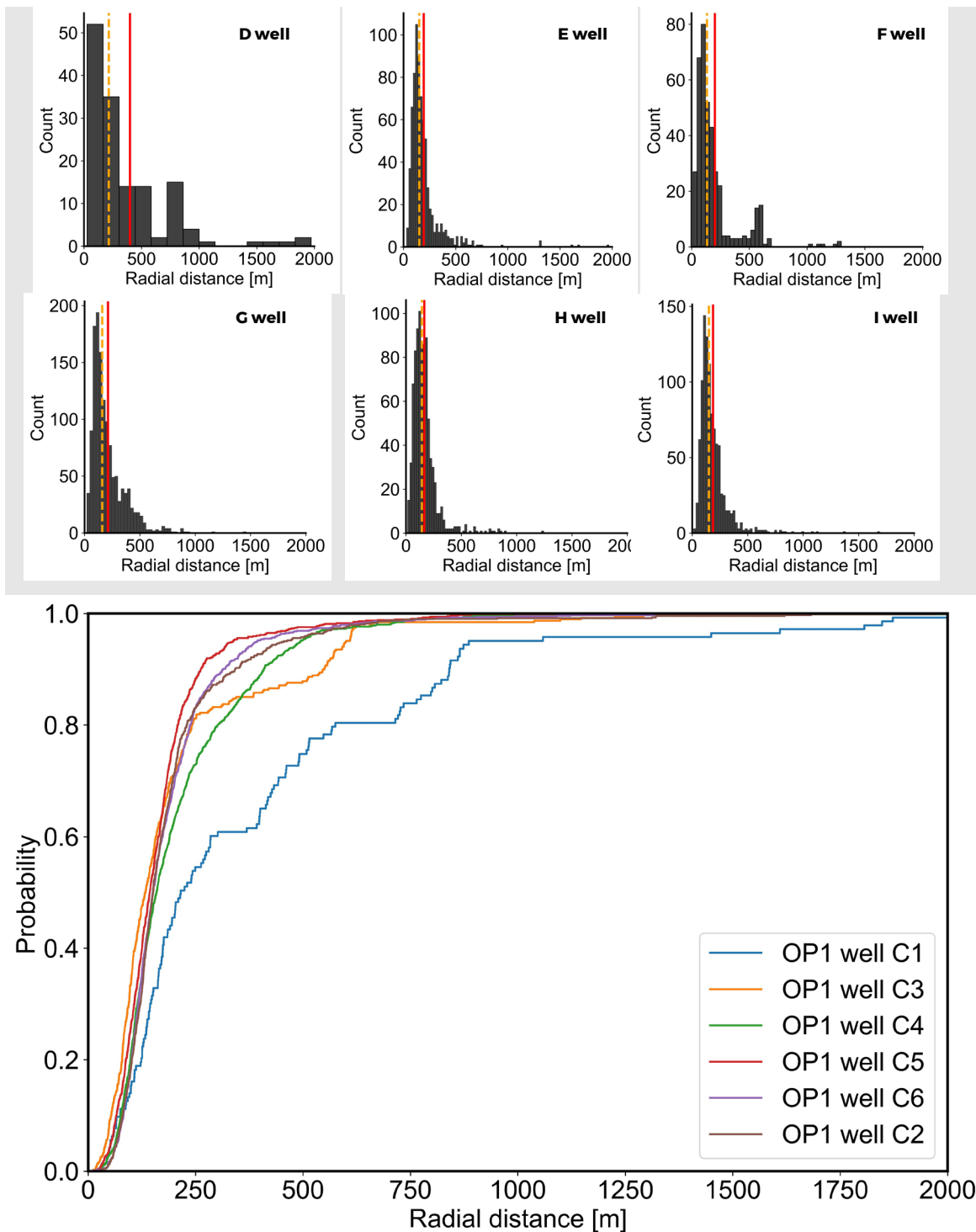


Figure 4: Top; Histograms of the radial distance induced events are from their active stage for OP1 (The solid red and dashed orange lines indicate the mean and median values, respectively). Bottom; Cumulative distribution of event radial distance.

Note how 90% of events for wells C2-6 occur within a distance of 350-500 m of their active stage. In contrast, 90% of events from C1 extend up to ~850 m away.

2.3 Operator 3 Data Set Summary

The data set for Operator 3 is derived from the treatment of seven wells, four completed in the Upper Montney and three in the Lower Montney (A2, A4, and A6). An open hole slickwater completion with ~50 m long stages were undertaken over two separate time periods (Phase 1 and Phase 2, separated by approximately 9 months). A total of 558 of induced seismic events were recorded by an operator-owned shallow buried array, with moment magnitudes between -0.64 and 3.1 observed. Induced events have been associated with the active stages from the wells using a simple temporal filter, Figure 5.

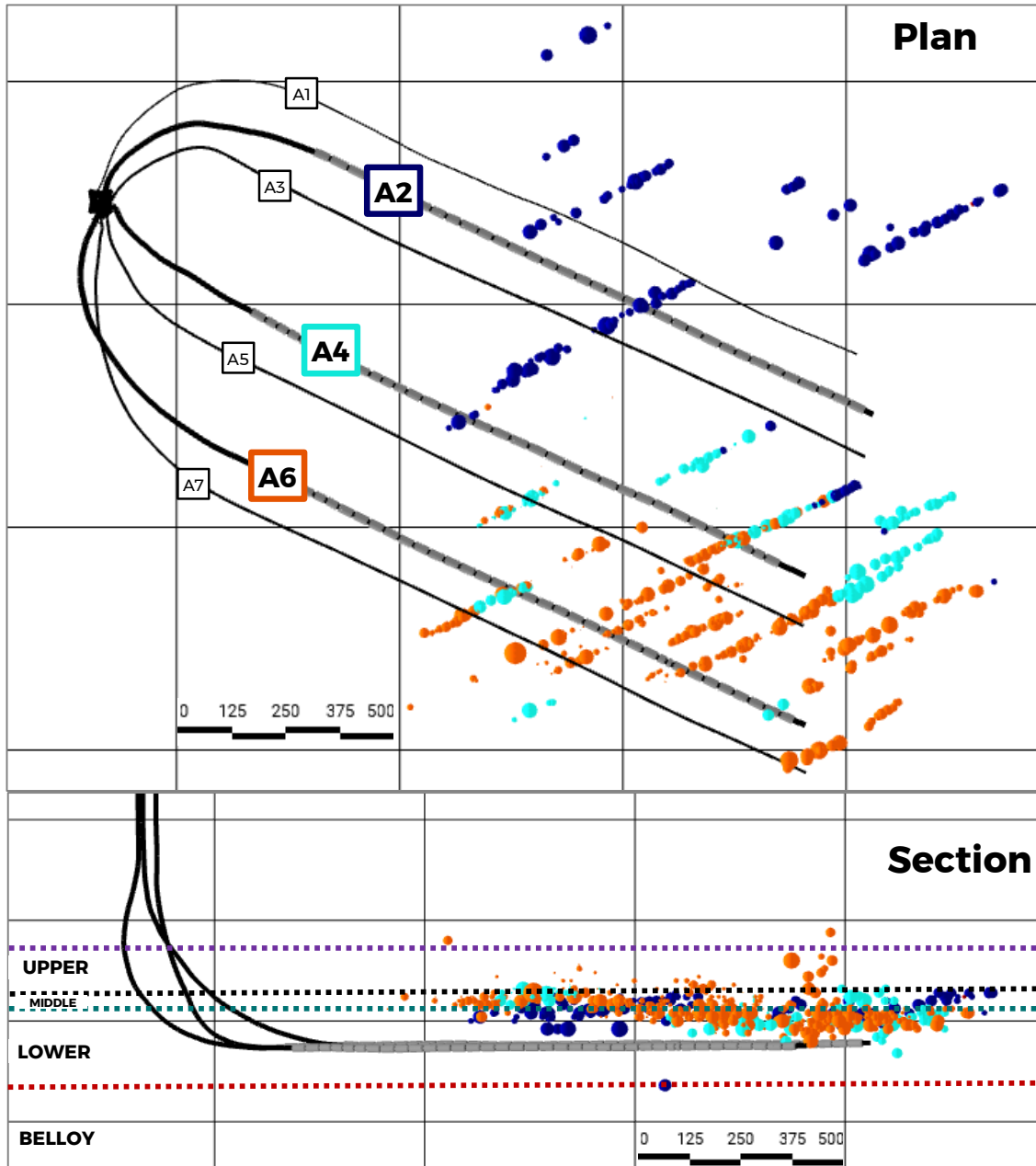


Figure 5: Plan View and Section View of Induced Seismic Events for OP3; Size Scaled by Magnitude (max magnitude M=3.1) and Coloured by the Wells they are Associated with. Section View Shows Major Stratigraphic Surfaces and the Lower Montney Wells.

The spatial distribution of events reveals a strongly aligned pattern of seismic lineaments with a broadly NE-SW (060 deg) trend. It is believed that the aligned structures are partly influenced by the seismic processing. The events are spread across the 3 lower wells and extend up to 500 m away (from the active wells, with most of the events being clustered in the toe half of the wells.

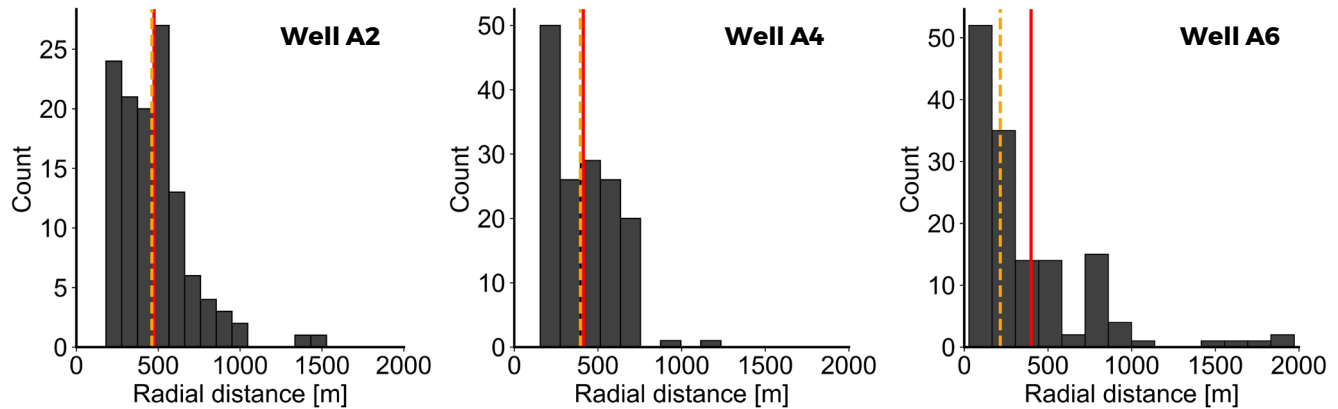


Figure 6: Top; Histograms of the radial distance induced events are from their active stage for OP3. The solid red and dashed orange lines indicate the mean and median values, respectively.

The shallow array geometry results in significantly more vertical uncertainty than horizontal. Figure 7 shows graphs of the surface breakdown pressure (left) and average pumping rate (right) plotted against the time. The graphs also show the seismic magnitude plotted on the right-hand y axis. The lower Montney wells (A2, A4 and A6) are plotted as solid lines coloured red, green and blue respectively and show a strong association with the seismic data plotted along side. Clearly some seismicity occurs outside of the active pumping windows but the strength of the association between Lower Montney stimulation and seismicity is compelling. We conclude that the induced seismicity is predominantly within the Lower Montney and Debolt Formation and for this reason, have focussed the study on the Lower Montney wells. However, we do acknowledge that there is some seismicity associated with Upper Montney stimulation. This may be leakage of pressure from Upper Montney wells down into the Lower Montney, a failure of the temporal filter to accurately associate stage activity with the correct events or other causes. However, we don't believe that the depth uncertainty changes our assessment and learnings.

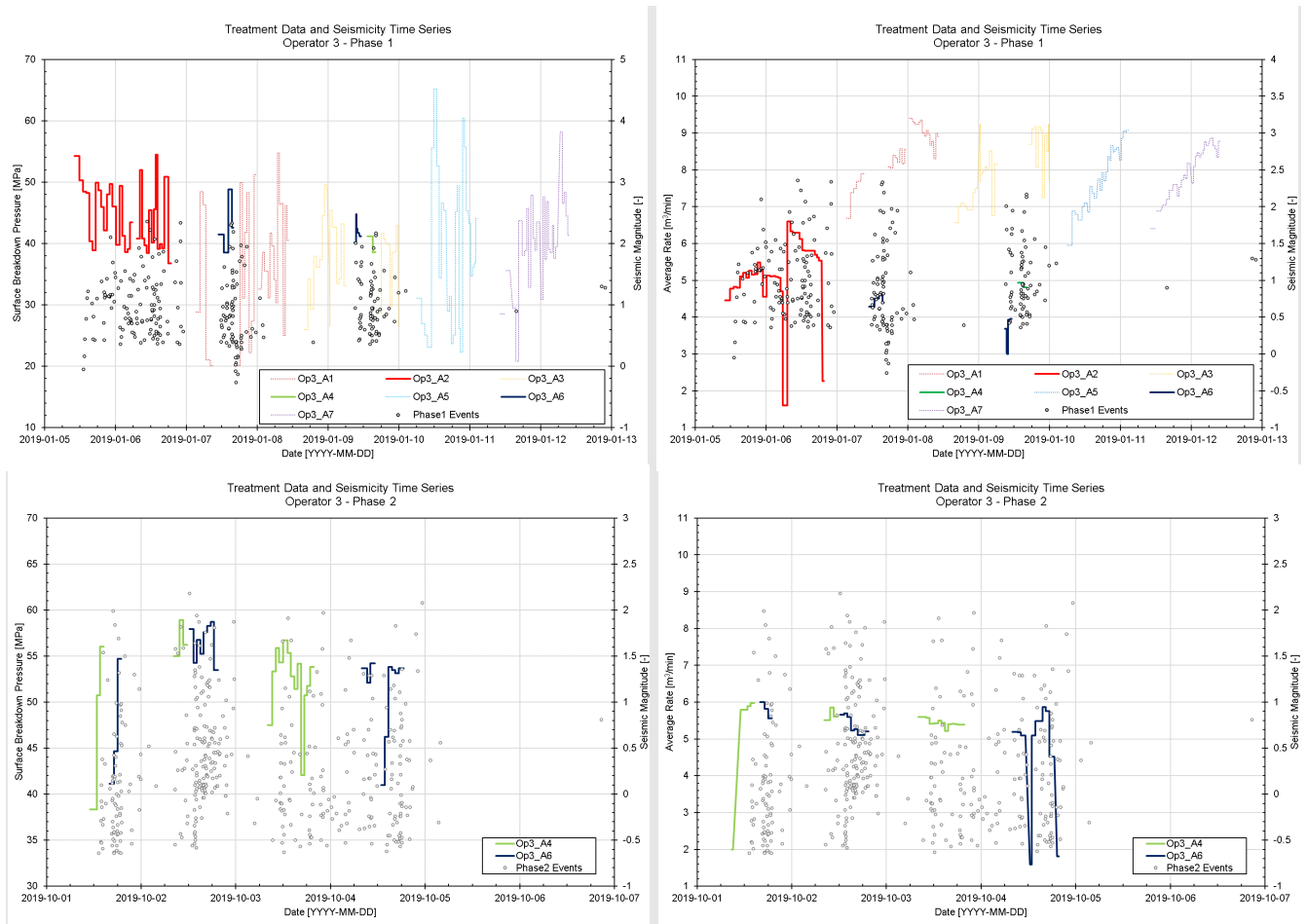


Figure 7: Treatment versus Magnitude Data for OP3 with Breakdown Pressure (Right) and Average Rate (Left), Lower Wells A2, A4, and A6 are Denoted by Heavier Lines. The upper two graphs represent Phase 1 and the lower two graphs represent Phase 2 stimulation phase.

No stress data were available for this pad and so properties have been inferred from the nearby OP1 pad, summarized in Figure 8. The direction of SHmax has been provided as 028 deg by the operator.

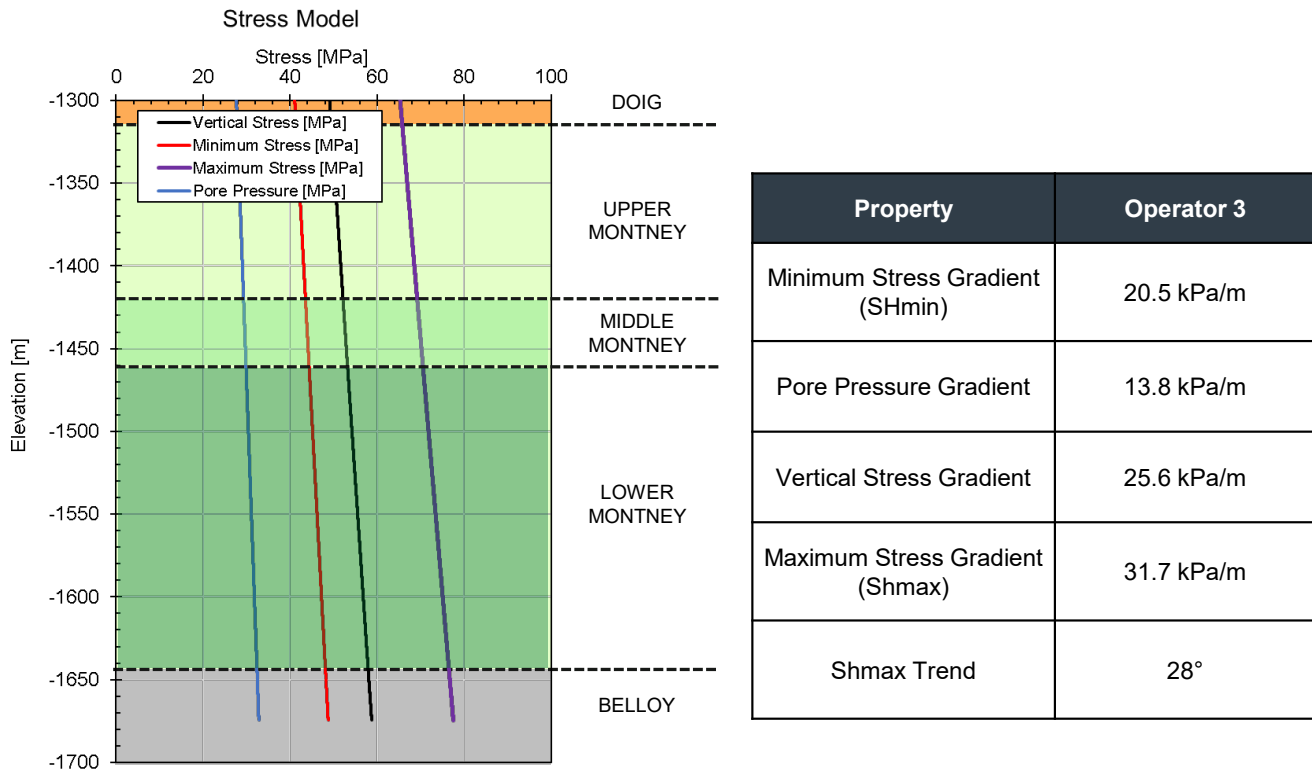


Figure 8: Summary of Stress and Pore Pressure Gradients for Operator 3. Note that the depths of stratigraphic surfaces within the Montney Formation (i.e., top Middle Montney and top Lower Montney) were estimated based on well tops from nearby drilling.

2.4 Summary of Induced Seismicity Data Sets

A broad comparison between the two data sets is presented in Table 1.

Table 1: General Characteristics of Induced Events

General Characteristic	OP1 (Plug and Perf)	OP3 (Open hole)
Maximum Magnitude	2.2	3.0
Minimum Magnitude	-0.922	-0.639
G-R b value	1.13	0.7
Depth Certainty	Reasonable	Poor
Stimulation Horizon	Upper Montney	Upper & Lower Montney
Primary Event Horizons	Upper & Lower Montney	Lower Montney & Debolt
Maximum Magnitude Lineament Trends	ENE-WNW	ENE-WNW
Lower Magnitude Lineament Trends	WNW-ESE NNE-SSW	Single major trend only
Structural Connectivity	Strong connectivity with multiple structural trends	Disconnected swarms with only a single structural trend imaged
SHmax trend	044 deg	028 deg

3.0 MAPPING STRUCTURAL CONNECTIVITY

3.1 Introduction

The geomechanics of pressurised water injection related seismicity are relatively well known with a straightforward causal pathway. Pore pressure and or stress changes result in induce stress changes on geological structures, resulting in the triggering of shear failure and the generation of a seismic event, Figure 9.

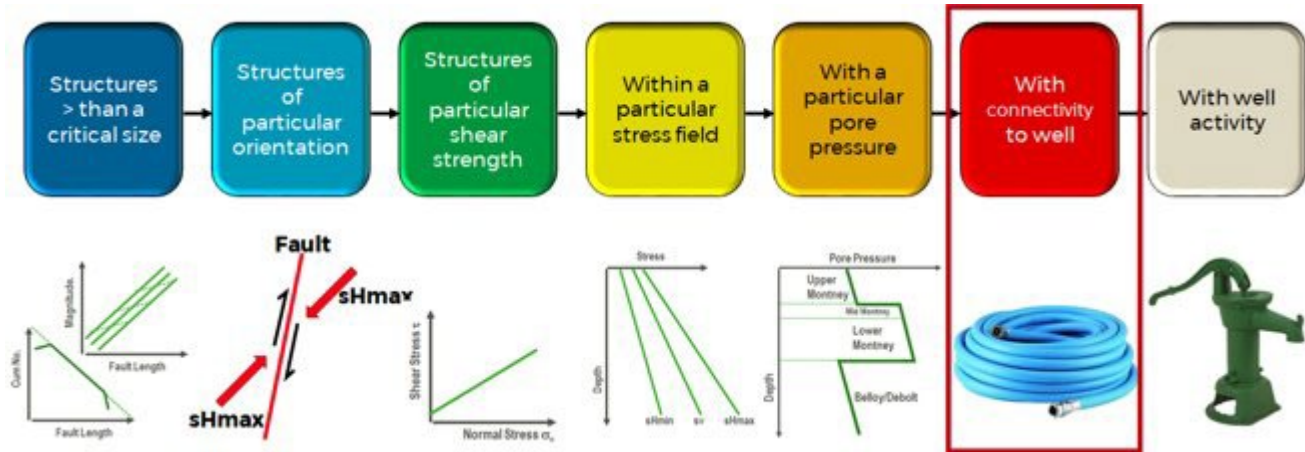


Figure 9: The induced seismicity causation pathway, after Rogers 2018.

The causation process comprises several component requirements: (1) A structure (e.g. a fault) of sufficient size (area) is required ($\sim 50\text{m}^2\text{-}1\text{km}^2$) in size; (2) That structure needs to be orientated appropriately to experience relatively high shear stresses; (3) The fault has to have a shear strength (ϕ) that could result in slippage, i.e., not a locked ancient fault; (4) The fault needs to be located within a certain stress field with an adequate pore pressure field; (5) The fault needs to be directly or indirectly connected to a well; and (6) the well has to be causing a pressure perturbation. With all this in place, the conditions for an induced shear event are met. This is in contrast to lower magnitude tensile events occurring during hydraulic fracturing.

Given that we can constrain or measure many of these features or properties, why is it that understanding the process remains so challenging? One key issue is how the stimulated well connects to the fault. The source of a pressure perturbation is obvious if the stand-off distance between a stimulation and known seismic fault is small. However, with increasing distances from the active well to activated fault, understanding the nature of the hydraulic pathway becomes a challenge.

In unconventional reservoir settings where matrix permeability is of the order of nanodarcies in magnitude and the majority of significant permeability is provided by a combination of natural and stimulated fractures, there are a number of potential triggering mechanisms to reactivate faults at some distance from the well:

- A poroelastic response where the presence of freely moving fluid transmits pressure away from the injection point;
- pressure diffusion through a ubiquitous joint, natural fracture or bedding fabric, or
- pressure diffusion through a partially connected (or variably permeable) network of structures.

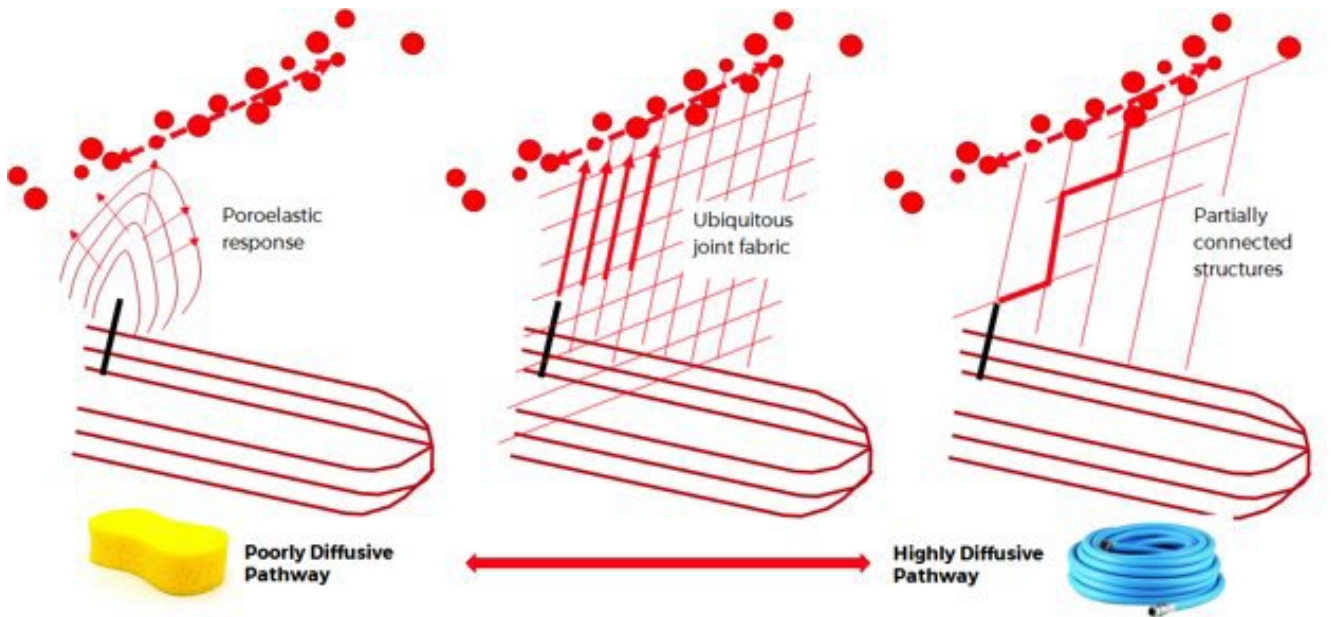


Figure 10: Alternative triggering mechanisms for induced seismic events, a) poroelastic response, b) pressure diffusion through a ubiquitous joint fabric and c) pressure diffusion through a partially connected network of structures.

If the triggering mechanism for fault reactivation is a poroelastic response from the active stage, then a far larger proportion of the stages would cause that same response and therefore a much wider spread and homogeneous response to stimulation. Similarly, if pressure diffusion through a well connected, effectively ubiquitous network of structures (sub-seismic faults and fractures) was the driving mechanism for large fault reactivation, the effect would be more widespread and pervasive. However, if pressure diffusion along a network of partially connected structures was the mechanism by which fault reactivation could be triggered, this would result in the spatially distributed and heterogenous response that is more typically seen.

This section of the report explores two cases where connectivity of structures can be used to help explain the distribution of induced seismic events. The first is a series of events associated with Lower Montney injection resulting a relatively simple pattern of seismic structures and the second is a complex pattern of events associated with hydraulic fracturing of the Upper Montney.

3.2 Stochastic Simulation of Induced Events

3.2.1 Introduction

For this study, we have taken the data set from Operator 3, a hydraulic fracturing treatment in the Montney within the KSMMA management area. The Montney Formation is a Triassic deposit consisting primarily of fine-grained sandstones, siltstones, and shales as well as some turbidite deposits. Two generations of vertical fractures have been identified in core (Gasparrini et al., 2021) and seismic (Vishkai and Gates, 2018), with fractures appearing to terminate in the Middle Montney. The Montney is underlain by the Debolt Formation, a massive carbonate unit known to host large induced seismic events (Riazi et al., 2020).

The treatment on this pad consists of an open hole slickwater completion with approximately 50 m long stages was undertaken over two separate time periods in four upper Montney wells and three lower Montney wells. This resulted in a total of 558 induced seismic events being recorded by an operator-owned shallow buried array, with moment magnitudes between -0.64 and 3.1 observed. The shallow array geometry results in significantly more vertical uncertainty than horizontal. However, there were virtually no events generated in the Upper Montney during the well stimulation (Figure 11.A), it was observed that the induced seismicity is predominantly within the Middle and Lower Montney formations. As such, the focus of this study is the Lower Montney wells.

The spatial (X-Y) distribution of seismic events shows a strongly aligned pattern of seismic lineaments (Figure 11.B), with a broadly NE-SW trend. The events are spread across the three lower wells and extend up to 500 m away from the active wells. The majority of the events are clustered in the toe half of the wells.

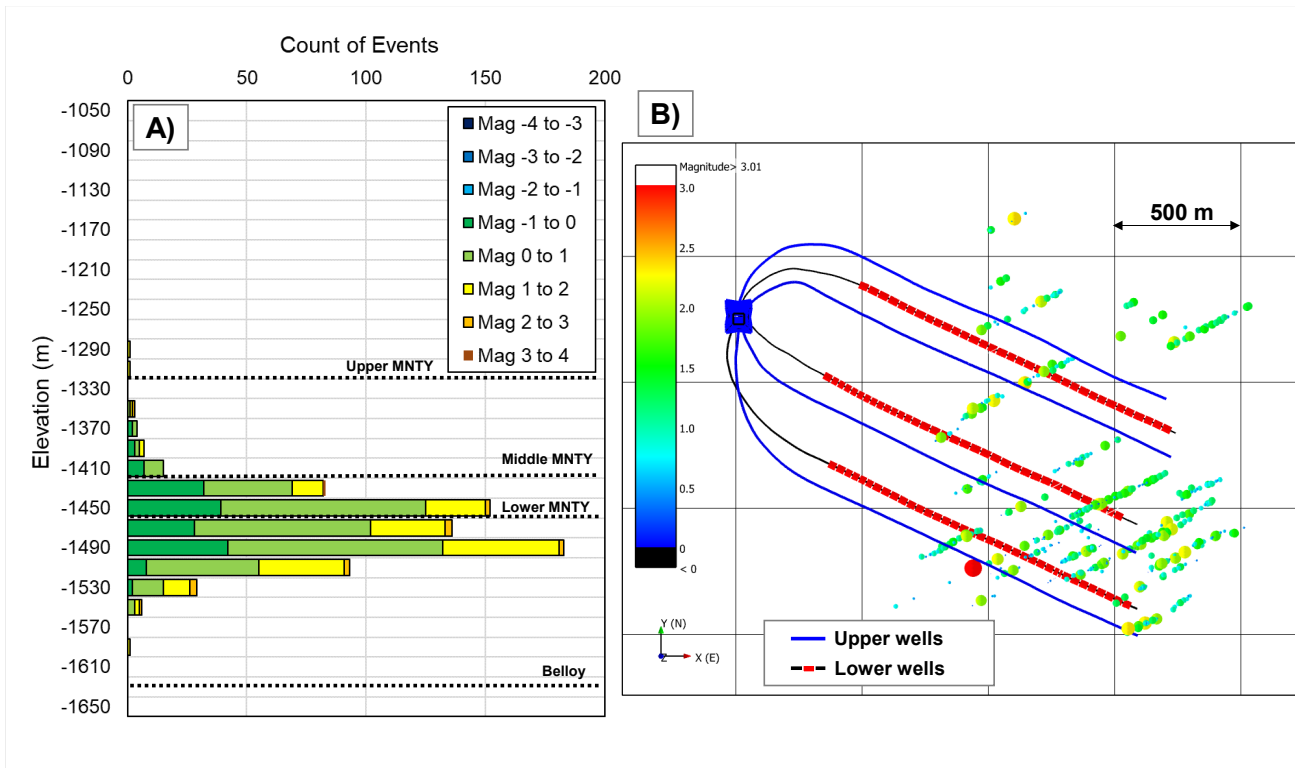


Figure 11: Distribution of induced seismic events coloured, showing estimated vertical location and spatial distribution across the pad. Events coloured and scaled by moment magnitude.

Based upon the distribution of events and the associated interpreted seismic lineaments, we can develop a simple conceptual interpretation that can be tested as follows:

- The distribution of seismic lineaments is believed to be associated with network of connected structures carrying pressure from the active well stages to critically stressed faults, present in the Lower Montney and below.
- The illuminated faults represent seismogenic faults (capable of generating seismicity) connected to active wells and that these faults are part of a larger network of structures.

- We can derive the geometric properties of the fault network (i.e., orientation, size and intensity) from the illuminated portion of these structures.
- Structures experiencing high shear stress exceeding local fault strengths will generate seismicity but other structures experiencing either tensile opening mode or higher normal stress will be aseismic and not be visible.
- To reproduce a synthetic seismic response, we need to identify those structures that are both connected to the well (either directly through the open hole completion or through hydraulic fractures) and seismically active.
- We have assumed that the natural structures have some conductivity, even if unpropped.

This conceptual model was tested through a stochastic structural modelling approach, described in the sections below.

3.2.2 Characterising the Geometry of Connected Montney Structures

3.2.2.1 Introduction

The key hypothesis of this work is that the geometry of sub-surface structures imaged by the induced events, represents a subset of a larger population of structures, many of which are not reactivated. To build models of these structures, we have used Discrete Fracture Network (DFN) analysis and modelling to represent the sub-surface structures stochastically, by defining distributions of structural orientation, size (radius) and intensity. This modelling is carried out in WSP-Golder' FracMan code, Golder 2022.

3.2.2.2 Orientation Definition

The orientation of structures can be determined in two different ways:

- Indirectly by looking at the association of events and the active stages at the time; and
- Directly by looking at patterns of induced seismic lineaments.

The pathways between active stages and events were first considered. Firstly, all seismic lineaments were numbered from 1-48. With the events already associated to a stage and using a simple temporal filter, each lineament is then associated with an active stage. This results in a one-to-many association between stages and lineaments, with each stage connecting to none, one or many lineaments. These connections between interpreted seismic lineaments and associated stages are illustrated as a spider plot which draws a line from stage to activated lineaments (Figure 12a) with the connections showing a bimodal distribution with a primary NE-SW trend and a secondary NW-SE trend, Figure 12b. The orientation of the pathway between the stages and seismic lineaments is then calculated. For simplicity, all pathways to a lineament have been located to the mid point of the structure (in 2D). The interpreted connections provide model evidence of a secondary, aseismic fracture set that needs to be considered to capture the actual structural connectivity.

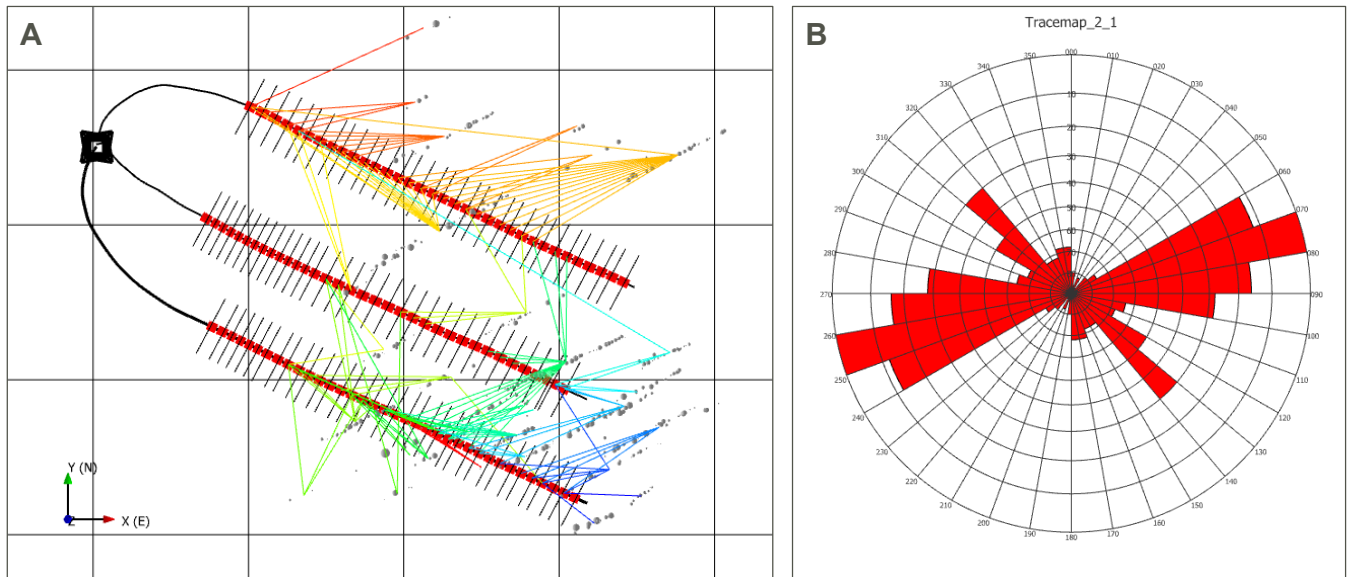


Figure 12: (a) Unique connections between the centre point of interpreted seismic lineaments and the active stages that caused the events, each different colour represents one lineament. (b) Rose diagram of the connection paths showing distinct bimodal orientation trend.

The resultant stage associated events do fail to show propagation paths in the maximum principal stress direction (~ 28 deg) with examples of direct stimulation from the hydraulic fracture to a well proximal event being very rare. Most of the events appear to be associated with a NE-SW fracture set, with connections observed between active stages and faults at considerable distance. Many of the induced events can only be explained by pressure migration through a second NW-SE fracture set.

Induced events are interpreted, and lineaments fitted to the data manually. The data show a strong highly aligned fault trend striking approximately 060° (Figure 13). Some of the lineaments represent high confidence interpretations, whilst others are less certain because of the spaced-out nature of the events. This conjecture is reinforced by induced seismic data from a nearby pad which also shows a bimodal distribution of two sets of lineaments at 060° and 110° (Figure 13).

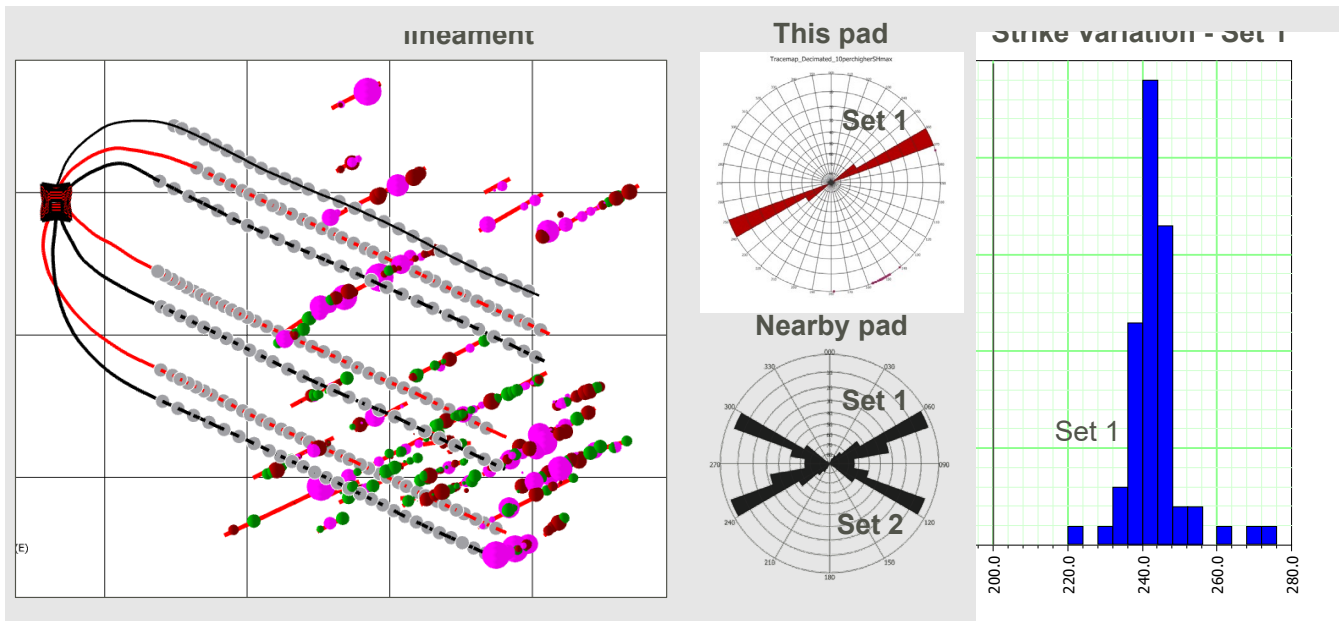


Figure 13: Orientation characteristics of interpreted induced seismic lineaments. Grid squares are 500 x 500 m. In addition, a rose diagram of induced lineaments from an adjacent pad is included, showing the same NE-SW Set 1, but also a conjugate NW-SE Set 2.

3.2.2.3 Structural Size Definition

The length of interpreted lineaments range between 100 m and 600 m and are usefully described by a power law distribution with a slope of -1 (Figure 14). A simulation of discrete structures using this power law description results in a high confidence match between observed and simulated lengths (Figure 14a). There is uncertainty in regard to the minimum observed lineament length. It could be 100 m; however, is more likely smaller as a result of event detection limits and a minimum area of fault patch required to generate an induced seismicity event (Eyre et al., 2019). If the minimum lineament size is lower than the system detection limit, the power law allows us to scale the intensity of structures as we reduce the minimum size. For example, reducing the minimum size from 100 m to 10 m results in an increase in structural intensity of 1000 times (Figure 14b).

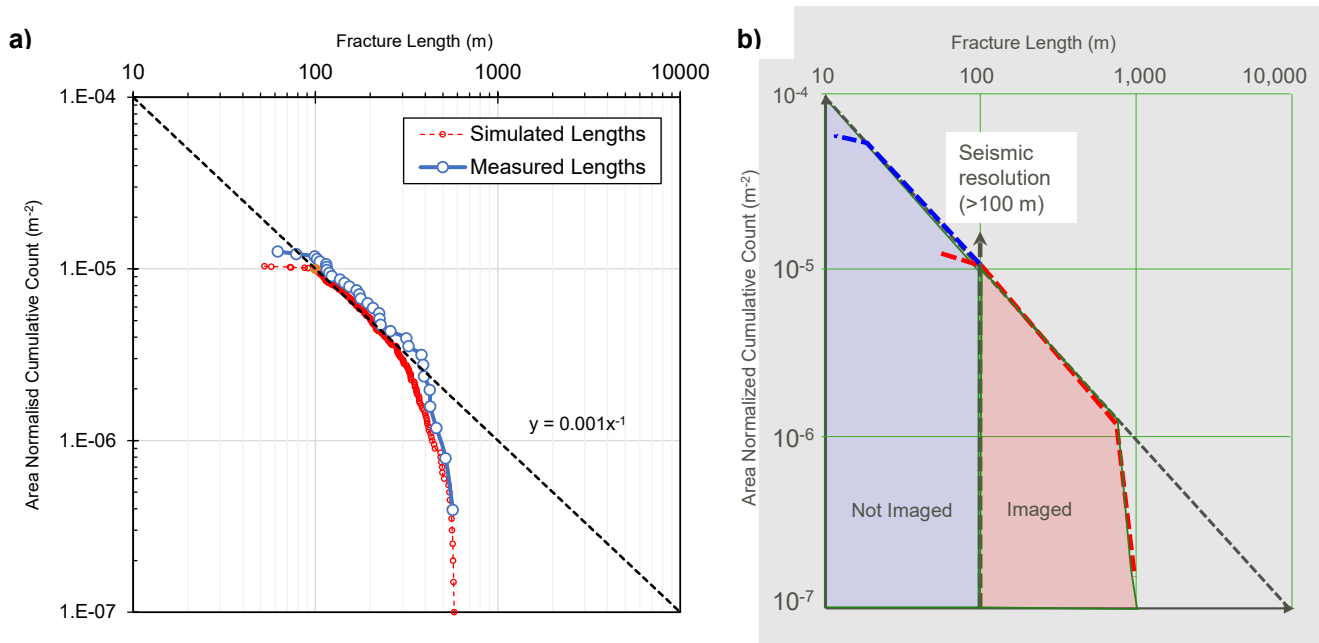


Figure 14: Power law plot of the length of measured structures (red), compared against the simulated length of DFN structures (red). The Cartoon on the right shows how the seismic resolution is at about 100 m, with structures longer than that being imaged and those less than 100 m not imaged.

3.2.2.4 Building a DFN Description of the Montney Structures

Generation of the DFN model (Figure 15) is carried out in FracMan® (WSP-Golder, 2022). Three sets of fractures are specified: A natural NE-SW seismogenic set, a NW-SE aseismic set, and a set of 200 m long by 30 m high hydraulic fractures originating from the center of each open hole stage. The hydraulic fracture length is provided by the operator and representative of an estimated propped fracture length. The unpropped length is estimated to be considerably longer and is considered as a sensitivity. The model is effectively 2.5-dimensional as vertical stress variations and stress barriers aren't fully considered outside of geological boundaries for fracture generation.

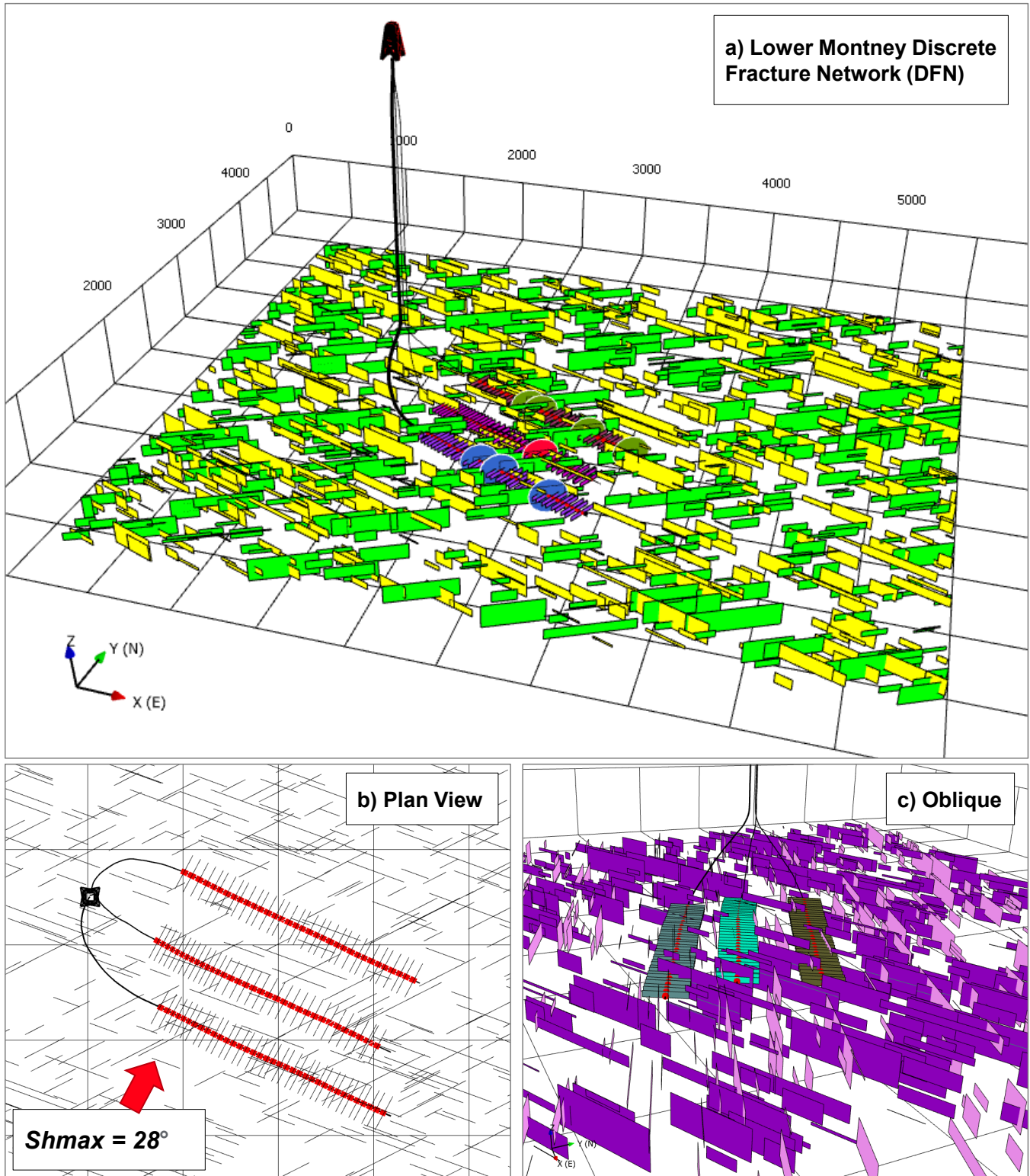


Figure 15: Plan view (a) and oblique view (b) plan view and (c) oblique view along the wellbore. Set 1 (dark), set 2 (light), and the short hydraulic fracs at the well are displayed.

3.2.2.5 Geomechanics Scheme

In order to identify which structures are seismogenic and which are aseismogenic, a heuristic geomechanics scheme has been applied. A Mohr's circle illustrates the geomechanical regime of the model, Figure 16a. The maximum principal stress direction ($S_{H_{max}}$) is estimated at 028° . This direction is oblique to the NE-SW set (striking 063°), making this set prone to high shear stresses and creating the induced seismicity zone in Figure 16. In contrast, the NW-SE set (striking 110°), is approximately normal to the maximum principal stress direction with high normal stresses, rendering this set unlikely to experience shear slippage and likely being aseismogenic. The NNE-SSW orientated hydraulic fractures, create opening mode fractures with little to no shear stress. They are therefore expected to propagate aseismically, at least below the magnitude detectable by the surface array.

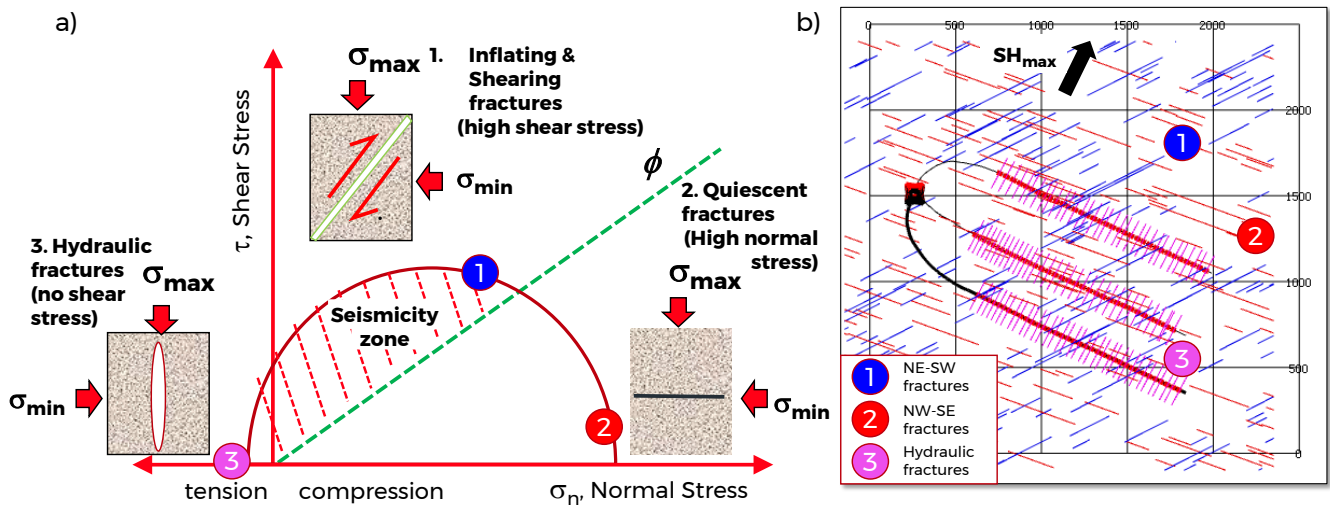


Figure 16: Basic geomechanics scheme (a) for determining seismic potential of structures (b). NE-SW structures (1) have high shear stress, reactivate readily and create seismicity. NW-SE structures (2) have very low shear stress, high normal stress and result in no-low seismicity. NE-SW hydraulic fractures (3) are tensile opening mode fractures with low shear stress and low seismic potential.

3.2.2.6 Identifying Connected Seismically Active Structures

Each stochastic realization of the DFN model populates fractures from the two natural sets based on the volumetric fracture intensity (P32), or fracture volume per unit area, as well as the minimum and maximum length limits for the fractures. The same hydraulic fractures are used each time. The DFN model is then used to interrogate induced seismicity by generating a synthetic set of induced events.

An initial arbitrary intensity of the natural fracture sets (i.e., P32) is specified, and a realization created (Figure 17a). Fractures that directly (pass through an open hole stage or connect to a hydraulic fracture) or indirectly (connect via a network of natural fractures) back to a well stage are identified (Figure 17b). Seismogenic NE-SW fractures are decimated into 100 m^2 elements, which are then converted to points representing potential induced events (Figure 17c). Finally, a consistent sub-sample of potential induced events is taken to mimic a more realistic catalog of synthetic induced events, with event magnitudes stochastically assigned to match the observed induced seismicity distribution (Figure 17d).

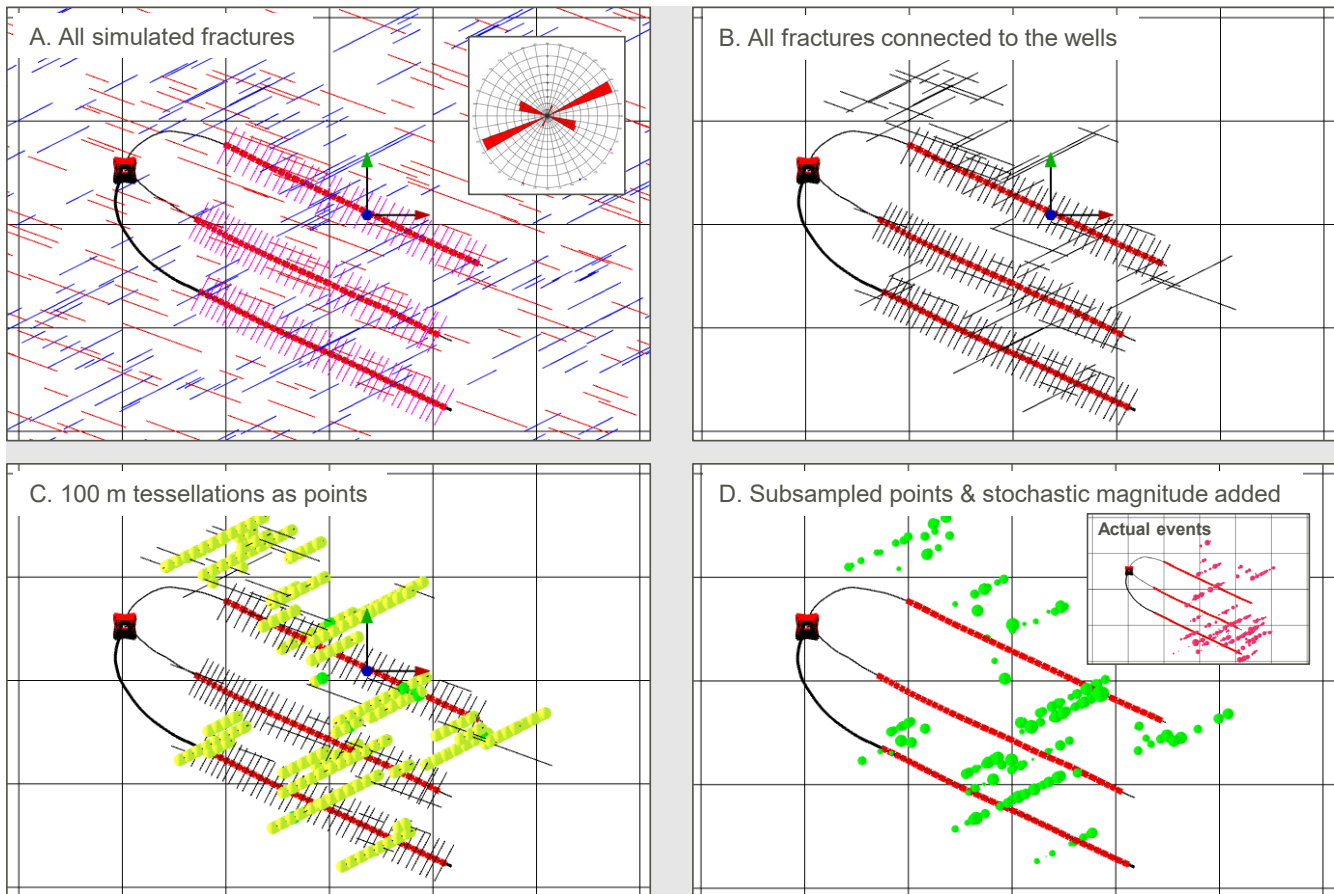


Figure 17: Workflow for simulating induced seismic events. Generate Set 1, Set 2 and hydraulic fracs (a). Identify all fractures that directly or indirectly connect back to the wells (b). Decimate NE-SW fractures into 100 m² elements representing potential induced events (c). Sample these points and stochastically assign event magnitudes to reflect the observed induced seismicity distribution (d). The distribution of synthetic induced events is compared against actual events in the inset window (d).

3.2.2.7 Calibration/Validation of the DFN Model

Each DFN realization is compared against observed induced seismicity using the total seismic lineament length and distribution of distances from stage to seismic event. The simulated seismic lineament length is calculated by summing all seismogenic NE-SW fractures that are connected to treatment stages. The Euclidean distance from stage center to the sampled simulated events is used to evaluate the distance distribution. The volumetric fracture intensity is varied between 2E-3 and 4E-3 (Figure 18a). An inferred P32 of 2.3E-3 m³/m² reproduces both the total simulated seismic lineament length (Figure 18a) and the stage to event distance distribution (Figure 18b).

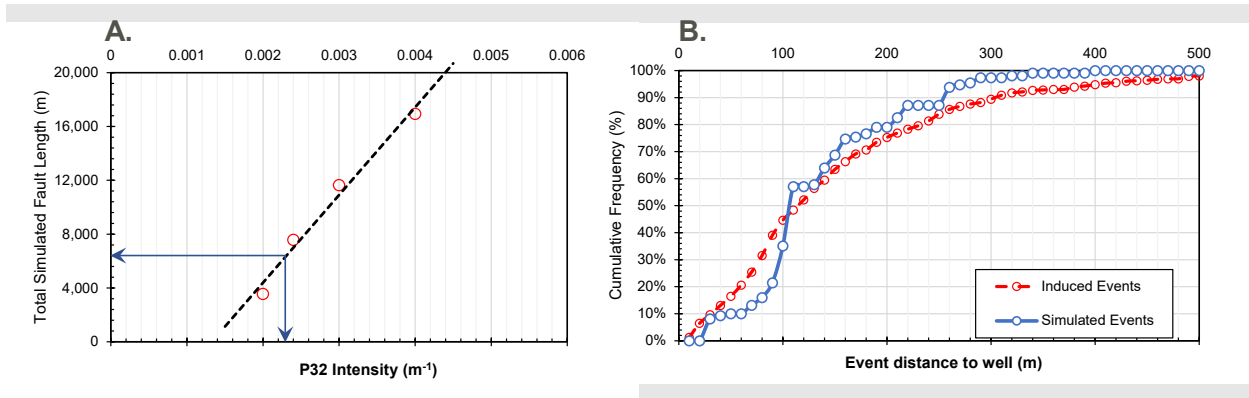


Figure 18: A) Relationship between simulated volumetric fracture intensity (P32) and length of simulated seismic lineaments, and B) Comparison between the distance between the wells and both actual and simulated induced events

The parameterized model is able to reproduce the nature of the induced seismicity well across numerous equiprobable realizations (Figure 19). Each stochastic realization shows one possible outcome of a subsurface fracture network. These realizations can provide hazard indicators such as the probability that a specific number of stages interact with fractures or the expected distribution of induced seismicity around the pad.

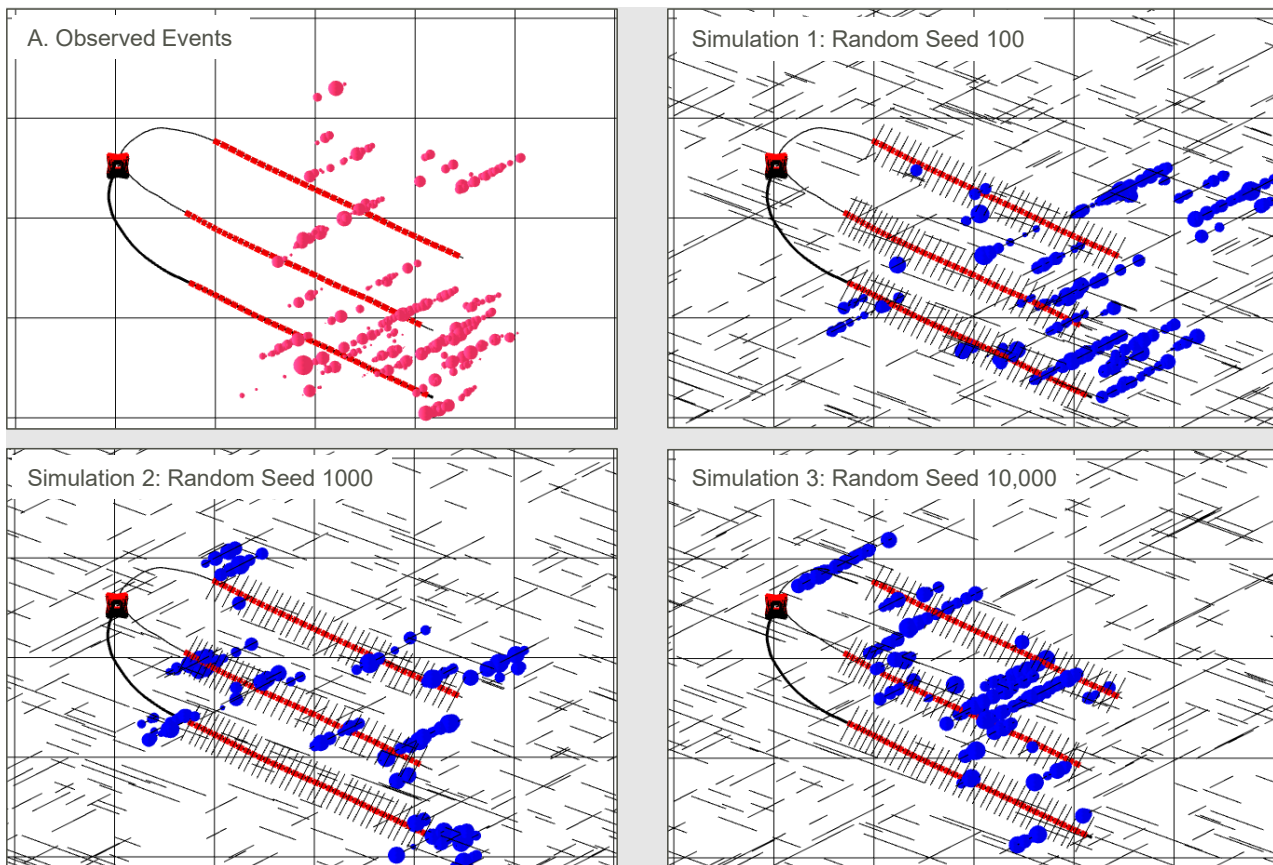


Figure 19: Three equip-probable realisations of simulated induced seismic events compared against the observed events (top left).

3.2.3 Discussion

Hydraulic fracturing induced seismicity requires some form of connection between an active treatment stage and a critically stressed fault with the potential for reactivation and seismic energy release. A fracture network of structures in the 10-100s m length represents a plausible way of characterizing plausible way of characterizing and modelling this connection. The results from this study utilized two fault sets, in fracture pathways extending up to 500 m away from the treatment wells, providing clear evidence for the potential of a meso-scale fracture network. DFN modelling has been used to infer the fracture geometric population parameters of both sets, balancing minimum fracture length with fracture intensity. The resultant DFN model realizations reproduce the nature of the induced seismicity well (seismic fault length, distance from well) across equiprobable realizations, with DFN connectivity being an apparent significant control on induced seismicity.

3.3 Characterisation of Montney Structures through Interpretation of Induced Seismic Lineaments

3.3.1 Introduction

The observed induced seismic events from Operator 1 provide evidence of a network of structures within the Montney Formation, Figure 2. The event catalogue has been interpreted in an attempt to characterise the geometry of these natural Montney structures and to further understand their role in pressure communication between the active stages and larger seismogenic faults.

Induced seismic events with their associated location, injection stage, and magnitude were provided. Seismicity on this pad is associated with Upper Montney stimulation, with six wells arranged in an upper and lower bench of the Upper Montney, Figure 20. Although the majority of the seismicity is recorded through the Montney sequence primarily below the wells, the biggest events occur in the Middle and Lower Montney. Some events are also seen above and below the Montney.

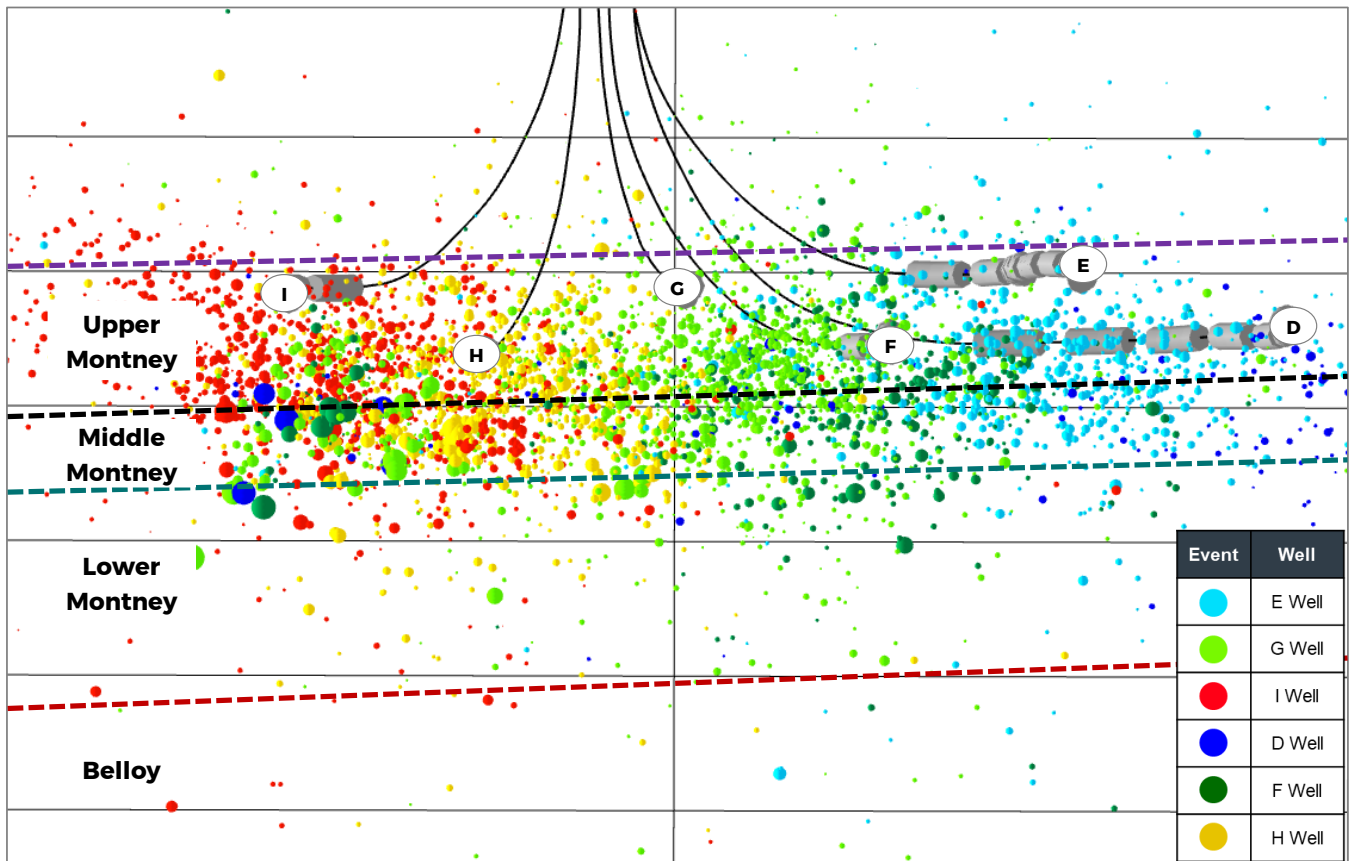


Figure 20: Side View looking west of OP1 Wells; Upper and Lower Bench Array with Wells Completed in Upper Montney. Seismic Events (Points) are Sized by their Associated Magnitude.

Using observations in both temporal and spatial trends in the occurrence of induced seismic events, WSP has interpreted the seismic structures.

3.3.2 Mapping of Deterministic Structures

Interpretation of seismic structures has been carried out in Leapfrog software (Sequent 2023) with the workflow for their interpretation being outlined in Figure 21 and described below:

- The interpretation started with the larger magnitude events which show less ambiguity in their interpretation.
- Polyline were drawn that constrained dominant trends in the array of data (Figure 21a). The identification of 2D lineaments was a preliminary step in order to gain a broad understanding of the trends that were associated with the event catalogue on the pad.
- Once a structure was generated (Figure 21b), the wireframe limits were extended to capture all events associated with the observed trend. Significant breaks between events were considered critically. If the disconnection was pronounced, the interpretation could be considered as a separate structure.
- The final step in the workflow (Figure 21c) was to check the wireframe against known stratigraphy surfaces and confirm that the interpreted extents were realistic. Structures generally terminate upwards against the top of the Upper Montney (MA5).

Data was considered from multiple views as well as by elevation, by magnitude, by well, and by stage. This was to ensure that the interpretation was not biased by perspective. Structure interpretations were updated and revised with each consideration.

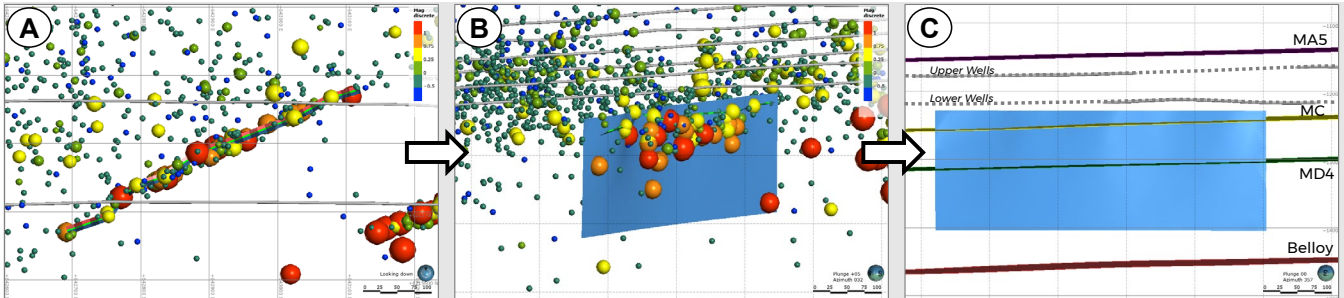


Figure 21: Workflow for Interpretation of Seismic Structures in Leapfrog from OP1 dataset. a) Dominant Trend Identified and Lineament Generated; b) Extents of Wireframe Extended to include all Associated Events; c) Wireframe and Stratigraphy Compared

With diminishing magnitude, there is increasing uncertainty and ambiguity with the interpretation. To account for this, the smaller structures associated with the lower magnitude events have been generated stochastically. See Section 3.3.3.

Preliminary connectivity analysis (discussed further in Section 3.4.2) indicated that revision of some of the longer mapped structures could improve the accuracy of the interpretation. Consideration of fault segmentation could create a more realistic representation of seismic structures. The example in Figure 22 shows both the original and revised interpretation during analysis. Although both interpretations represent the data set, the preliminary analysis indicates that the southern area of the pad is not stimulated by the later stages of injection. The inclusion of a persistent structure from north to south immediately results in a high level of connectivity. A segmented fault, with possible relay connections, is much more probable and provided more realistic results during subsequent simulations.

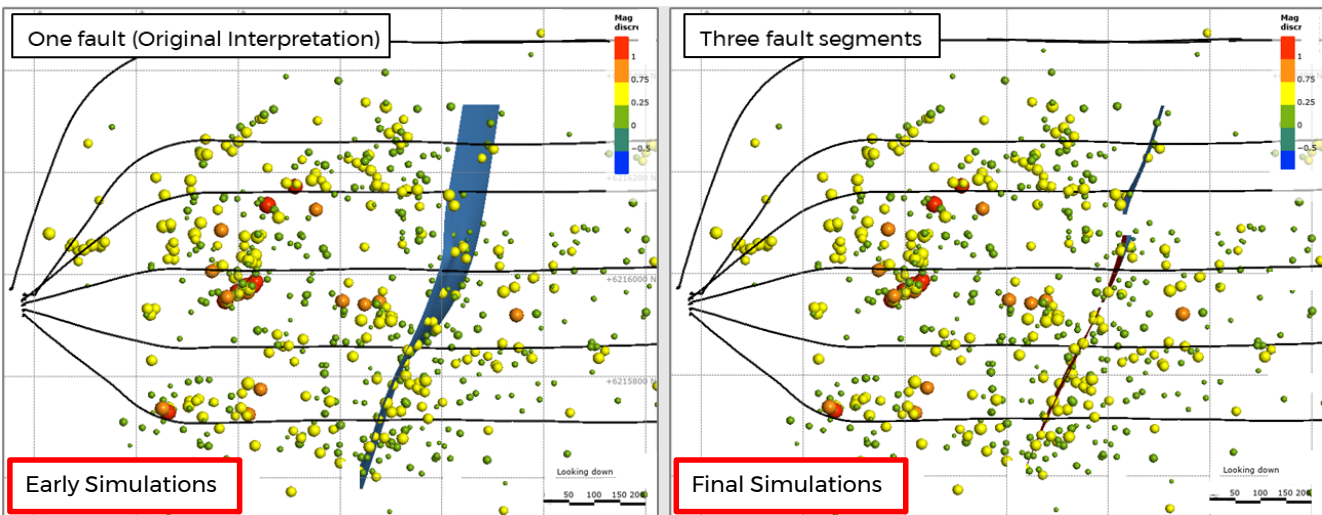


Figure 22: Consideration of Segmentation. Early Simulations Show Highly Connected Network from North to South; Final Simulations Produced More Realistic Results in Connectivity Simulations.

When the interpretation was complete, it was observed that only a handful of structures persisted into the Lower Montney (Figure 23). The majority of structures terminate right before or right after the Lower Montney surface (MD4). Geomechanics will be discussed further in Section 5.2.

Several of the persistent interpreted structures are noted to be activated by multiple wells (Figure 24). An investigation into the relationship between the well array (i.e., upper and lower bench) and the event occurrence is discussed during hydraulic fracture simulation, in Section 5.2.

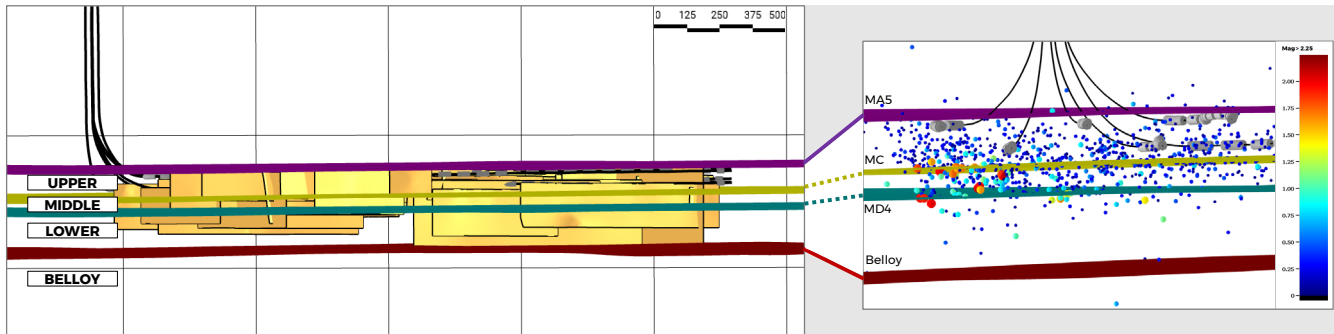


Figure 23: Major Known Stratigraphy Compared with the Extents of Interpreted Seismic Structures (Yellow Wireframes) from Induced Seismic Events

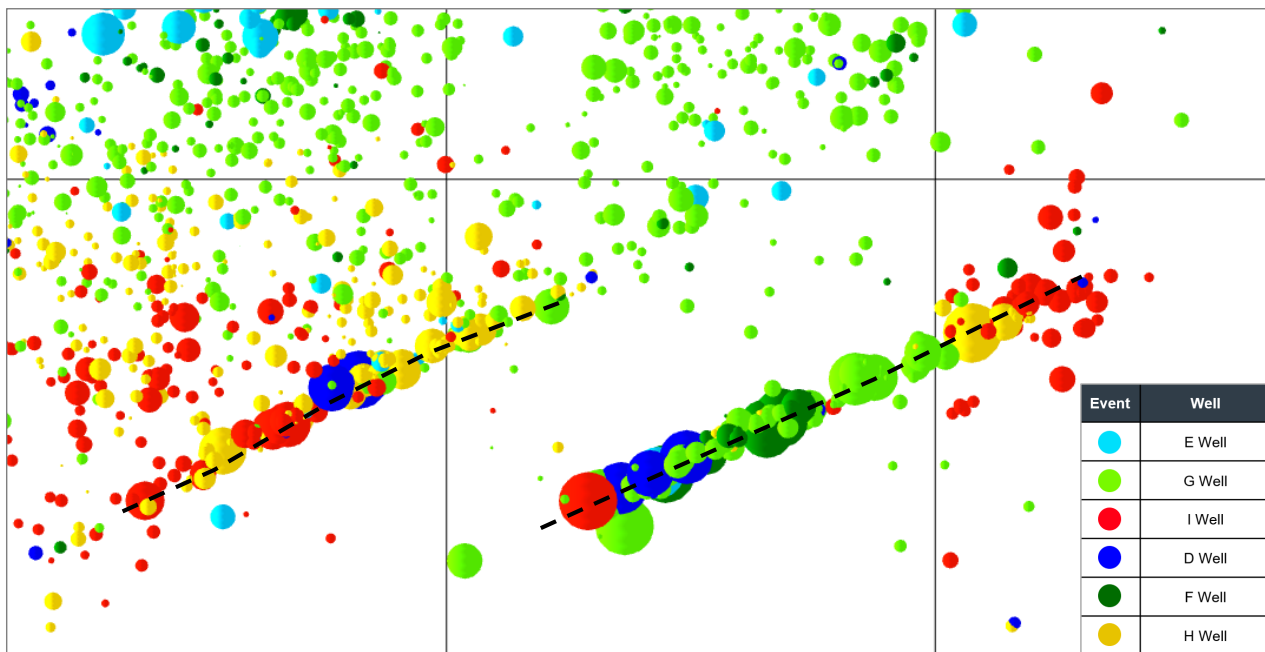


Figure 24: Interpreted Structures Activated by Different Wells

The final interpretation from induced seismic events (Figure 25a) contains a total of 77 wireframe structures (Figure 25b). There are three dominant structural orientations (Figure 25c); the most prominent of which (Set 1) is northeast-southwest. Set 1 is seen to include 63% of the interpreted seismic structures. Vertical structures are difficult to portray on a stereonet as their average dip plots close to the edge of the hemisphere (i.e., structures with a dip of approximately 90 degrees). For this reason, they are shown on a rose plot. Rose plots are a variation of the common pie chart, where the size of the wedge segment conveys the count of points.

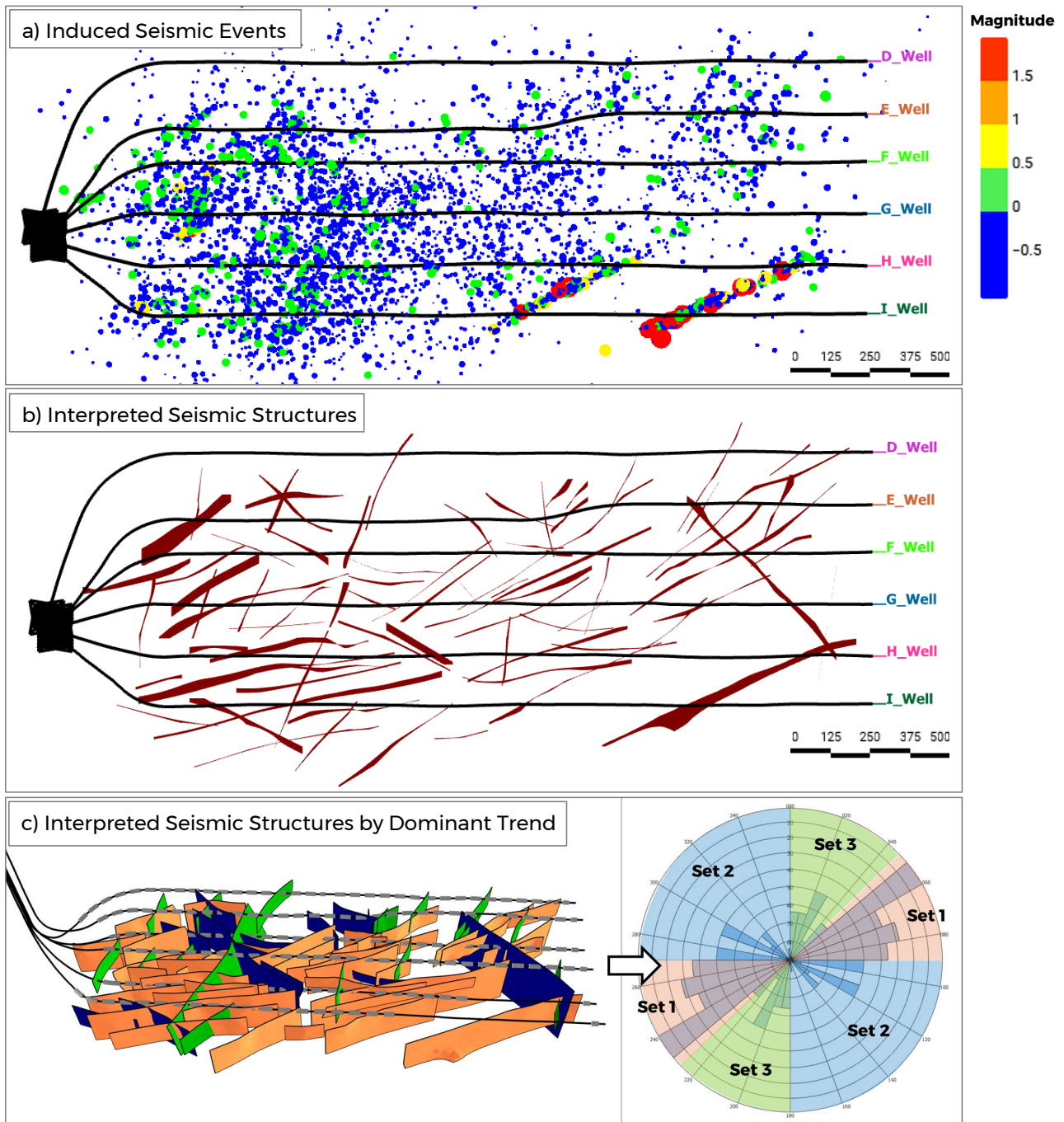


Figure 25: a) Array of Induced Seismic Events Coloured by Magnitude; b) Interpreted Seismic Structures; c) Interpreted Structures by Dominant Trend.

The 3D wireframed structures mapped into a grid in order to determine the density of structures in each Montney unit, Figure 26. For each unit, the P21 areal intensity of structures has been calculated (total length of structures/total area of sample). The highest density of structures is seen at the top of the Middle Montney (72 intersections). Not as many structures persist down into the Lower Montney (46 intersections) or up through the top of the Upper Montney (23 intersections).

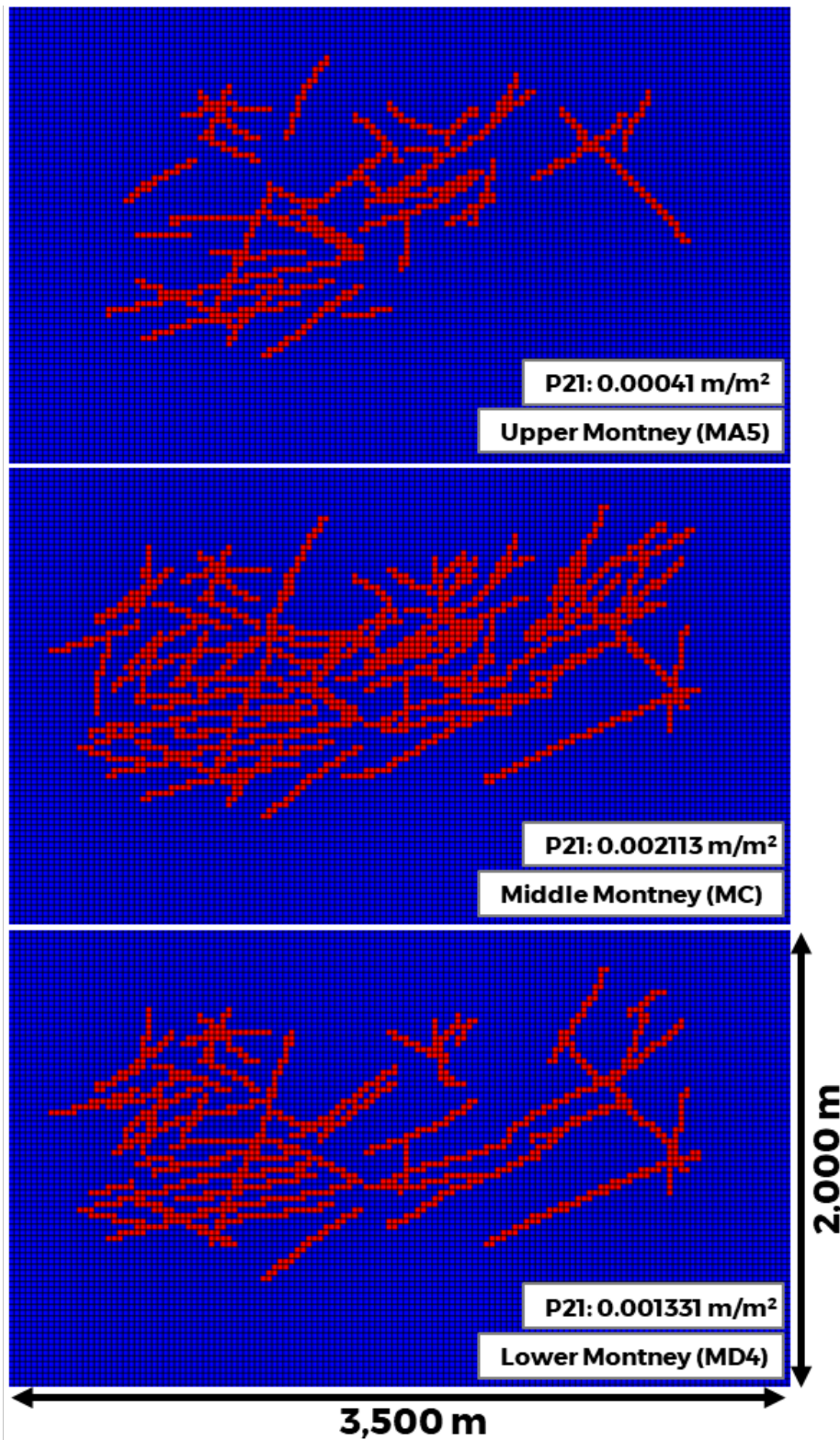


Figure 26: Calculation of P21 areal intensity for the interpreted structures at major Montney surfaces.

3.3.3 Characterisation of Smaller Scale Structures

3.3.3.1 Introduction

Geological structures reactivated with larger magnitude events (Magnitude >0.5) can be directly interpreted either because the events form clearly aligned structures or by using both spatial and temporal searching. However, a large number of the events, typically possessing smaller magnitudes, are associated with structures that can't be directly interpreted without a high degree of uncertainty. In an attempt to characterise the geometry of this smaller structural fabric that plays a role in the induced seismic puzzle, a Discrete Fracture Network (DFN) modelling approach has been applied. DFN modelling allows us to stochastically generate these smaller structures that are hard to specifically define. Stochastic modelling approaches allow the generation of multiple equiprobable realisations of these structures to be generated.

As introduced in Section 3.2.2, DFN modelling requires the geometry of stochastic structures to be defined by determining the distribution of structural size, orientation, intensity, and spatial pattern. A geocellular grid (20m x 20m x 20m grid cells) was used to populate the properties required for DFN model generation. The DFN model inputs are detailed below and summarized in the subsections below and in Table 4.

3.3.3.2 Structural Size Distribution

Seismic structure interpretation (from Section 3.3.2) provided observations with regards to structure size. The interpreted seismic structures were processed using a power law analysis technique (Rogers et al., 2016). Power law analysis reflects the common observation that many geological structures show scale invariant properties over large scale ranges. Data measured over several orders of magnitude can be plotted together and, where appropriate, a single common power law trend identified for the size of structures spanning a wide range of length scales. The power law plots display the cumulative number (count) of faults below a certain size (normalized by the estimated area over which that count was performed) against the minimum size of the observation, Figure 27a. Based on the power law analysis, a straight-line gradient of -1.4 was found. The interpreted structural lengths from Operator 3 have also been added to the power law plot and show good agreement with the Operator 1 trend. The common power law trend means that both the size distribution and intensity of structures is common between the two pads. The two datasets are regionally proximal to each other, suggestive of a common structural setting.

The purpose of the stochastic structures is to generate fractures at a scale below that which could be explicitly mapped from the interpretation of the induced events. Figure 27b shows the relationship between the lengths of the interpreted seismic structures (red) and the simulated smaller scale structures (green). The maximum size for the smaller scale structures has been taken as the 5th percentile of the interpreted structure size; this ensures that the datasets show a minor overlap but no significant duplication of fracture length. Using the minimum from the interpreted dataset would result in an abrupt transition and likely a low intensity of structures at the boundary. A radius of 20m was chosen to represent the smallest structure in the simulations. Structures smaller than 20m would not contribute heavily to the connectivity analysis but would be computationally demanding. The size distribution inputs are summarized in Table 2.

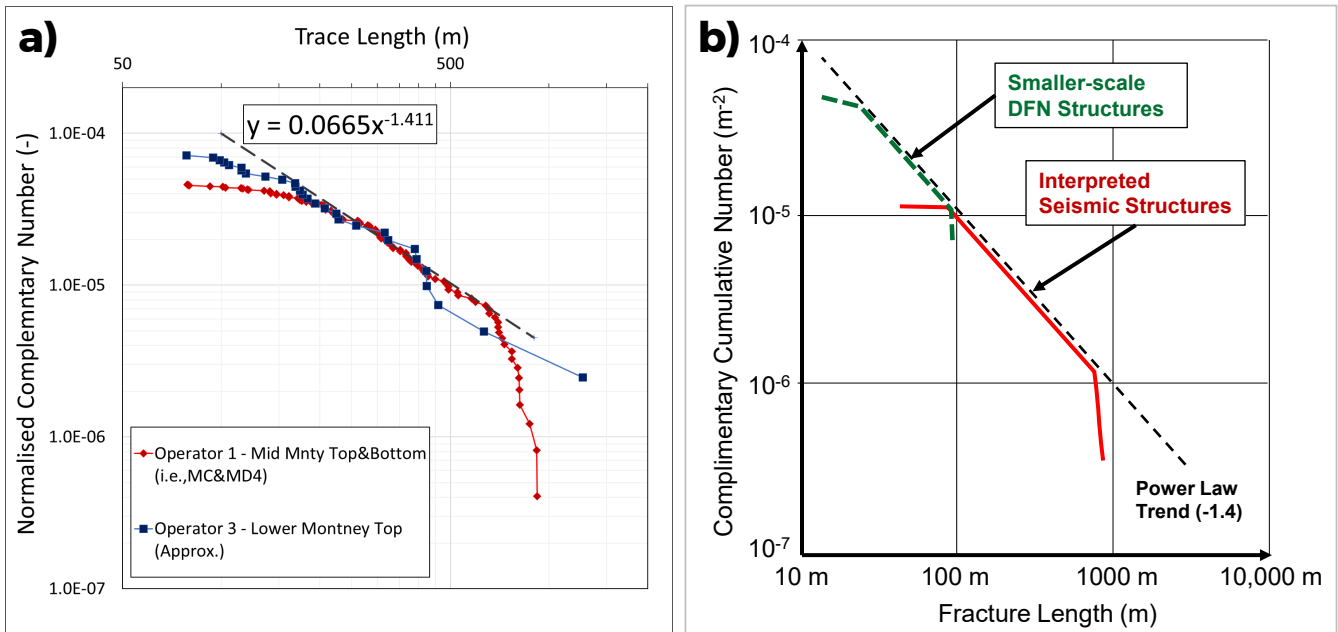


Figure 27: a) Power Law Size Distribution for OP1 in red (OP3 Displayed in blue for Comparison); b) Simulated Size Distribution range of Smaller Structures (Green) relative to the mapped structures (red)

Table 2: DFN Size Distribution

Radius (m)	Set 1	Set 2	Set 3
Minimum Simulated ¹	20 m	20 m	20 m
Maximum Simulated ²	73 m	72 m	57 m

1) A radius of 20m was chosen to represent the smallest structure in the simulations. Discussed in Section 3.3.3.2.

2) The 5th percentile size of the interpreted seismic structures. Discussed in Section 3.3.3.2.

3.3.3.3 Orientation Distribution

The seismic structure interpretation (from Section 3.3.2) provided data about variations in structure orientation across the pad. The interpreted structures were split into three sets (based upon their dominant trend) and used to define the trend (strike) and variation of the smaller (stochastic) fractures, Figure 28. A vector property of fracture strike was generated within the modelling grid for each orientation trend by mapping the local variations in orientation seen within the interpreted structures. This was used to define the local orientation of the smaller stochastic structures during generation, by locally correlating the fracture orientation to this grid property, Figure 28.

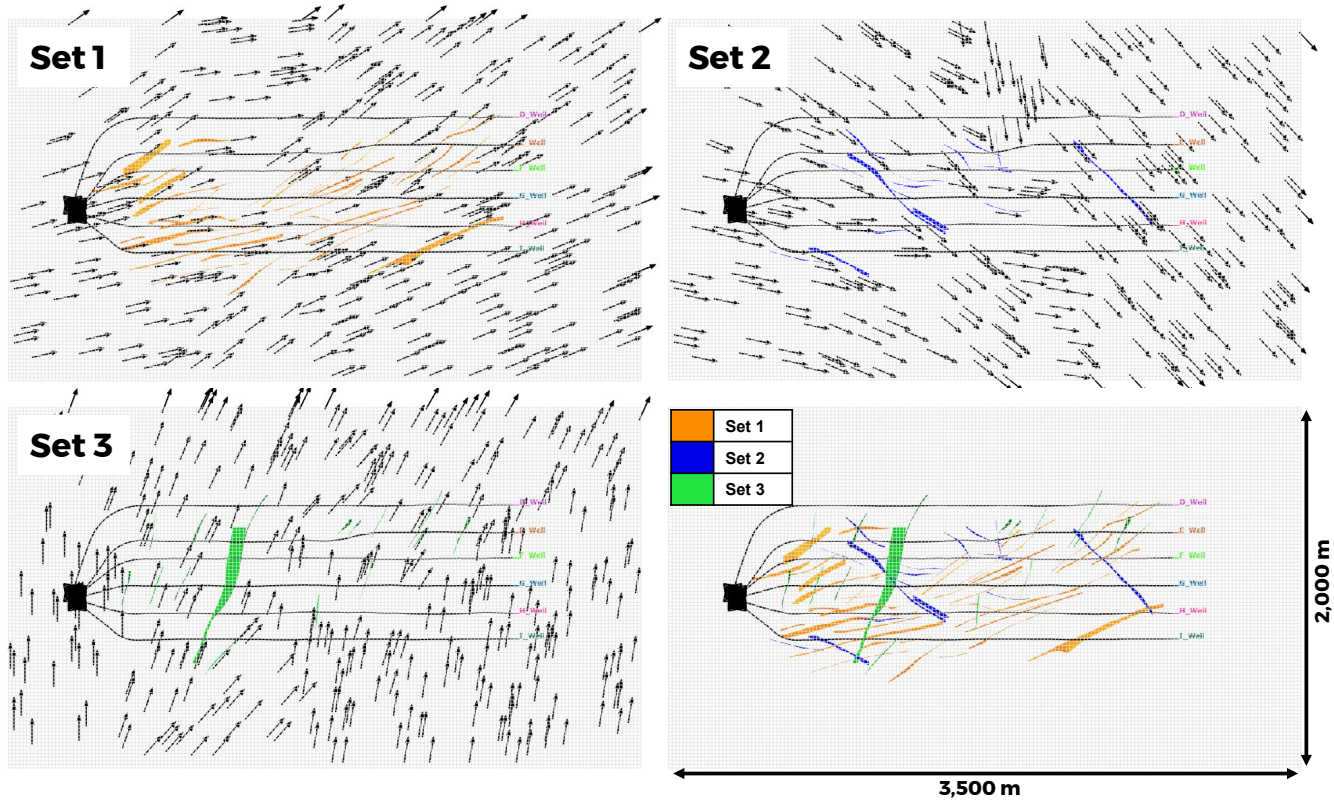


Figure 28: Structure orientation (Strike) for each set. The local vector orientation is developed from the variation of structure orientations within each set (see bottom right image) and so better reflects the overall orientation pattern for a set than simply assigning a constant trend.

To stochastically generate a fracture orientation at any point within the grid, the local fault trend is selected from the grid, the structure dip is randomly sampled from nearby interpreted faults and a small amount of dispersion is added, such that multiple realisations would produce similar but non-identical orientations. This technique is known as bootstrapping (Rogers et al 2006).

3.3.3.4 Intensity Definition

The structure intensity measurements for DFN models are described in terms of P32 (Dershowitz & Herda, 1992). P32 is a measurement of total fracture surface area per unit volume of rock [units m^{-1}]. Small scale structure intensity information was not available from drilling in the area and so it was estimated by simulation. Starting from an initial guess of P32 of 0.003 m^{-1} , the P32 was increased until the mapped connectivity from FracMan simulations showed a good agreement between observed events and simulated fractures. A total P32 of 0.005 m^{-1} was found to provide a good estimate. This total P32 was proportioned into the three identified sets based upon frequency of occurrence of mapped structures in each set, Table 3.

Table 3: Summary of Fracture Intensity Properties

Set	Population Percentage	P32 [1/m] (Total target: 0.005 m ⁻¹)
Set 1	63%	0.0031
Set 2	21%	0.0011
Set 3	16%	0.0008

3.3.4 Summary

The properties used for the stochastic structure simulations are summarised in Table 4.

Table 4: Summary of DFN Properties for Stochastic Structure Generation

	Constrained by	Properties	Comments
Structural Size	Power law analysis of mapped faults from OP1 and OP3	Power Law Slope = -1.4 Variable min & max defined from interpreted structures	Shows good agreement between both pads
Orientation	Orientation trends from mapped faults, split into three sets	Defined as mean vectors per set, dip bootstrapped from interpreted structures with dispersion added, k=80	
Structural Intensity	Estimated by simulation	Total P32 = 0.005 m ⁻¹	Total P32 divided between three sets based upon mapped intensity

The combination of the deterministic larger structures (typically defined by the higher magnitude events) and the stochastic fabric defined in reference to the larger structures but associated with the lower magnitude events, represents a reasonable structural description of the OP1 pad with which to investigate key questions of connectivity and whether this can help explain the distribution of observed induced seismic events.

3.4 Reproduction of Induced Seismicity Patterns using Connectivity Analysis

3.4.1 Introduction

The hypothesis that a critical part of the induced seismicity mechanism is the transmission of pressure from the active well along structures to critically stressed faults and other structures is further tested here. Simple connectivity tests (similar to those described in Section 3.2) can be used to test the degree of connectivity between well stages and faults and to see if that can explain the distribution.

3.4.2 Connectivity Analysis

Connectivity analysis in FracMan involves searching the DFN network, starting from the well and identifying all fractures that connect directly or indirectly to the well, up to a certain level of connection. The connection level represents how many fractures connections are involved back to the well. This represents a geometric approximation of simulating pressure diffusion away from the well towards a distal fault, with increasing connection level approximating the potential for greater pressure diffusion distance.

Four examples of the connectivity analysis on the G well are shown in Figure 29, each using identical fracture sets but with increasing connection level. The ability to identify which seismic events were associated with each well stage allowed for a detailed review of each connectivity result.

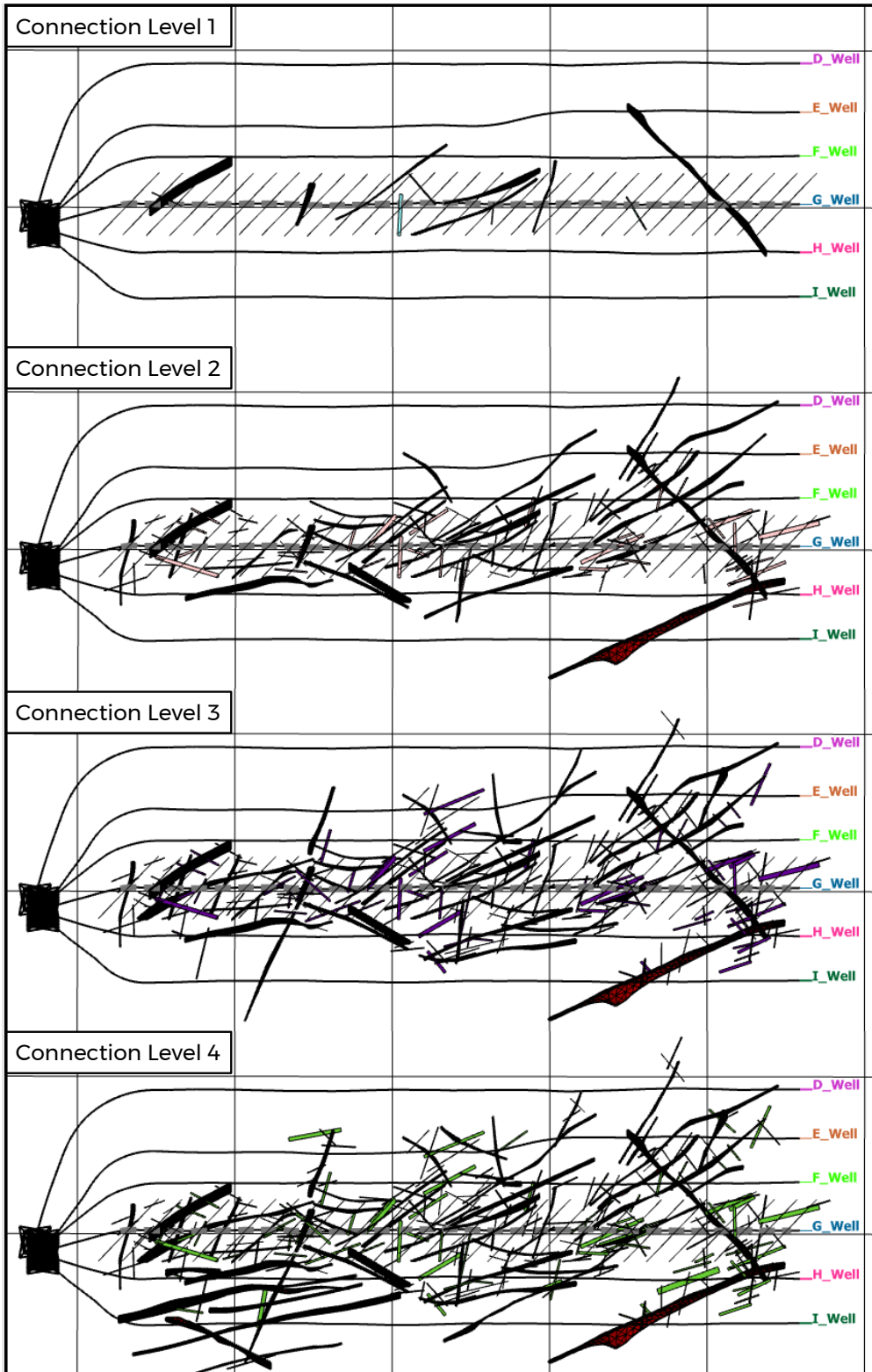


Figure 29: Example of Connectivity Analysis in FracMan on the G Well (OP1) Using Four Different Levels of Connection. Brown structures are deterministic and green are stochastic.

Using a low connection level (connection level 3) with both a low and high intensity of smaller scale fractures yielded vastly different results. Figure 30A shows an under-connected network for the D well, while Figure 30B shows an overly connected network for the E well. Whilst this difference in intensity and connectivity required by the two wells to match the distribution of induced seismicity may reflect operational controls (e.g., build up of pore pressure and stress with subsequent wells) or a need to improve the initial seismic structure interpretation. However, it also points towards a spatially variable fracture network with the highest intensity in the southwest corner of the pad.

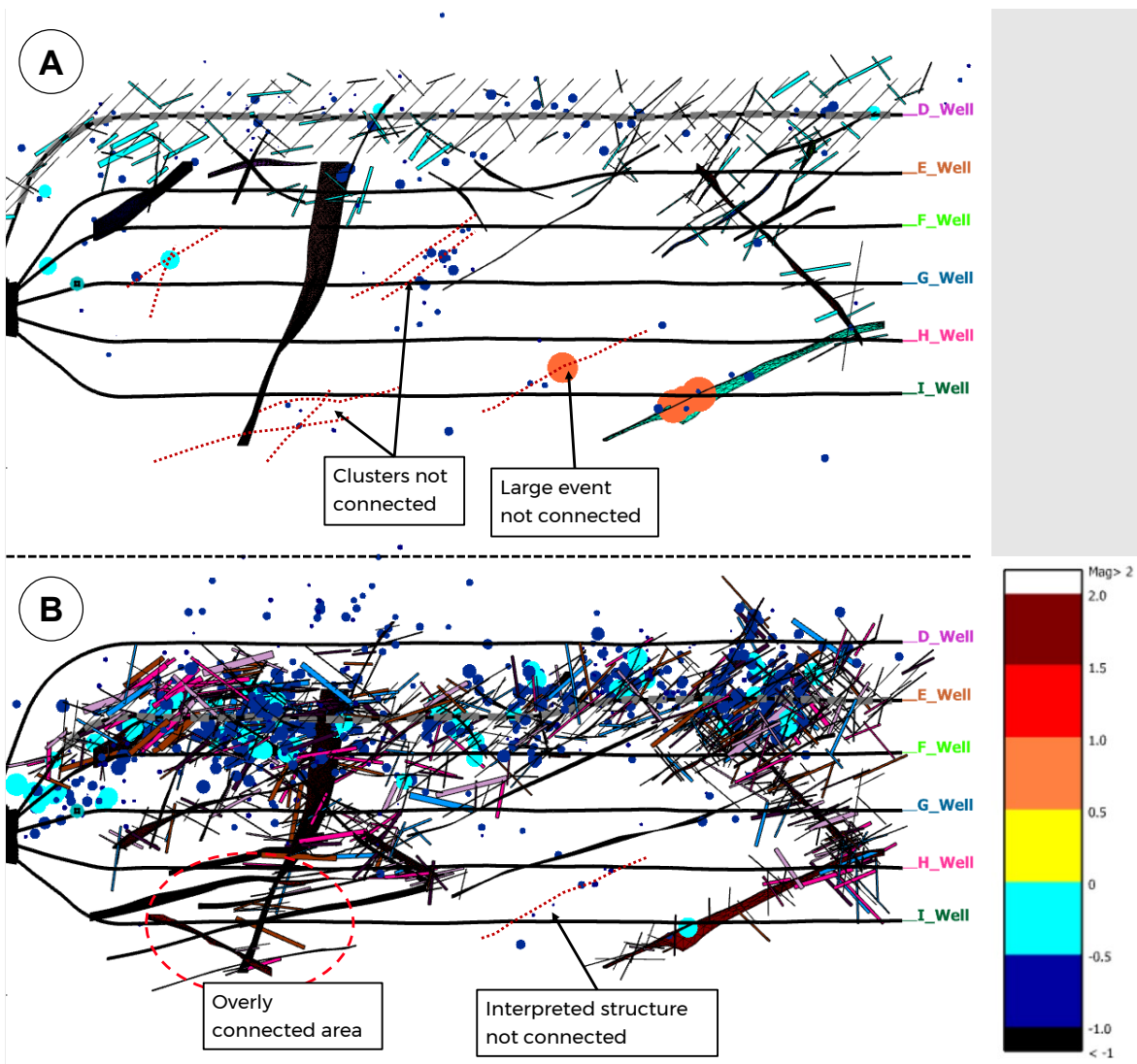


Figure 30: Preliminary Connectivity Analysis OP1: a) Well D Connectivity with Low Fracture Intensity and Low Connection Level; b) Well E Connectivity with High Fracture Intensity and Low Connection Level.

Multiple realisations were simulated in order to test the network that resulted in the most representative connectivity for each well in terms of explaining observed seismic events. There were 23 seismic events associated with the first five stages of injection in the D well, shown in Figure 31. The faults observed represent predominantly seismogenic faults that are connected to the active stages on the well. However, there are some additional aseismic structures that have been added based upon a need for connectivity.

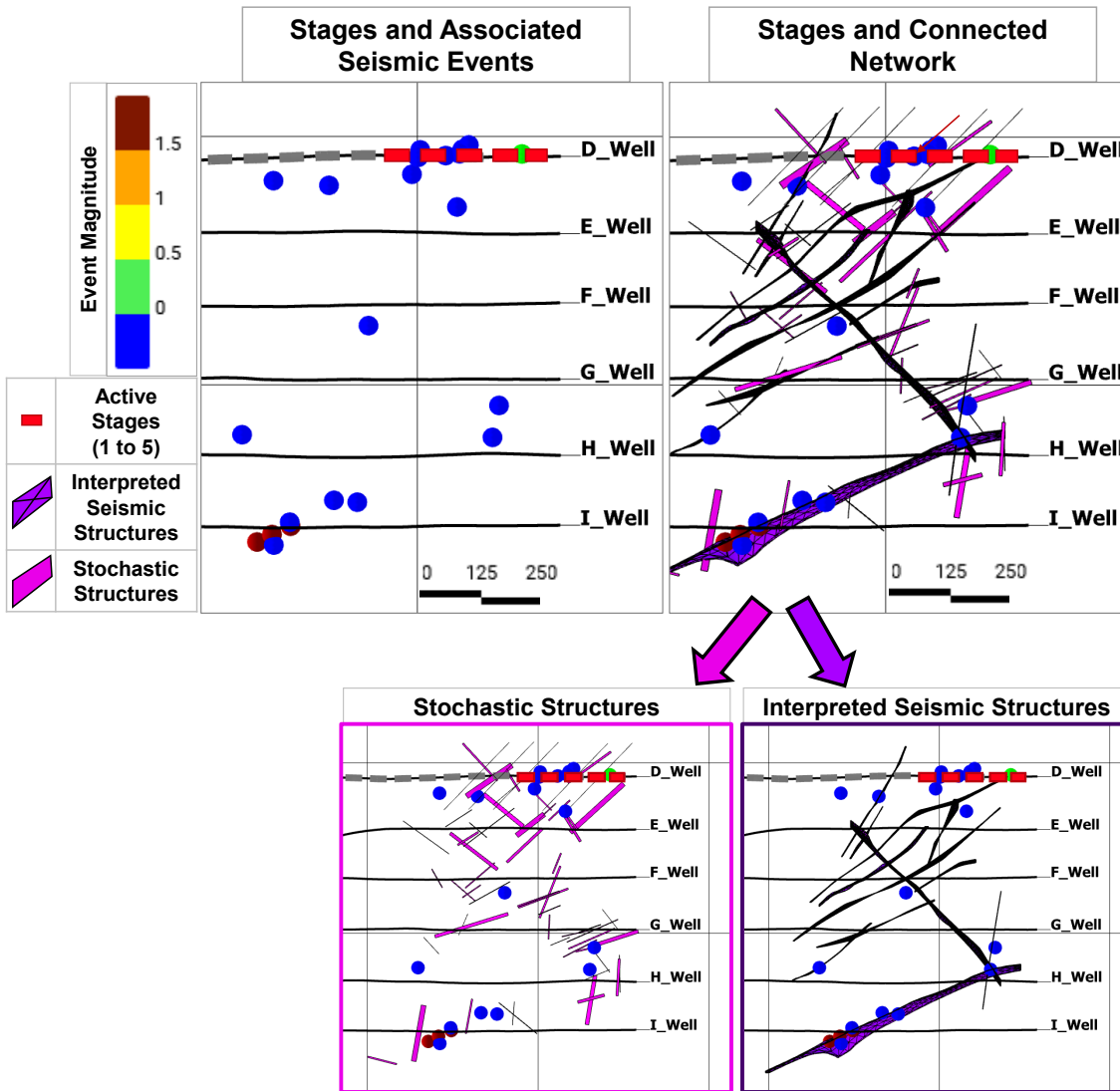


Figure 31: Example of Connectivity Analysis; D Well, Stages 1 to 5. Induced Events are Coloured by Magnitude. Connected Network is Split into Stochastic (light purple) and Interpreted (dark purple) Structures to Highlight their Relationship to the Seismic Events.

For the I well, multiple stages at the toe of the well were skipped in order to help mitigate the reactivation of the large faults in the southeast of the pad (Figure 32A). It can be seen in Figure 32B that previous wells, predominantly F and G well, had activated the large NE-SW structures near the toe of the I well. However, one significant seismic event (magnitude >1.5) was recorded during the I well completion in an area that was not being actively stimulated (Figure 32C). The effectiveness of the stage skipping strategy can be tested using the DFN model. When multiple DFN models are search for connections from the I well stages to the main NE-SW fault, with a connection level of 5, the fault associated with the large event was only geometrically connected to the I well in 5% of realizations (1 out of 20) (Figure 33). This could be considered as a probability of failure of 5%. An increase in the connection level, to connection level 7, was required in order to reactivate the large seismic structure in every realization (20 out of 20). A connection level of 7 represents a long flow path but one that is consistent with the observed seismicity patterns. The increase in connection level indicates that skipping stages as a means of mitigation did significantly reduce the connectivity of the network.

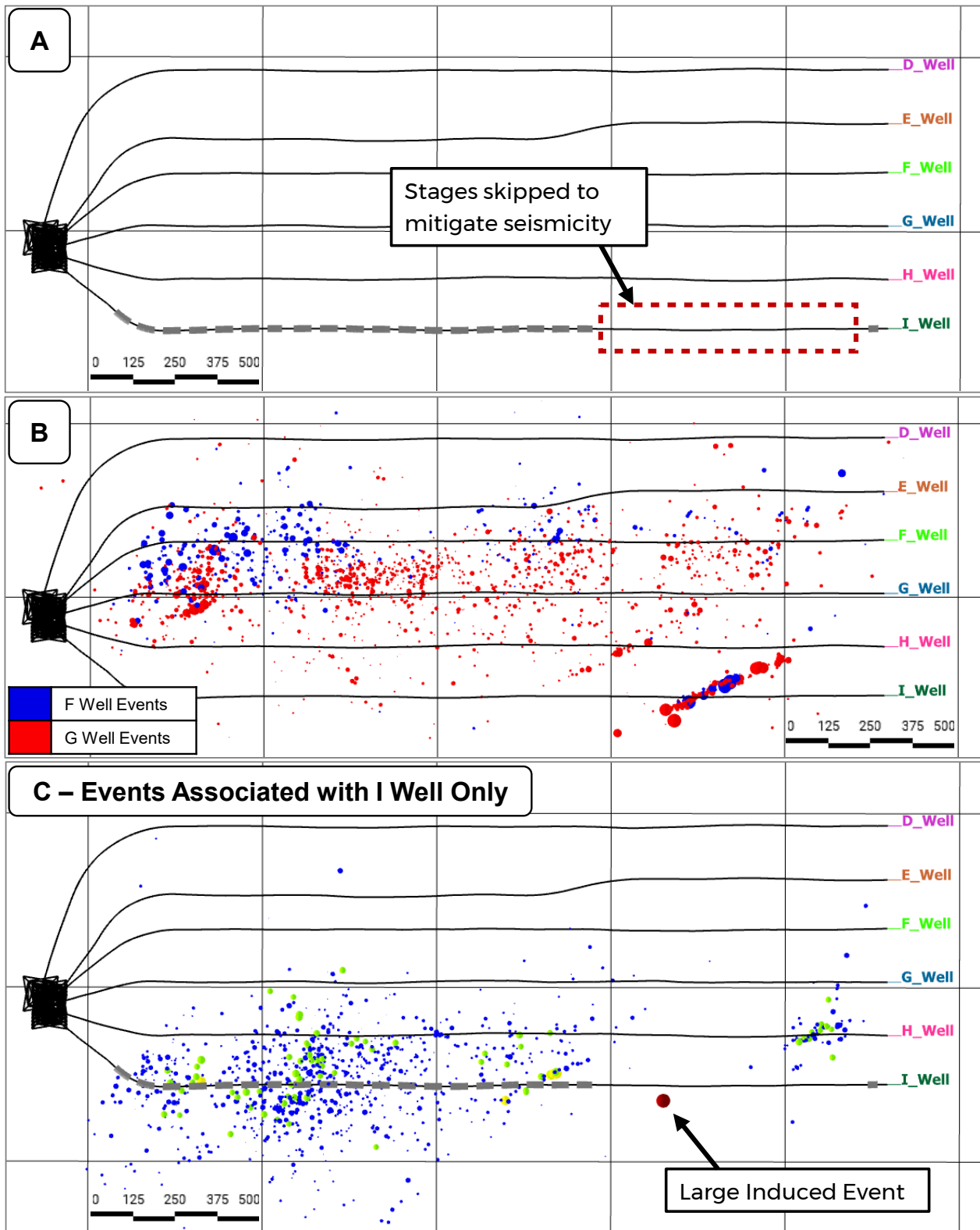


Figure 32: a) Toe of the I Well Not Stimulated to Mitigate Seismicity; b) Induced Seismicity Associated with F and G Well Injection; c) Induced Seismicity Associated with I Well Injection.

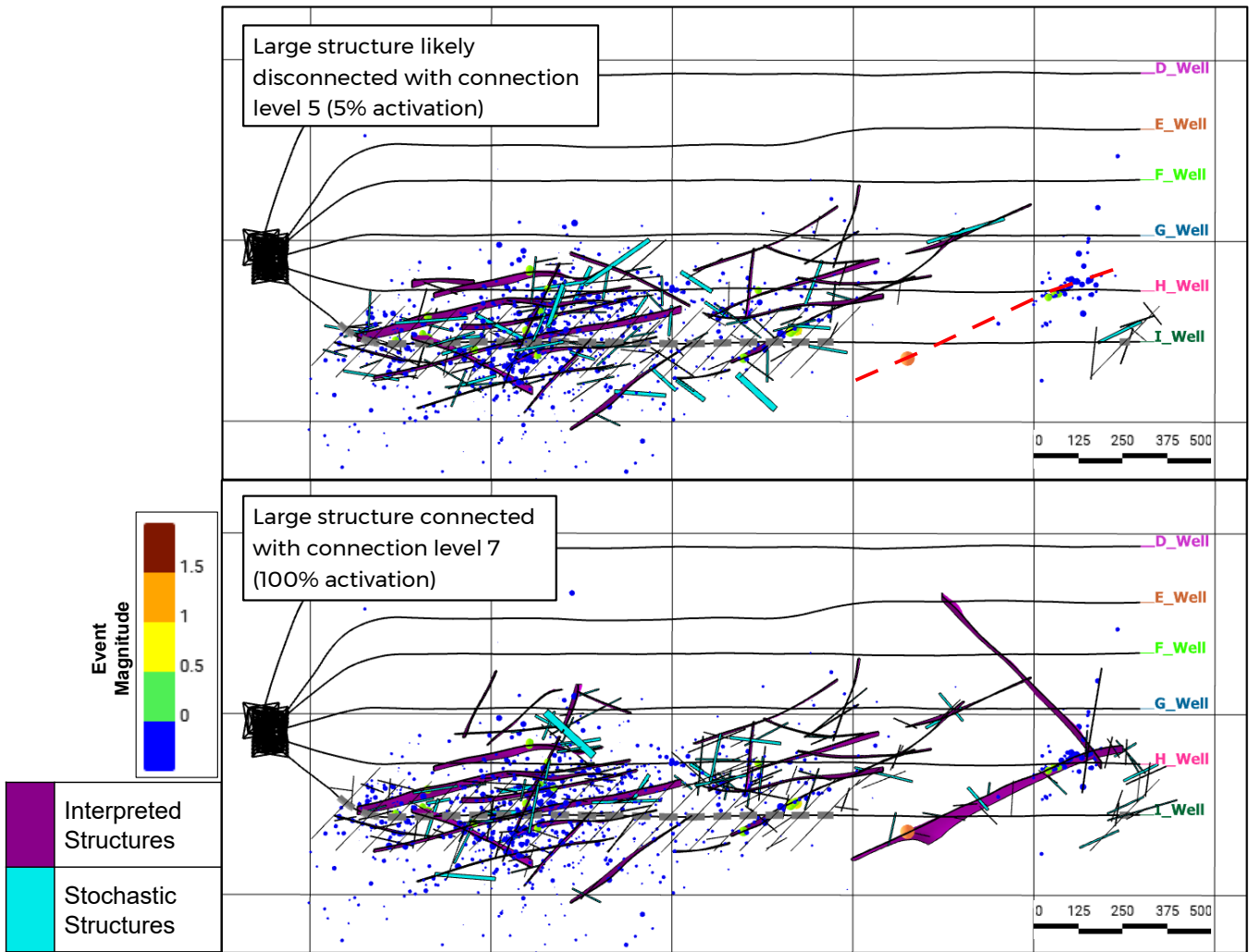


Figure 33: I Well Connectivity Analysis, Results using Connection Level 5 and 7 Displayed. Events Sized and Coloured by Magnitude.

3.4.3 Summary

These simple connectivity tests have demonstrated that the observed patterns of seismicity can be explained by structurally sensible networks of structures. Multiple realizations of the connectivity models were simulated with varying fracture intensities and connection levels which gave a measure of the likelihood of connection. These results suggested some revisions to the initial interpretation, mainly in terms of segmenting some larger structures to prevent excessive connections.

Characterisation of the connection level for each well was carried out on a geometric level, as a simple proxy for distance. Analyses on the I well indicate that although the problem of connectivity can be approached geometrically, that consideration must be given to hydraulic processes. More comprehensive analysis into the connectivity of interpreted structures was carried out in Section 4.0 where hydraulic diffusivity is considered as a pathway property.

4.0 CHARACTERISATION OF PATHWAY PROPERTIES BY HYDRAULIC DIFFUSIVITY

4.1 Introduction

Effort has been made to estimate the hydraulic properties of reservoir structures from the spatio-temporal distribution of fluid-injection induced seismicity (Talwani & Acree, 1985; Shapiro et al., 1997, 1999, 2002; Talwani et al., 2007; Igonin et al., 2021). These studies show that the dominant triggering mechanism of induced seismicity is governed by diffusion of the pore-fluid pressure perturbation from the injection source. In other words, the fluid pressure build-up used to initiate and propagate a hydraulic fracture with each injection stage, will leak off and diffuse once it intersects a pre-existing fracture network. This broader pressure front then increases the probability of intersecting and disturbing distal structures and inducing shear slip and seismicity.

If the configuration of fluid injection into a borehole is approximated by a point source of pressure perturbation into an infinite heterogeneous anisotropic poroelastic fluid-saturated medium, then, based on Biot's equations of poroelasticity (Biot, 1962), the spatio-temporal evolution of the pressure perturbation P can be described by the following differential equation of diffusion (Shapiro et al., 2002):

$$\frac{\partial P(x_{ij},t)}{\partial t} = \frac{\partial}{\partial x_i} \left[D_{ij} \frac{\partial P(x_{ij},t)}{\partial x_j} \right] \quad \text{for } i, j = 1, 2, 3. \quad (1)$$

Here t is the time, D_{ij} is the components of the hydraulic diffusivity tensor, and x_{ij} are the components of the radius vector from the injection point to an observation point inside the medium. Relaxing Eq. (1) by simplifying the medium to a homogeneous and isotropic medium yields:

$$\frac{\partial P}{\partial t} = D \nabla^2 P \quad (2)$$

Shapiro et al. (1997) stated that Eq. (2) could completely describe the spatio-temporal pressure evolution of the medium using the time- and pressure-independent hydraulic diffusivity D . Following the seismicity-based reservoir characterization approach (Shapiro et al., 1997, 1999, 2002) a reasonable heuristic field scale magnitude estimate of D can be determined by analyzing the spatio-temporal characteristics of induced events. For this, $r - t$ diagrams are computed which show the radial distance r between the event location and the injection point, as a function of the elapsed time t since the beginning of the injection. In such diagrams, clouds of hydraulically induced events show a characteristic parabolic signature which can be understood as a footprint of the underlying hydraulic transport. This characteristic signature of pore pressure diffusion induced seismicity is evaluated by the so-called triggering front. The triggering front represents a spatial surface which approximately separates regions in which the pressure has already caused induced seismicity. Thus, in $r - t$ plots, such a separation surface is described by the outermost envelope which also expresses the triggering front for the simplified medium (Shapiro et al., 1997):

$$r = \sqrt{4\pi Dt} \quad (3)$$

Hence, fitting this square root of time-dependent parabola as an envelope of injection phase induced events allows to heuristically estimate the field-scale in-situ hydraulic diffusivity of a given seismically active rock volume.

In multi-stage hydraulic fracturing operations, the pressure perturbation source of each event cluster must be identified first so that it would be possible to plot the seismic events distribution in $r - t$ space. This can be done with the application of temporal filtering to the data (Figure 34). By doing so, the events would be assigned to the stage n if they were recorded between the start of injection for this stage up to the start of injection for the next stage ($n+1$), see Figure 34a and b. The intrinsic assumption of this filtering is that the events are triggered only by the pore pressure perturbation of that active stage. An example of a typical $r - t$ plot of fluid-injection induced seismicity for a hydraulic fracturing stage from a well pad in the Horn River basin of BC is shown in Figure 34c (Shapiro et al., 1997, 1999, 2002; Hummel & Shapiro, 2013; Goebel & Brodsky, 2018; Cesca et al., 2021).

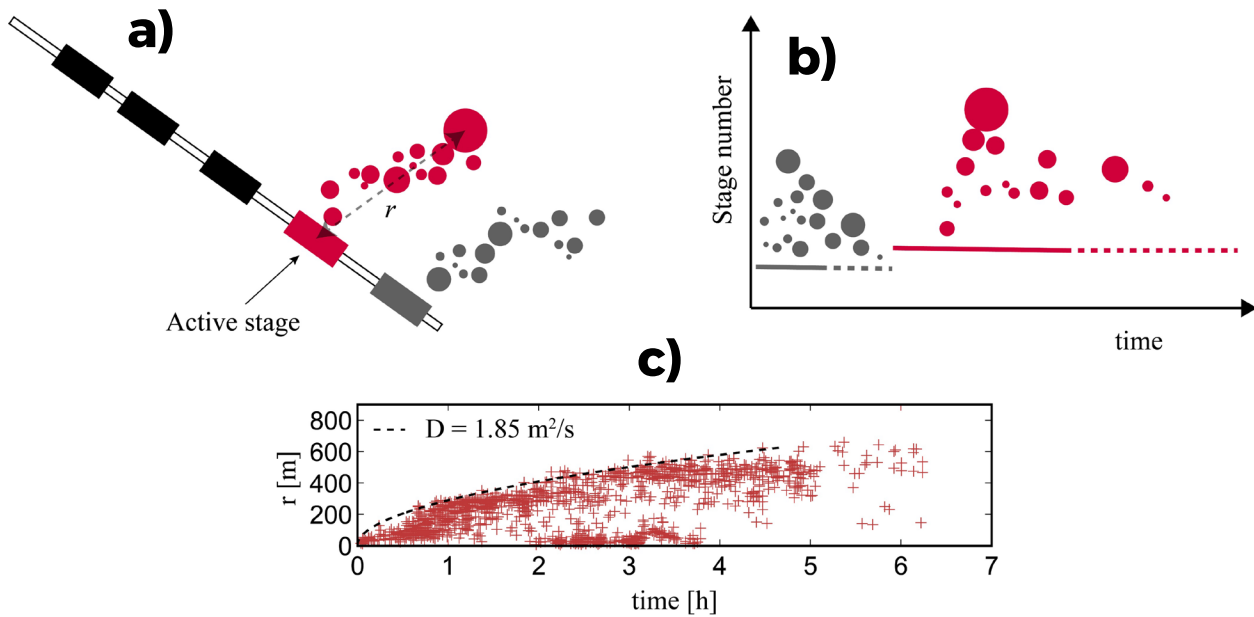


Figure 34: Calculation of the spatio-temporal distribution of fluid-injection induced seismicity events. a) Illustration of the active stage (red) and radial distance r (dashed line) to the biggest event from the injection source. Also shown is the previous stage and associated events (grey). b) Illustration of the temporal filtering of events, assigning them to the active stage (red) or previous stage (grey), where the solid and dashed horizontal lines show the fluid injection and shut-in intervals, respectively. c) Typical seismic event distribution pattern of a hydraulic fracturing stage in the Horn River, BC (modified after Hummel and Shapiro, 2013).

From the estimated diffusivity values, we can calculate the effective hydraulic permeability of the medium. The diffusivity and medium permeability, k , are related to each other by (Jaeger et al., 2007):

$$D = \frac{k}{\mu\phi C_t} \quad (4)$$

Where μ , C_t and ϕ are the viscosity of the fluid saturating the medium, the overall bulk compressibility of the saturated medium (i.e., the pore-fluid and the rock matrix and fractures), and the porosity of the medium, respectively.

There is a fundamental difference between the hydraulic diffusivity in a fault hosted in an impermeable rock (e.g., shale), and the hydraulic diffusivity of a porous medium in that the pressure fronts will be at different distances from the injection point, this shown by a cartoon illustration in Figure 35. In fact, injecting the same amount of fluid with the same rate over the same time will result in much longer pressure front propagation from the injection point for the case of fault (r_F) relative to porous medium (r_P), and thus $D_F > D_P$. In addition, comparing the storage capacity and permeability of these two cases, the fault has a lower storage capacity and typically a higher permeability in contrast to a porous medium (i.e., $S_F \ll S_P$ and $k_F \gg k_P$, respectively) which all lead to $D_F > D_P$. Note that a high hydraulic diffusivity in the context of fractured reservoir means that the pressure perturbation is only focused in a few partially connected structures and the pressure front transfers faster to distal structures and results in induced seismic events out of the zone of HF design. Whereas a low hydraulic diffusivity in such context means that the pressure diffused in a larger volume of intersected connected structures which only transfers pressure perturbation to structures close to the HF stage. Such differences has been appreciated in this study for the first time.

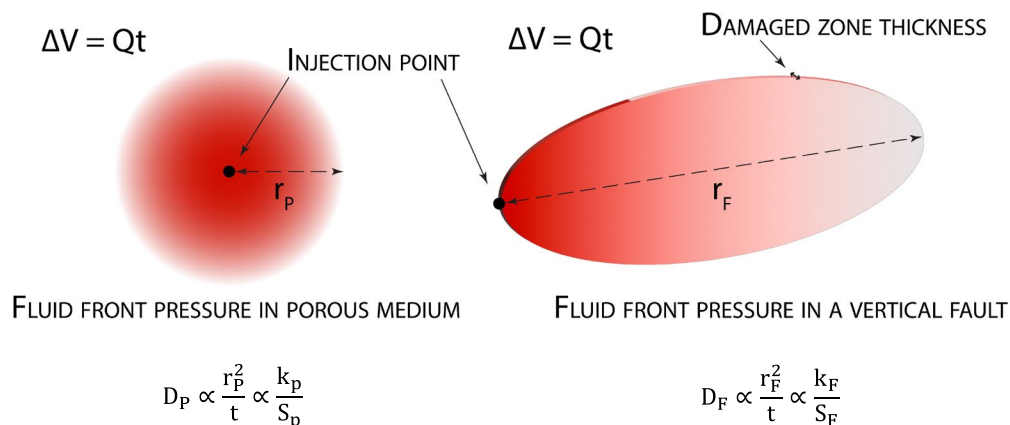


Figure 35: The difference between pressure perturbation front in a porous medium (left) and a vertical fault (right). For the same amount of injected fluid (ΔV) with the same rate (Q) over the same time (t), the pressure fronts distance from the injection point are shown by the two headed dashed arrows ($r_P \ll r_F$). k_F , S_F and k_P , S_P refer to permeability and storage coefficient of fault and porous media, respectively ($S_F \ll S_P$ and $k_F \gg k_P$).

In the following, the hydraulic diffusivity analyses are carried out for OP3 and OP1 different completion techniques and geological structure characteristics. These empirical analyses help us understand the mechanism of induced seismicity in the study area and allow the development of potential mitigation measures, discussed in Section 6.0 of this report.

4.2 Hydraulic Diffusivity Analysis – OP3 (Open Hole Completion)

The events from the OP3 dataset were assigned to the active stages for OP3 using the temporal filtering procedure explained in the previous section. From the wells in this pad, a close match was found between the three wells completed in the Lower Montney and the event occurrence times (see Figure 7). Hence, only these wells were considered in the hydraulic diffusivity analysis of OP3. Figure 36a illustrates a full spatio-temporal view of the seismic events in 3D and r-t space for well A2. The events distribution in r-t space is mostly enveloped by diffusivity values of $D \geq 5 \text{ m}^2/\text{s}$. It is noted that for one of the stages, shown in Figure 36b, the induced seismicity distribution does not show the classical parabolic signature. The analyses and interpretation for this unusual seismic event distribution pattern in r-t space will be discussed in Section 4.4.

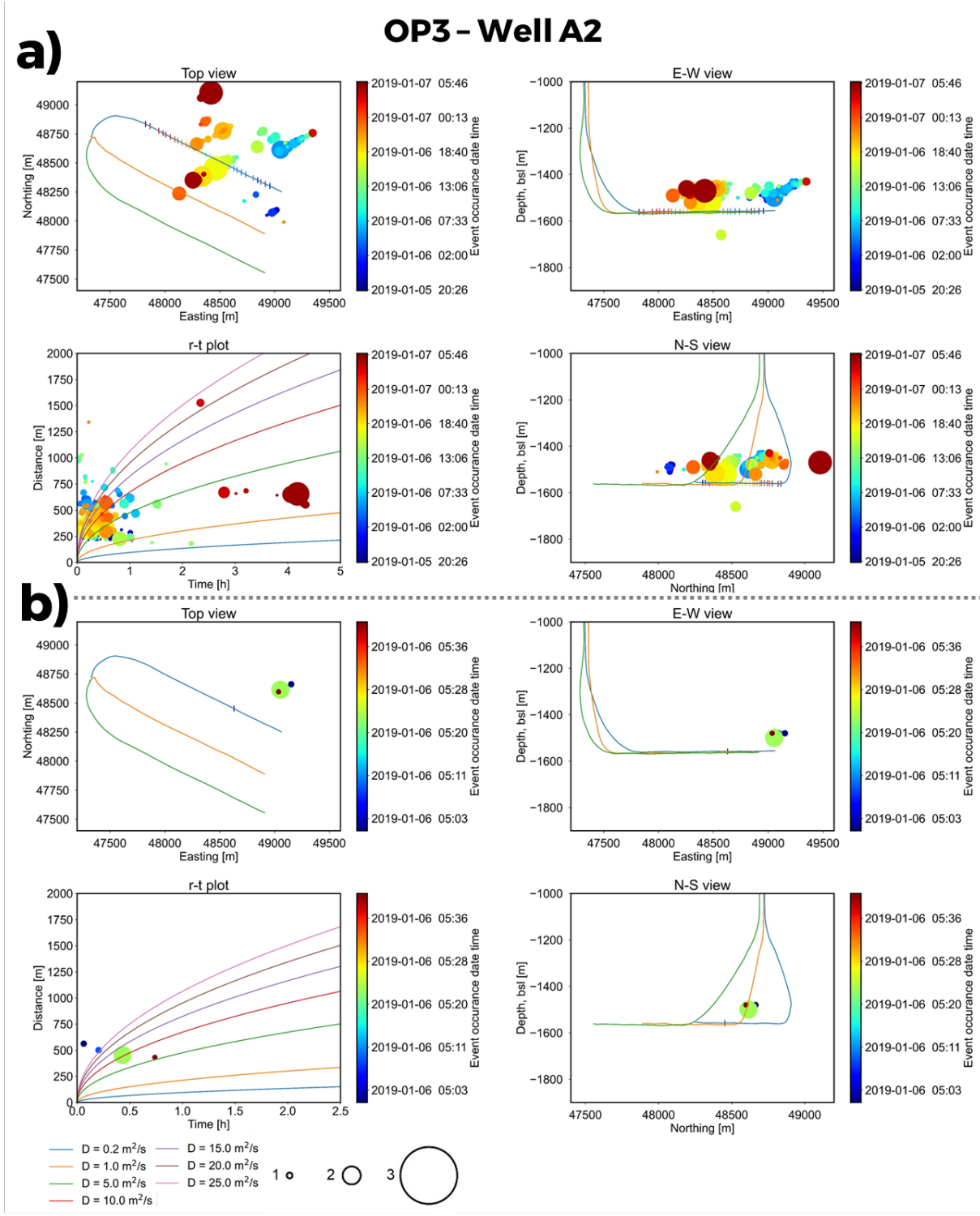


Figure 36: a) Full view of the induced seismicity with the corresponding r-t plot for well A2 of OP3. b) Example of stage 12 of well A2 that does not follow classical parabolic signature in r-t space. Events are colored by the time of occurrence (color bar). The size of each point scales to the seismic event magnitude as indicated in the legend.

Figure 37 begins by analyzing the relationship between hydraulic diffusivity and seismic event magnitude (see bar graph). Two findings are observed in the data. The first is that the majority of small magnitude events ($M_w < 2$) are associated with low diffusivity values. The second is that larger magnitude events (i.e., $M_w \geq 2$; see blue bars) are associated with both low and high diffusivity values relative to the median value of $4.5 \text{ m}^2/\text{s}$. One explanation for this relates to the influence of fracture intensity. Two scenarios are illustrated in Figure 37: one involving a fracture network (i.e., high fracture intensity and storativity) and one involving a single fracture (i.e., low fracture intensity and storativity). These are shown by the solid blue lines in the left and right illustrations, respectively. Otherwise, both scenarios assume a similar fault orientation and shear strength, the same injected fluid volume, and the same radial distance from the injection source to the event hypocenter (i.e., $r_1 = r_2$).

For the scenario involving a higher fracture intensity (Figure 37, left illustration), leak off results in a longer pressure perturbation travel time from the injection source to the seismogenic fault. Recalling that the diffusivity is describing the ratio of the permeability, k , and the storage capacity, S , of the medium (Jaeger et al., 2007), a fluid pathway consisting of more structures would result in a larger S (i.e., $S_1 > S_2$ in the figure) and therefore lower diffusivity values. The corresponding pressure front disturbing the fault would be larger in area (increasing the potential for more seismic events) but smaller in pressure magnitude (resulting in smaller magnitude seismic events). A larger magnitude event would still be possible but would require longer times for higher pressures to build up on the fault (i.e., $t_1 > t_2$). This is contrasted against the scenario involving a lower fracture intensity (Figure 37, right illustration), which results in a more intense pressure interacting with the fault (higher pressure acting across smaller fault surface area), favouring the triggering of a large magnitude event relative to smaller magnitude events.

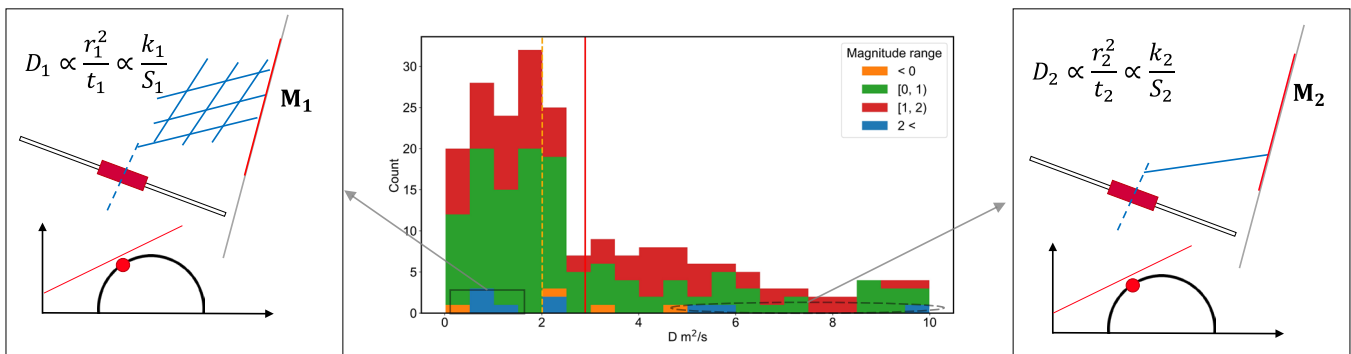


Figure 37: Plot of distribution of hydraulic diffusivity values coloured according to their corresponding seismic event magnitude ranges, for the first phase of OP3 data. The solid red and dashed orange vertical lines correspond to the mean ($4.5 \text{ m}^2/\text{s}$) and median ($2.3 \text{ m}^2/\text{s}$) values, respectively. The adjacent illustrations depict a potential explanation for the observed trends between low diffusivity values (left) and high diffusivity values (right). See text for explanation. For both illustrations, the grey solid line represents the susceptible/activated fault, the red segment of the fault shows the shear slip extent corresponding to a larger magnitude event ($M_w \geq 2$), the blue solid lines represent the fracture intensity transporting the fluid pressure, and the dashed blue line shows the hydraulic fracture intersecting the fracture network propagated from the active hydraulic stage (red box). Also shown is the Mohr-diagram of the reservoir in-situ stress state where the red dot represents the normal and shear stress acting on the fault relative to its shear strength (red line). Both scenarios depicted assume the same fault orientation and strength, injection volume, and radial distance from the injection source (i.e., $r_1 = r_2$).

Figure 38 shows the locations and magnitudes of the detected induced seismicity events from the first phase of OP3 data. Also shown are the interpreted structures derived from these events, and superimposed on these are the calculated hydraulic diffusivity values. The blue ellipse highlights the part of the reservoir where $M_w \geq 2$ events are associated with lower diffusivity values (i.e., $D < 4.5 \text{ m}^2/\text{s}$). It can further be seen that this is also where the reservoir is more highly fractured. This corresponds with and supports the explanation given for the left illustration in Figure 37. The red ellipse in Figure 38 represents the structures with high diffusivity values associated with similar event magnitudes, and is where the reservoir is not as highly fractured. This corresponds with and supports the explanation given for the right illustration in Figure 37.

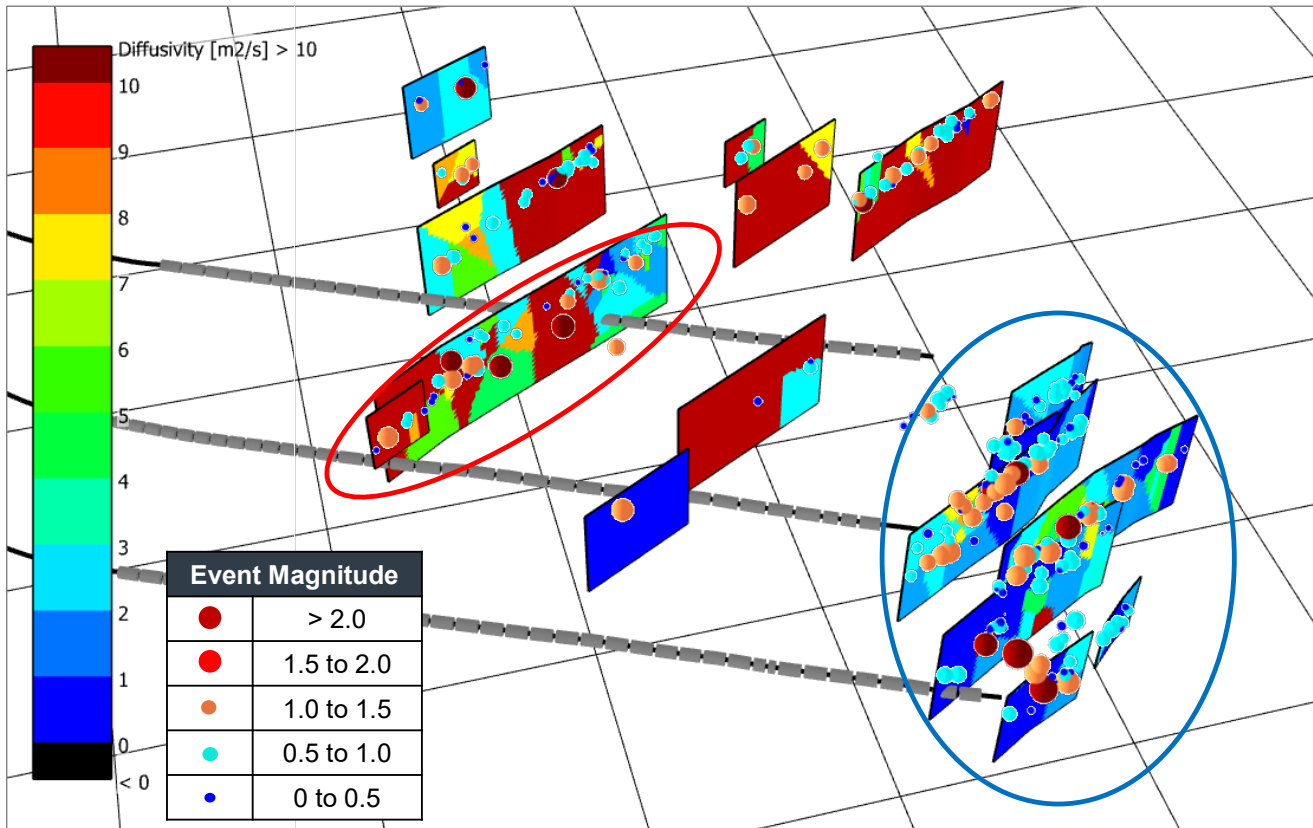


Figure 38: The event distribution and hydraulic diffusivity values on the identified structures for the first phase of injection in the OP3 dataset. The red ellipse bounds hydraulic diffusivity values of $4.5 \text{ m}^2/\text{s}$ and greater, and the blue ellipse bounds diffusivity values lower than $4.5 \text{ m}^2/\text{s}$ (i.e., highly fractured).

Rearranging Eq. (3), one could calculate the hydraulic diffusivity value for each individual event in the catalog using $D = r^2/4\pi t$. With this equation one could estimate the permeability of the structures that are transporting the fluid pressure to the event hypocenter. The hydraulic diffusivity of the fracture network using Eq. 4 is related to the permeability, k , and fracture porosity, ϕ_f , of the structures, the overall viscosity of the fluid mixture, μ_t , the total compressibility, C_t , of the fracture system, and the saturating fluid, with $D = k/\mu_t\phi_f C_t$ (Jaeger et al., 2007). In fact, even though the permeability is a function of the effective stress (e.g., Min et al., 2004), the calculated value is the overall average effective permeability where using the “cubic law”, one could calculate the effective hydraulic aperture, a_h , of the system by $k = a_h^2/12$ (Witherspoon et al., 1980; Kessels & Kück, 1995). This effective hydraulic aperture is the equivalent representation of a fracture by parallel plates, which yields the comparable fracture permeability. In addition, it is typically expected that the aperture values of the fracture network follow a log normal distribution (e.g., see Renshaw, 1995; Lyons et al., 2015 and references therein).

However, deviation from the cubic law for heterogeneous fracture apertures with significant fracture roughness are reported in the literature (Zimmerman & Bodvarsson, 1996; Konzuk & Kueper, 2004) and consequently a host of reformulations and empirical corrections have been proposed. For instance, fluid flow and transmissivity studies of fracture networks in the SKB Äspö Hard Rock Laboratory in Sweden resulted in the suggestion of an empirical relationship between transmissivity, T , and a_h , given as $T \propto a_h^2$ (Uchida et al., 1994; Dershowitz et al., 2003) with the exponent ranging from 1 to 3.

Therefore, we considered a range of 1 to 3 for the exponent in our analyses, and our sensitivity analyses suggest $D \propto a_h^{2.5}$ or $k_f \propto a_h^{2.5}$ yields the most reasonable aperture values for both operators, and hence we used $k_h = a_h^{2.5}/12$ to estimate the aperture from the calculated fracture permeability. Note that the terms hydraulic aperture and aperture, as well as effective fracture permeability and permeability are used interchangeably throughout this report.

The properties and proportion of fluids saturating the fracture networks are uncertain, therefore an even mixture of both gas and water is assumed, with a fracture porosity of $\phi = 10\%$ (Lyons et al., 2015). The compressibility and viscosity of the fluid was calculated based on equations proposed by Batzle and Wang (1992) with the assumption that the gas has a specific gravity of 1, and native brine has a salinity of 100,000 ppm, at a temperature of 100°C and a pressure of 35 MPa (these values are representative of general conditions in unconventional reservoirs in the WSCB; e.g., see Dunn et al., 2012; Lyster et al., 2017). The properties of the mixture values were averaged with the injected slick water (i.e., $4 \times 10^{-3} Pa.s$ or $4 cP$), which yields an overall viscosity value of $\mu = 2 \times 10^{-3} Pa.s = 2 cP$. The compressibility of the fractured siltstone-shale formation was estimated based on reported values in the literature (Kessels & Kück, 1995; Li et al., 2022), resulting in an overall compressibility for a fracture saturated with a mixture of fluids of $C_t = 5 \times 10^{-8} Pa^{-1} = 0.34 \times 10^{-5} Psi^{-1}$. It should be noted that the goal is not to provide a definitive constraint on the transport properties of the fracture network, but to demonstrate that reasonable values for the hydro-mechanical properties of the fractures can be interpreted from the data, which can transport pressure perturbations to activate structures away from the active injection stage.

The effective hydraulic permeability of each structure with their corresponding hydraulic aperture are shown in the form of boxplots in Figure 39. Also, the overall distribution of these properties along with their mean and median values are represented in the same figure. The median permeability and aperture of the structures resolved for the reservoir targeted by OP3 are larger than $10^4 mD$ and $10^{-4} m$, respectively.

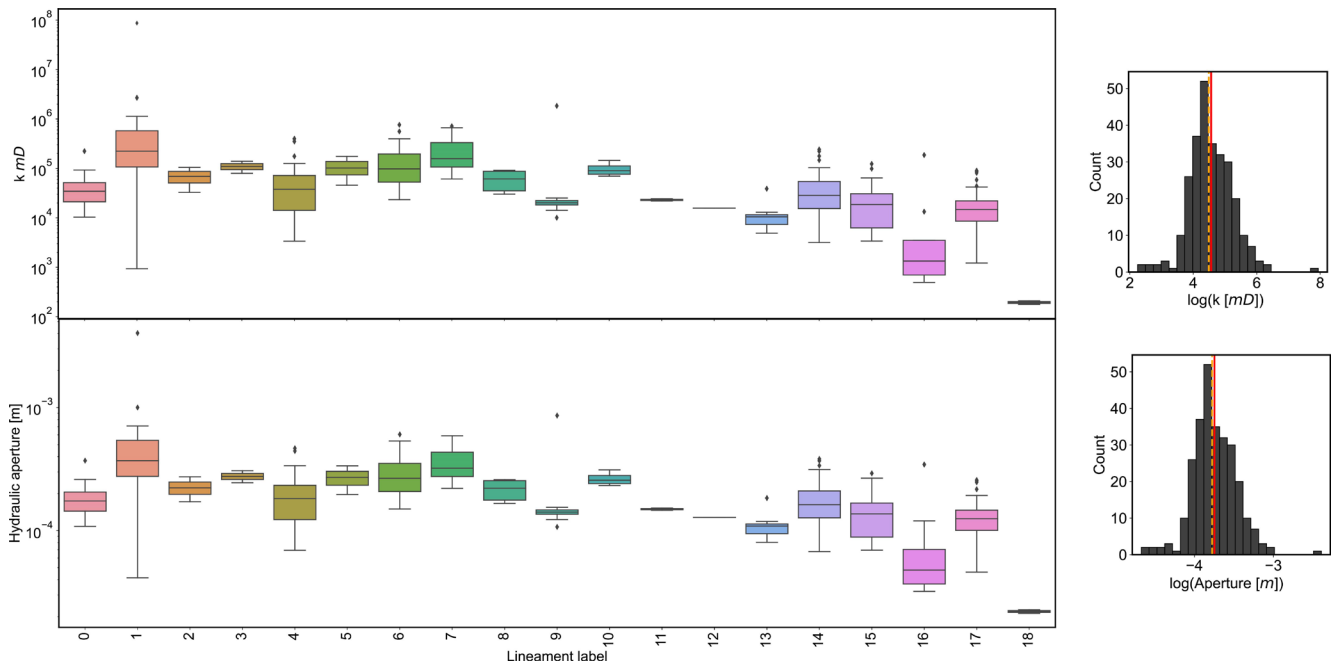


Figure 39: Values of effective hydraulic permeability and aperture calculated for structures activated during the first phase of OP3 fluid injection. The box plots show the properties for each structure, and the overall distributions of the properties are shown to the right, where the solid red and dashed orange vertical lines illustrate the mean and median values, respectively.

In order to examine the relative magnitude of the cumulative recorded seismic energy release compared to the injected hydraulic energy, we use “seismic injection efficiency”, I_{eff} , introduced by Maxwell et al. (2008). From this, the injected hydraulic energy can be calculated using (Goodfellow et al., 2015):

$$E_H = \int_{t_1}^{t_2} P(t)V(t)dt \quad (5)$$

where P and V are the measured well-head pressures and injection rates, respectively. The seismic injection efficiency for time interval $[t_1, t_2]$ is calculated as the ratio of the cumulative radiated energy of seismic events that occurred in the specified time period and hydraulic energy E_H . The seismic energy release can be calculated from the reported moment release using the equation proposed by Kanamori (1978).

The full injection data was available for OP3, and these were used to estimate I_{eff} values for well A2 (Figure 40a, c). The activation of the distributed fracture network can be compared with other empirical data of reported seismic injection efficiency from various sites reported in the literature, which for new hydraulic fractures are typically $I_{eff} < 10^{-5}$ (Maxwell et al., 2008; Maxwell, 2011; Goodfellow et al., 2015; Kwiatek et al., 2018). It is noted that the calculated values for OP3 well A2 are up to 3 orders of magnitude larger. In fact, these values are within the range of hydraulic shear stimulation of pre-existing fractures in geothermal reservoirs (see Kwiatek et al., 2019). Therefore, such values support the hypothesis that structures were activated in shear during the injections from OP3 well A2.

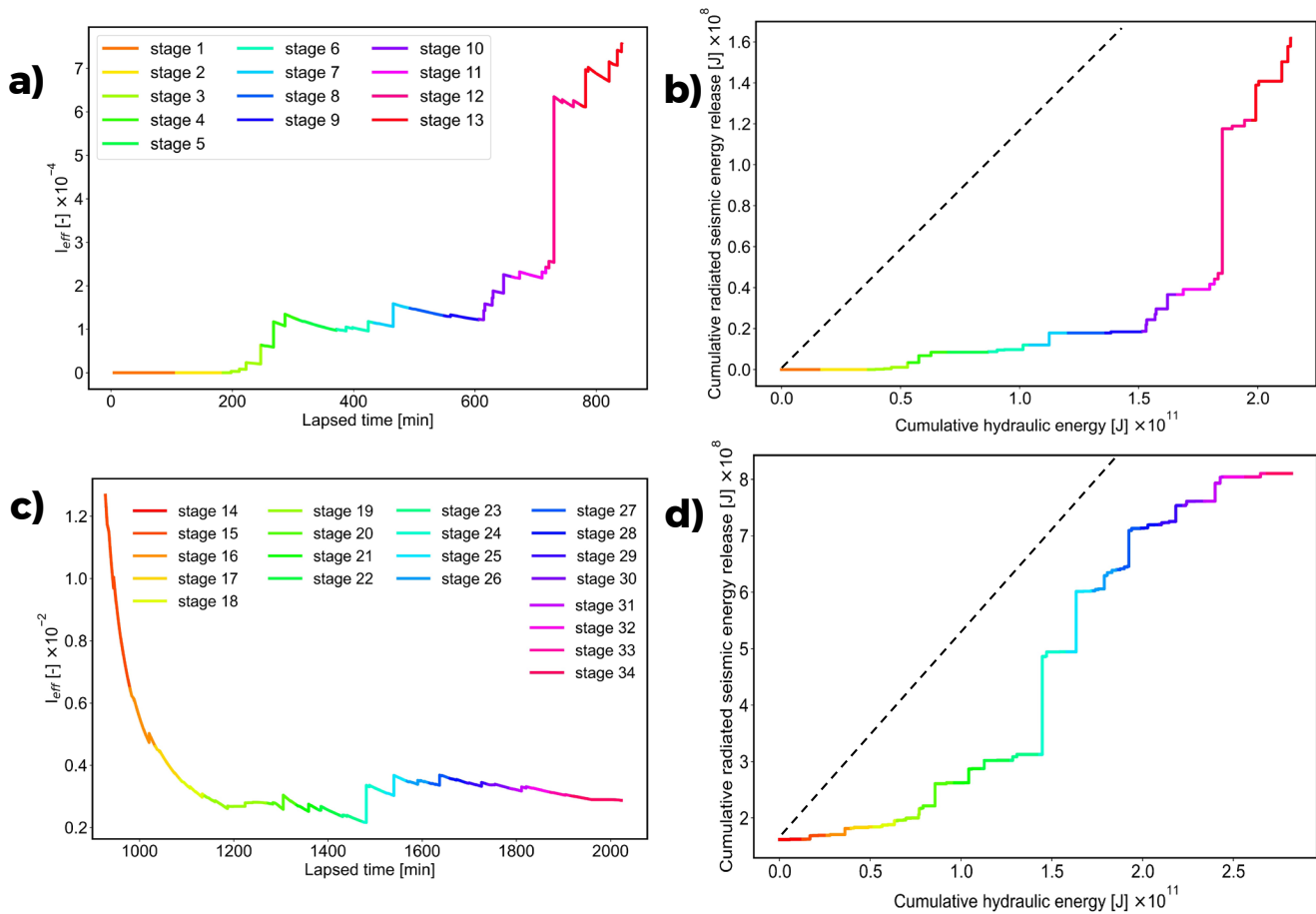


Figure 40: Seismic Energy Efficiency Calculated for OP3 Well A2 with Full Hydraulic Stimulation. a) and c) Show the hydraulic seismic injection efficiency, I_{eff} , as function of lapsed time since the injection start. b) and d) illustrate the cumulative radiated seismic energy release relative to the input hydraulic energy into the reservoir; the dashed black line represents the case where all the injected hydraulic energy is transformed to radiated seismic energy.

Moreover, Figure 40b and d illustrate the relative cumulative seismic energy release recorded by the seismic sensors to the input hydraulic energy. The dashed black lines represent the case where all of the input hydraulic energy is transformed into seismic energy. This could only happen if there were no energy loss due to friction (i.e., the fractures open in tensile mode I) and fluid leak-off, amongst other factors (Maxwell, 2008). As can be seen in Figure 40, we observed that from stage 12 onwards the energy release is getting closer to the full hydraulic energy being transformed to seismic energy release (i.e., the black dashed line). This may suggest that, even though the seismic array is not very sensitive (i.e., it could only pick up and record events of magnitude - 0.26 or larger), most of the hydraulic energy is released as shear slip. Thus, the results point more towards the direct effect of fluid pressure increase as the primary mechanism for the induced seismicity recorded in this case, as opposed to other possible mechanisms like aseismic slip (e.g., Eyre et al., 2019).

4.3 Hydraulic Diffusivity Analysis – OP1 (Cased Hole Completion)

Similar to OP3, diffusivity data analyses were carried out for OP1 and the results are presented in this section. All six wells for this pad were completed in the Upper Montney (Figure 20), and all recorded induced seismicity events were associated with the different wells and their respective stages using the temporal filter previously described in Section 4.1.

Figure 41 represents the event distributions associated with the hydraulic fracturing of well F of OP1 where the events and stages are colored by their corresponding recorded time and stage initiation, respectively, and the size of each datapoint is proportional to the magnitude of the seismic event. In the corresponding $r - t$ plot, the triggering fronts follow two discernable curves. One is associated with the early stages near the toe of the well (about $5 \text{ m}^2/\text{s}$) and the other corresponds with the later stages closer to the heel of the well (about $1 \text{ m}^2/\text{s}$).

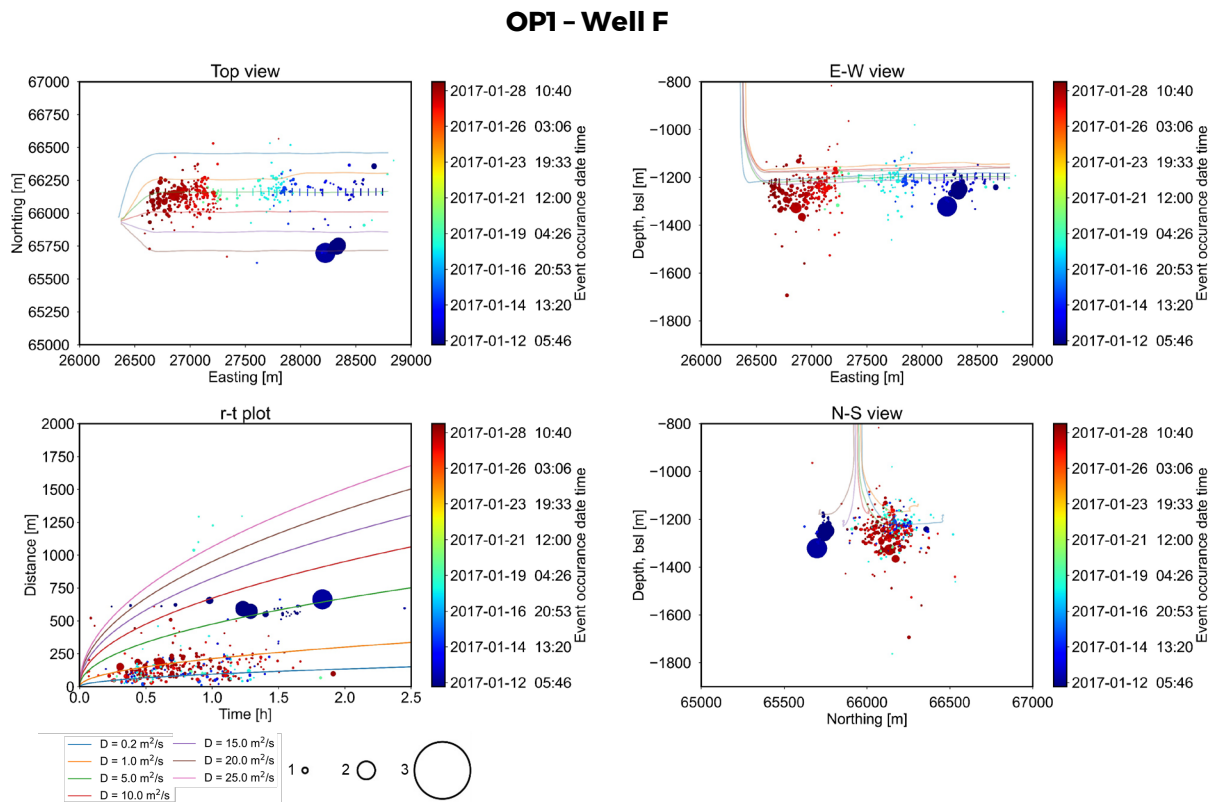
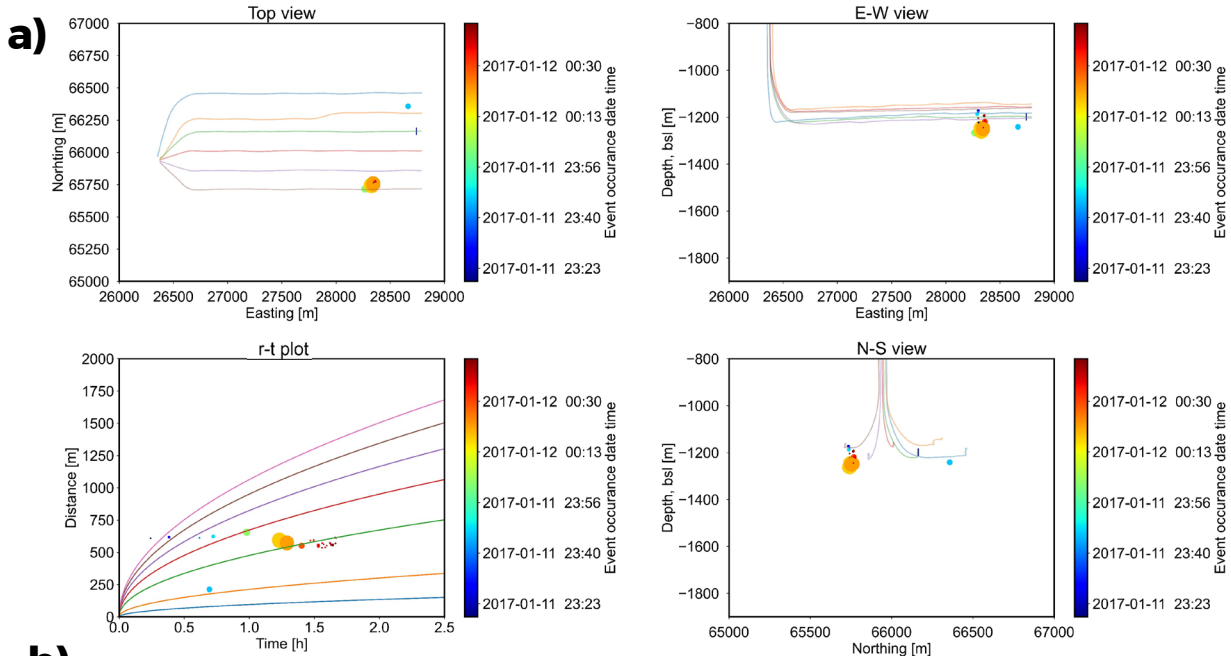


Figure 41: Full view of the induced seismicity recorded for well F of OP1 with the corresponding r-t plot. Events are coloured by their time of occurrence and the size of each point shows the seismic event magnitude, as denoted in their respective legends. Note that the top left figure (“Top View”) displays Wells D to I from top to bottom, respectively.

We selected two hydraulic fracturing stages and their corresponding seismic events distribution, and plotted them in Figure 42. In Figure 42a, one can see similar seismic event distribution in $r - t$ space as observed previously in Figure 36b for OP3 with high diffusivity values (i.e., $D \geq 5 \text{ m}^2/\text{s}$). However, the classical parabolic seismic event distribution can also be observed in Figure 42b, which is similar to that reported by Hummel and Shapiro (2013) for a hydraulic fracturing stage in the Horn River (see Figure 34c) with similar low hydraulic diffusivity values of approximately $1 \text{ m}^2/\text{s}$. These two distinguished seismic event distributions in $r - t$ space provide us with a unique opportunity to compare the data and study the values to gain knowledge on the seismic event magnitudes, hydraulic diffusivities, operational factors and their relationship to each other.

OPI - Well F - Stage 1



b) OPI - Well F - Stage25

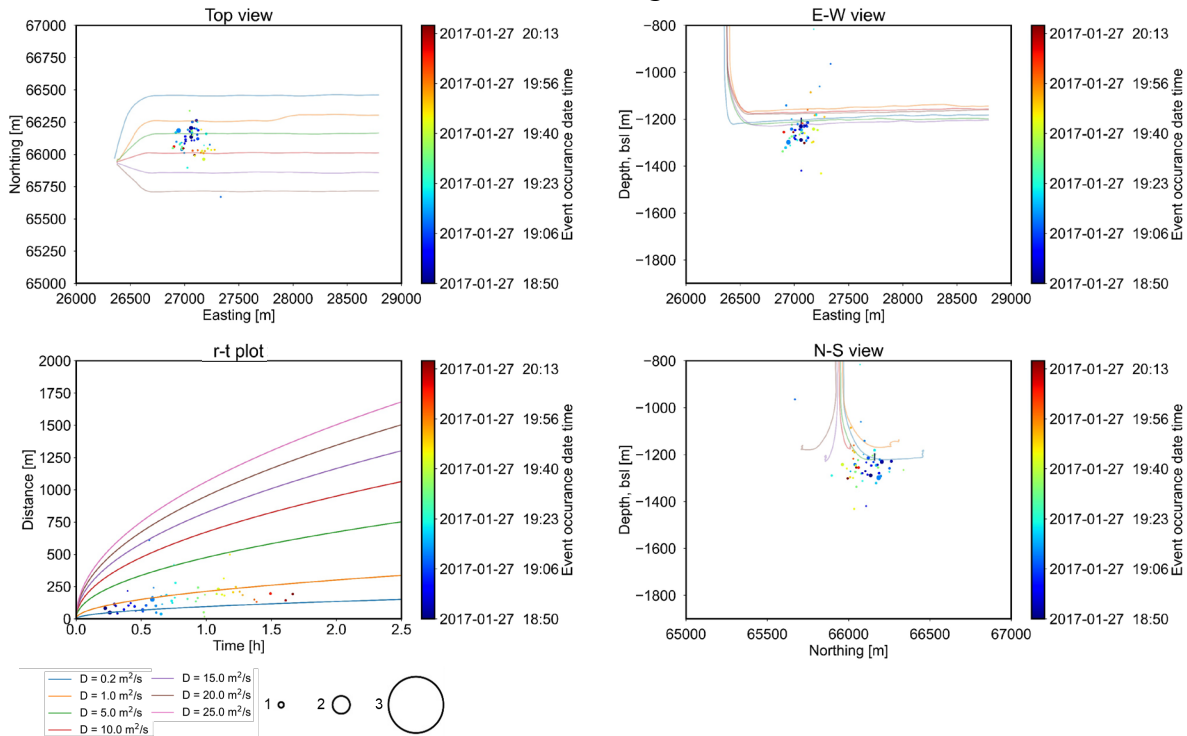


Figure 42: a) Full induced seismicity event distribution for stage 1, well F, OP1, with its corresponding atypical seismic event distribution in r-t space. b) Seismic event distribution for stage 25 with its corresponding classical parabolic distribution in r-t space. Events are coloured by their time of occurrence and the size of each point shows the seismic event magnitude, as denoted in their respective legends.

The hydraulic diffusivity distribution for OP1 is plotted and colored by event magnitude in Figure 43, following the same procedures as previously discussed for Figure 37. The data suggests that low hydraulic diffusivity values are linked to a higher number of low magnitude seismic events. This is believed to be caused by fluid injection into a reservoir volume with a high fracture intensity, as inferred from the diffusivity values being less than the mean (indicated by the red vertical line). Injection pressure diffusion in densely connected fractures, with varying shear strengths, can result in seismic moment release through a large number of small shear slips. This is in contrast to higher hydraulic diffusivity values, which as discussed for the results for OP3 (see Figure 37), a lower number of events indicates a lower fracture intensity or partially connected structures.

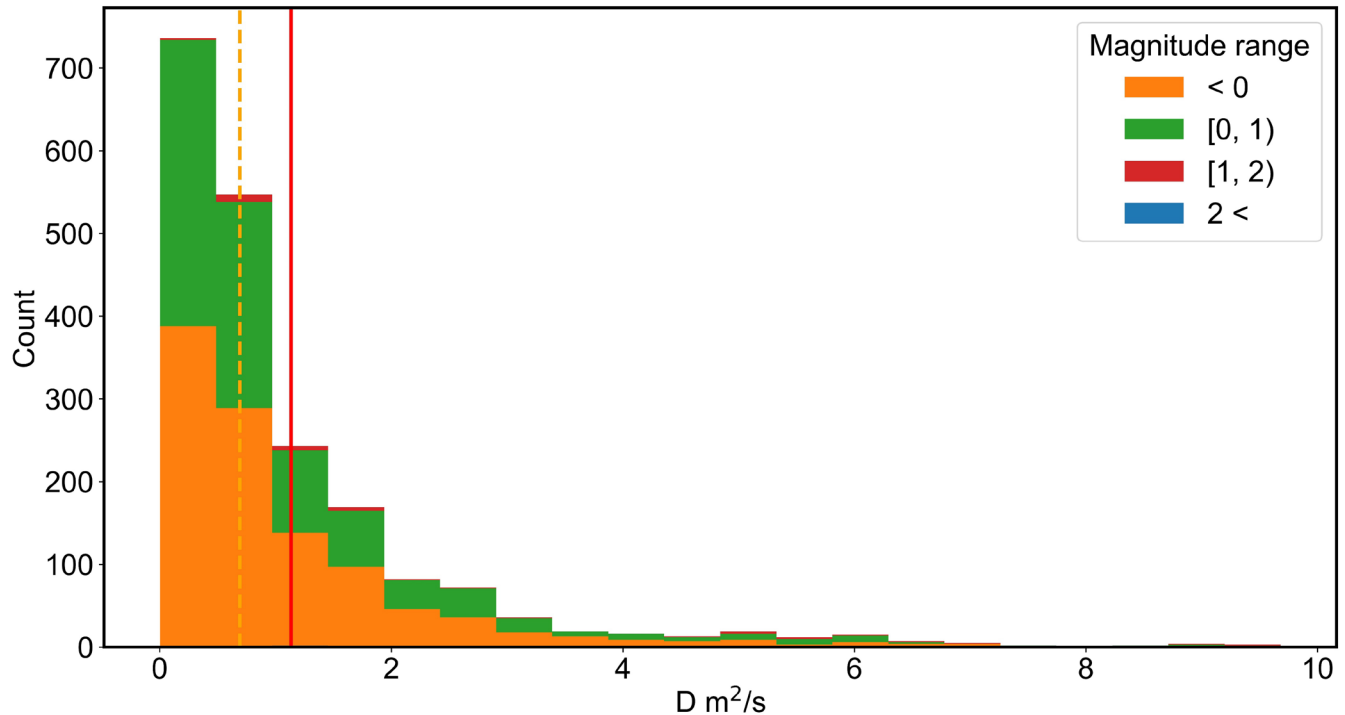


Figure 43: The distribution of hydraulic diffusivity colored by their magnitude ranges for OP1. The solid red and dashed orange vertical lines illustrate the mean ($1.14 \text{ m}^2/\text{s}$) and median ($0.7 \text{ m}^2/\text{s}$) values, respectively.

Hydraulic properties of the reservoir were estimated using the same assumptions made for OP3 and using the same modified cubic law procedure explained in the previous section. Figure 44 illustrates the effective hydraulic permeability and aperture of the identified structures as well as the overall distribution of these parameters. As can be seen, the median permeability and aperture of the structures associated with OP1 are very similar to those for OP3 at around 10^4 mD and 10^{-4} m . Since the aperture and hydraulic diffusivity are proportional (i.e., $D \propto a_h^{2.5}$, assuming a constant aperture and fracture porosity), some of the larger structures which are only connected to a small number of fractures typically show larger diffusivity, and equivalently, permeability and aperture (Figure 45). These structures were typically associated with the larger events during the fluid injection.

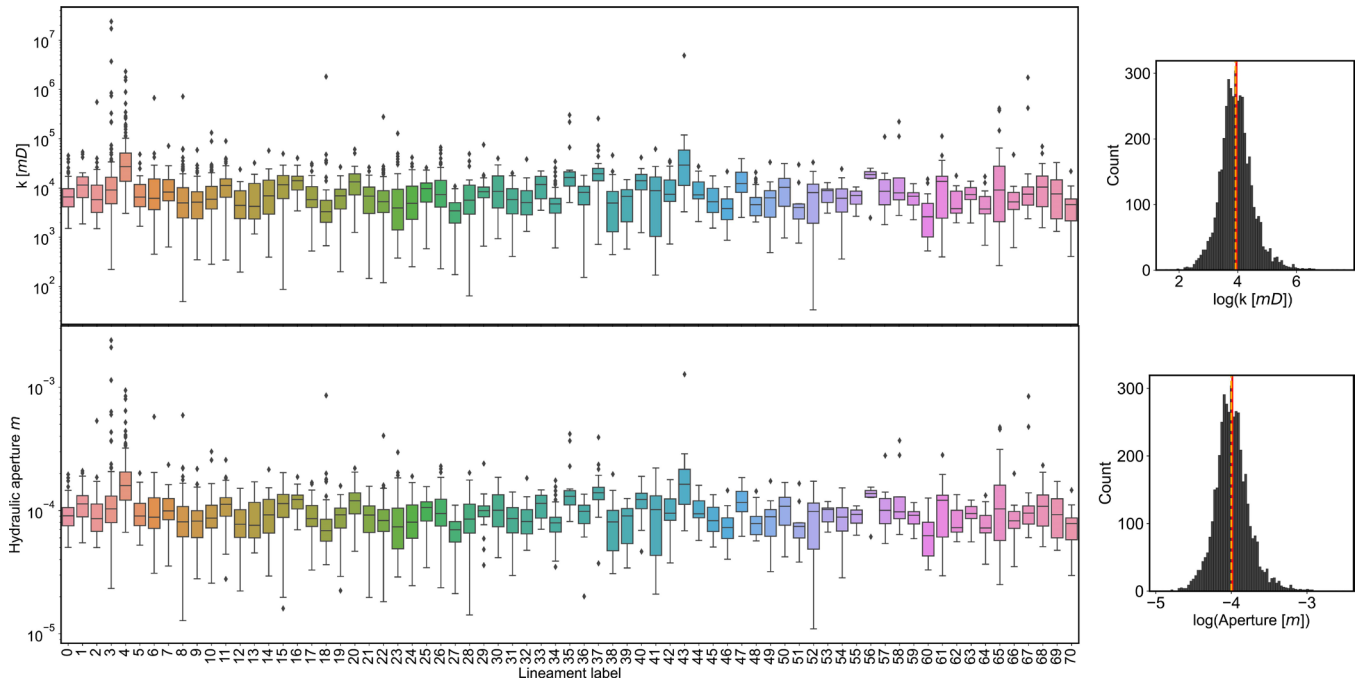


Figure 44: Plot of the effective hydraulic permeability and aperture calculated for all structures activated during the fluid injection for OP1. The box plots show the properties for each structure, and the overall distributions of the properties are shown to the right, where the solid-red and dashed-orange vertical lines indicate the mean and median values, respectively.

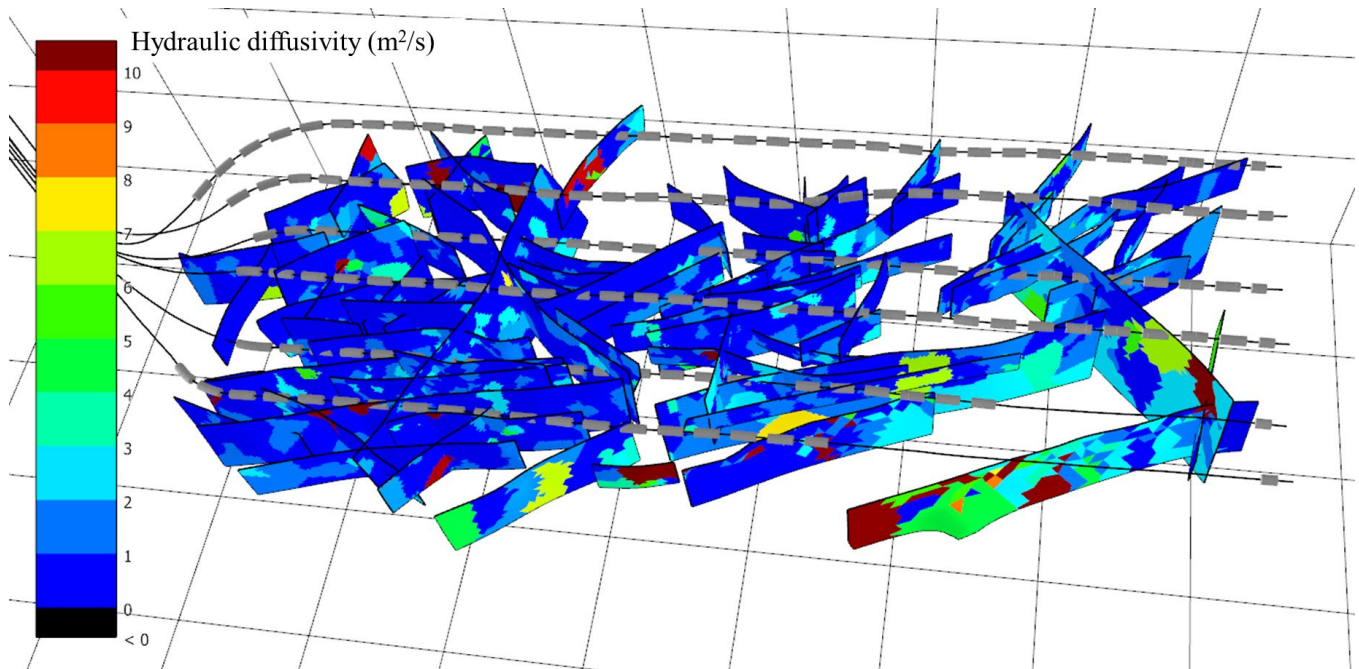


Figure 45: Hydraulic diffusivity values calculated for each event superimposed on the identified activated structures for OP1. Wells D to I are from top to bottom, and the hydraulic stages are shown as grey cylinders.

Limited injection data were available for OP1, and therefore the average injection pressure and the average injection rate was used to calculate I_{eff} . To do this for each stage, we calculated the cumulative seismic moment and the time difference between the occurrence of each seismic event after the start of the injection. Using this time difference and the average injection pressure and rate for the stage, we calculated the hydraulic energy using Eq. (5). Finally, the ratio of cumulative radiated energy of seismic events that occurred in the specified time period and the hydraulic energy E_H was calculated as I_{eff} . Figure 46 presents I_{eff} for each well and each stage as a function of elapsed time since the beginning of the fluid injection. Since the time varies from stage to stage, we do not show the quantity on the horizontal axes. As can be seen in these plots, the seismic energy efficiency ranges from 10^{-4} to 10^{-3} , which is 1 to 2 orders of magnitude larger than those reported for typical hydraulic fracturing completions (i.e., $I_{eff} < 10^{-5}$; see Maxwell et al., 2008; Maxwell, 2011; Goodfellow et al., 2015; Kwiatek et al., 2018). However, these values are well within the values reported for hydro-shearing on pre-existing structures in enhanced geothermal systems (see Kwiatek et al., 2019), and therefore similar to OP3, the results support the hypothesis of slip/activation of natural fractures and structures in this case, particularly for the early completion stages (i.e., close to the toe of the wells). Note that with the available injection operation data for OP1, it was not possible to plot the cumulative radiated seismic energy as a function of cumulative input hydraulic energy.

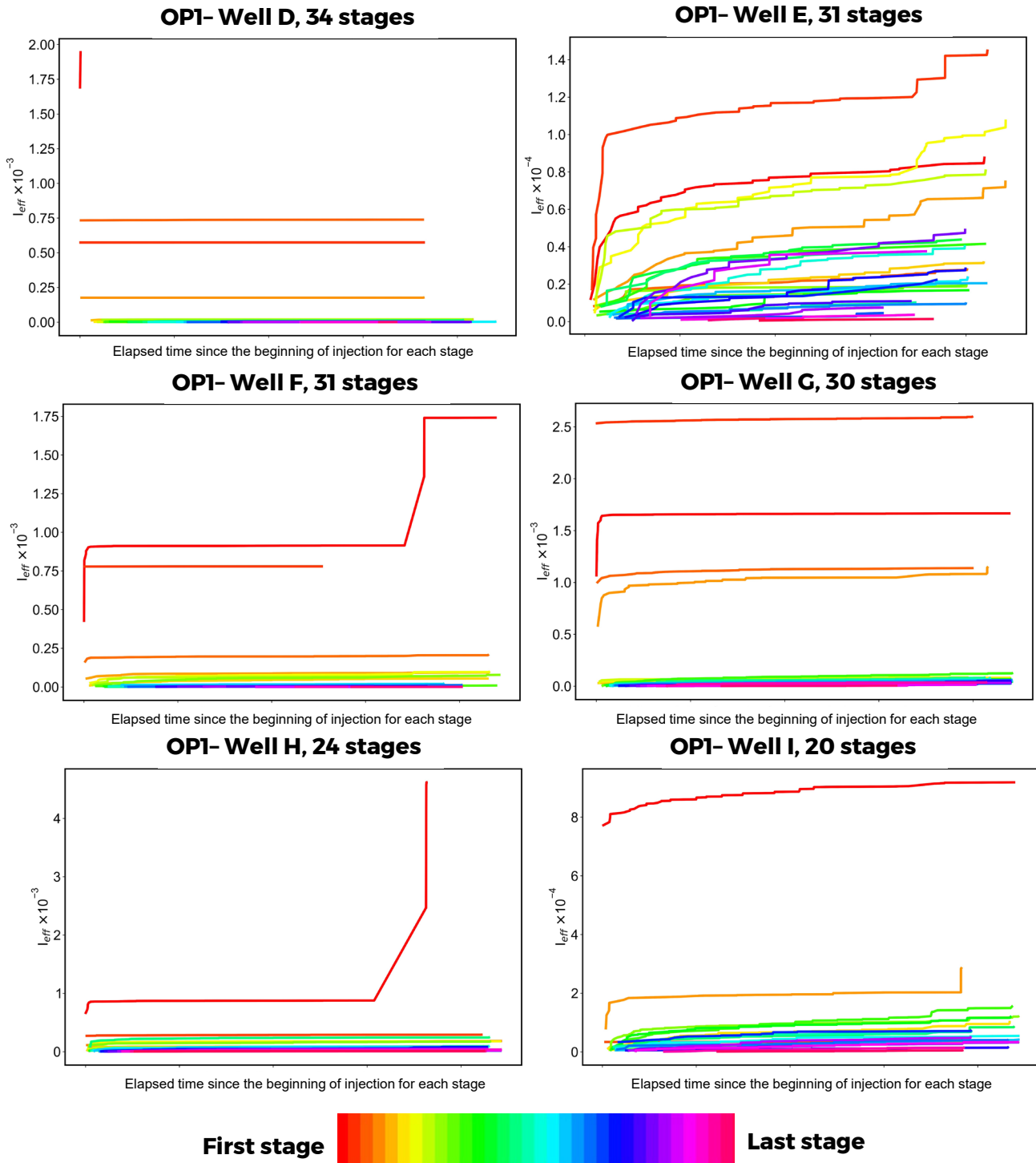


Figure 46: Seismic energy efficiency calculated for OP1 over the full hydraulic stimulation. Shown is the hydraulic seismic injection efficiency, I_{eff} , as a function of lapsed time since the start of injection.

4.4 Synthesis

Comparing the results for both well pads (OP3 and OP1), the hydraulic diffusivity distributions (Figure 37 and Figure 43) and transport properties (Figure 39 and Figure 44) show larger values for OP3 than OP1. One explanation for this is that OP3 was completed using an open hole completion technique. This would increase the possibility that the same fracture network gets stimulated repeatedly during injection from the neighboring stages. The elevated fluid pressure in the fracture network would adversely contribute to the pressure transition required to overcome the fault shear strength, and thus the delay time from the start of injection to the seismic event would decrease. This would result in a higher calculated hydraulic diffusivity (recall, $D \propto 1/t$). The presence of such elevated fluid pressures in the system might increase the average hydraulic aperture of the fracture network and consequently the permeability.

It was further found that the hydraulic diffusivity values recorded for both pads (especially OP3) are considerably higher than those typically reported for hydraulic fracturing operations (e.g., Hummel and Shapiro 2013) and hydro-shearing stimulations of enhanced geothermal systems (e.g., Shapiro et al., 2002, Talwani et al. (2007)). Moreover, the induced seismicity events from some stages in both datasets do not follow the typical parabolic signature in r - t space. We believe this is related to the number of connected structures to the pressure perturbation source and discuss this in more detail in the paragraphs below. This was further confirmed by comparing the seismic energy release calculated for the two pads (10^{-4} to 10^{-3}), to typical values of $I_{eff} < 10^{-5}$ reported for other hydraulic fracturing operations (e.g., Maxwell et al., 2008; Goodfellow et al., 2015). Together, these suggest that structures in the Kiskatinaw area of the Montney formation, especially the Lower Montney, may be highly connected and a larger proportion of the input hydraulic energy is activating the structures.

The unique and unusual event distributions in $r - t$ space seen for both OP3 and OP1 (Figure 36b and Figure 41a) were studied and compared with the more typical parabolic signature of event distributions associated with hydraulic fracturing operations (e.g., Figure 34c). To do so, well F of OP1 was selected where both distributions (atypical and typical) were recorded in the data (Figure 47). The seismic event distributions are identified by two boxes: a blue box that bounds the event cloud where the signature of $r - t$ plot is parabolic (typical), and a red box that encompasses the part of the reservoir where the signature is non-parabolic (atypical). The adjacent illustrations in this figure represent the injection of the same fluid volume into two different reservoir types. The first applies to a highly fractured reservoir (blue box) where the intersected fracture network distributes the injected fluid volume evenly, radiating outwards following a spherical shape. The result is the typical parabolic pattern of the seismicity cloud, such as those reported for Horn River (Hummel and Shapiro, 2013). In this case the pressure front is traveling a distance r_1 close to the injection source. In contrast, the second reservoir type involves a low fracture intensity and the injected fluid flows dominantly through a small number of persistent fractures, resulting in a more elongated ellipsoid. In this case the pressure front travels a longer distance from the injection source, r_2 . Consequently, since $D \propto r^2$, the hydraulic diffusivity values for structures in the red box are most likely larger than the ones in the blue box.

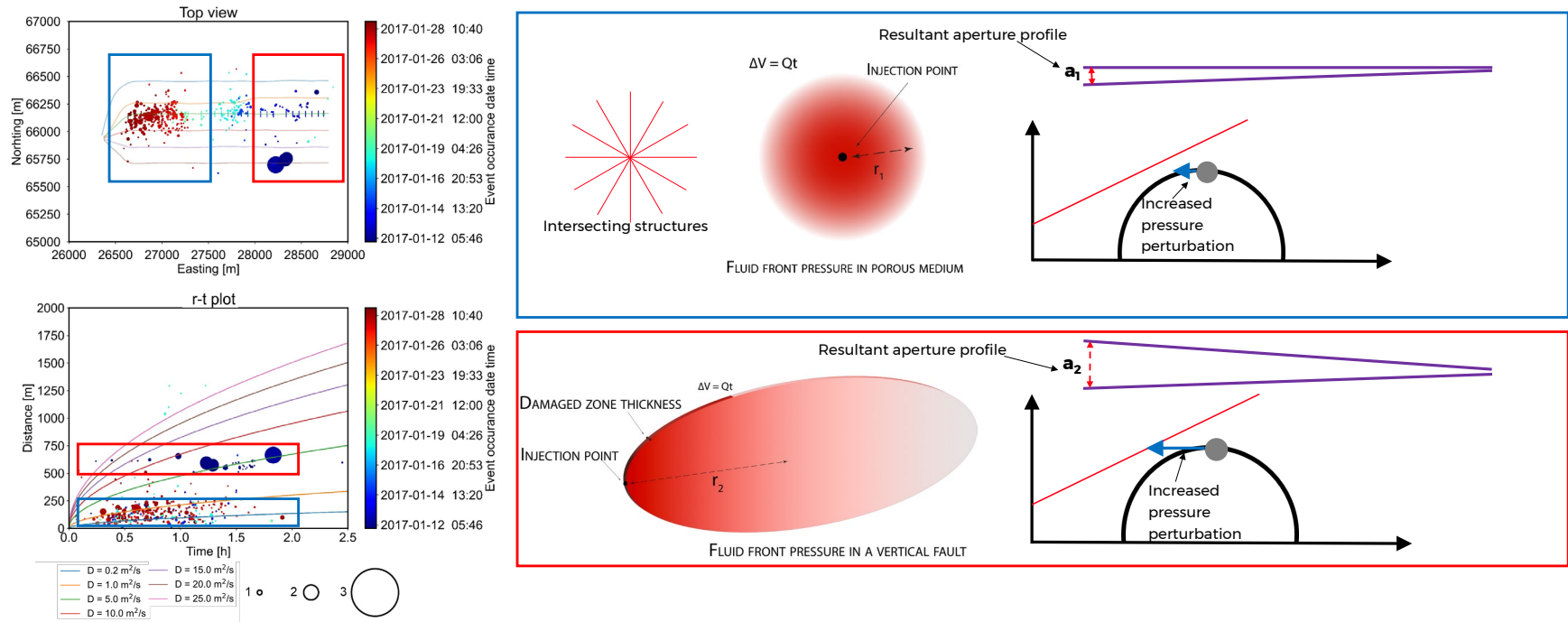


Figure 47: Seismic event distributions in r-t space for well F of OP1. Both parabolic and non parabolic signatures are shown by the blue and red boxes, respectively. The adjacent illustrations show the pressure perturbation front from the injection point. The red intensity represents the pressure distribution from highest (red) to lowest (white). For both reservoir geometries the injected volume is the same but the pressure front distance, r_2 , is larger for the case where fluid flow is confined to a single structure orientation as opposed to the case with high fracture intensity, where the intersecting structures distribute pressure more radially, with distance r_1 . Also shown are the Mohr-circle representations for both injection scenarios assuming the same fault orientation and shear strength (red line), where the blue arrow shows the increased pressure perturbation due to fluid injection. The profile of the aperture, a , due to injection into the fracture transmitting fluid pressure and volume is shown in purple. The aperture of the fracture highly intersected with other fractures, a_1 , and the aperture of the same fracture not intersecting other structures, a_2 , are relative (i.e., $a_2 > a_1$) but exaugurated for illustration purposes.

In addition, we can compare these two reservoirs from the fluid pressure distribution perspective. Considering that the same amount of fluid is injected into both systems, the larger permeable volume of the higher intensity fractured reservoir rock (blue box) contributes to lower pressure buildup in the system. Since there is a larger number of asperities with a range of different shear strength for this highly fractured and intersected system of fractures, the occurrence of a cloud of growing seismicity away from the injection source is highly plausible. This follows the conventional fluid pressure front propagation reported by other researchers (e.g., Shapiro et al., 1997, 1999, 2002; Talwani et al., 2007). On the other hand, the injection into a system where fluid flows through a small number of sub-parallel fractures that are only partially connected (red box), involves a pressure build up that favours mode-I opening of the fracture(s). Such tensile opening of the fracture network, especially near the injection source, reduces the likelihood of shear events in this area. This is shown schematically in Figure 47, where one could compare the fracture aperture, a_2 , profile along its length relative to a_1 (note that the two fractures have the same orientation and length). The resultant pressure gradient in the structure travels away from the injection source and once adequate pressure builds up along the flow channel to overcome the shear strength of the structure, shear slip occurs and the seismic energy is released. We can also compare the impact of these two pressure-buildup scenarios using Mohr circles. The blue arrows in Figure 47 show the pressure buildup in both reservoir scenarios due to injection of the same fluid volume. Accordingly, in this conceptual model, the restricted potential for leak-off in the single/parallel structure case would result in a more intense fluid pressure front and the potential for larger induced seismicity events.

We substantiate the conceptual model and hypothesis explained above (Figure 47) by first comparing the average injection pressure for each stage of OP1, and instead of looking only at one well, we carried out the analysis on the full dataset. Figure 48a shows the distribution of all induced seismic events associated with the fluid injection for OP1, including the average pressure associated with each event, the corresponding stage and the seismic event magnitude. Based on the data distribution, the top view of the reservoir can be divided into two areas (dashed grey line) where the average injection pressure is higher than 60 MPa (the east side) and lower than 60 MPa (the west side). Comparing this graph with the identified geological structures (e.g., Figure 45), these represent the low (east) and high (west) fracture intensity reservoirs, respectively. Figure 48b illustrates the corresponding average injection rate, which seems to be equal or slightly larger for the west side of the reservoir and given that the duration for injection of each stage is about the same (1 hour), this supports the assumption in the conceptual model of the same amount of fluid injection. In other words, observing a larger injection pressure for the east side where the reservoir has a lower fracture intensity agrees with the conceptual model proposed.

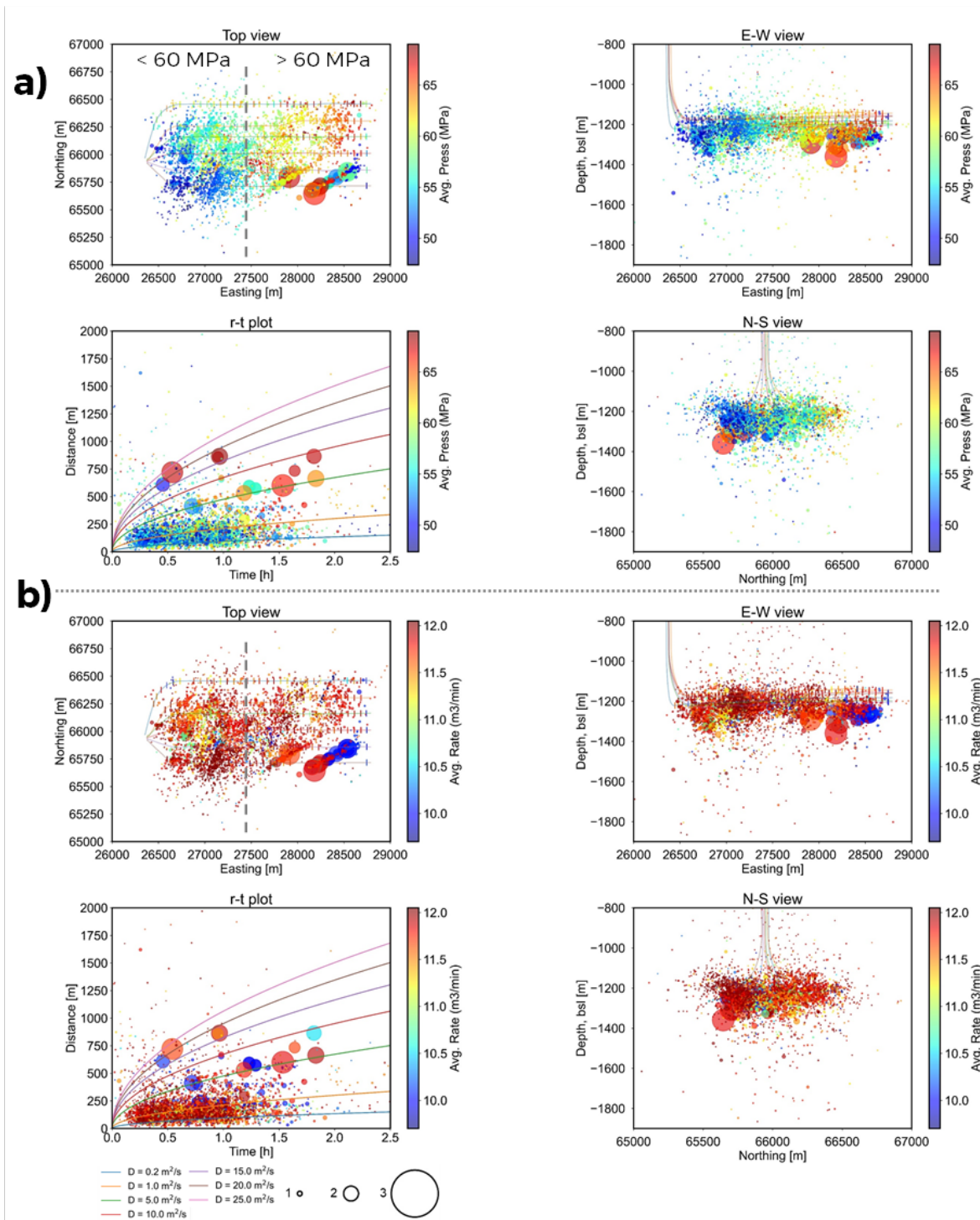


Figure 48: a) View of all induced seismicity data for well F of OP1 with the corresponding r-t plot. Events are coloured by the average injection pressure, and the size of each point shows the seismic event magnitude, as denoted in their respective legends. In the top view plot, the east and west of the reservoir is separated by a dashed grey line, which approximately separates areas where the injection pressures are larger than 60 MPa (East) and lower than 60 MPa (West). b) The same as plots as in a) except the events are coloured by the average injection rate (m³/min).

Using the data, we next examined the conceptual-model hypothesis that the larger hydraulic diffusivity and seismic event magnitudes are associated with injection into a low fracture intensity region of the reservoir. Figure 49 shows the relationship between the hydraulic diffusivity as a function of the number of connected structures to the hydraulic fracturing stage. The data suggest an inverse relationship between the hydraulic diffusivity and the number of connected structures. The circle size is proportional to event magnitude, and it can be seen that most of the larger events in this dataset (encompassing all induced seismicity events for OP1) are occurring on the structures that are connected with only a few structures (i.e., less than 6 lineaments), and that these events are mostly associated with larger average injection pressures. These observations are in agreement with the conceptual model that we developed above, which explain the mechanism of the observation of larger induced seismicity events.

In Section 6.0, the proposed conceptual model for injection into high and low fracture intensity reservoir rock is further investigated using numerical simulations based on the identified structures for OP1 to support and derive further mechanistic understanding.

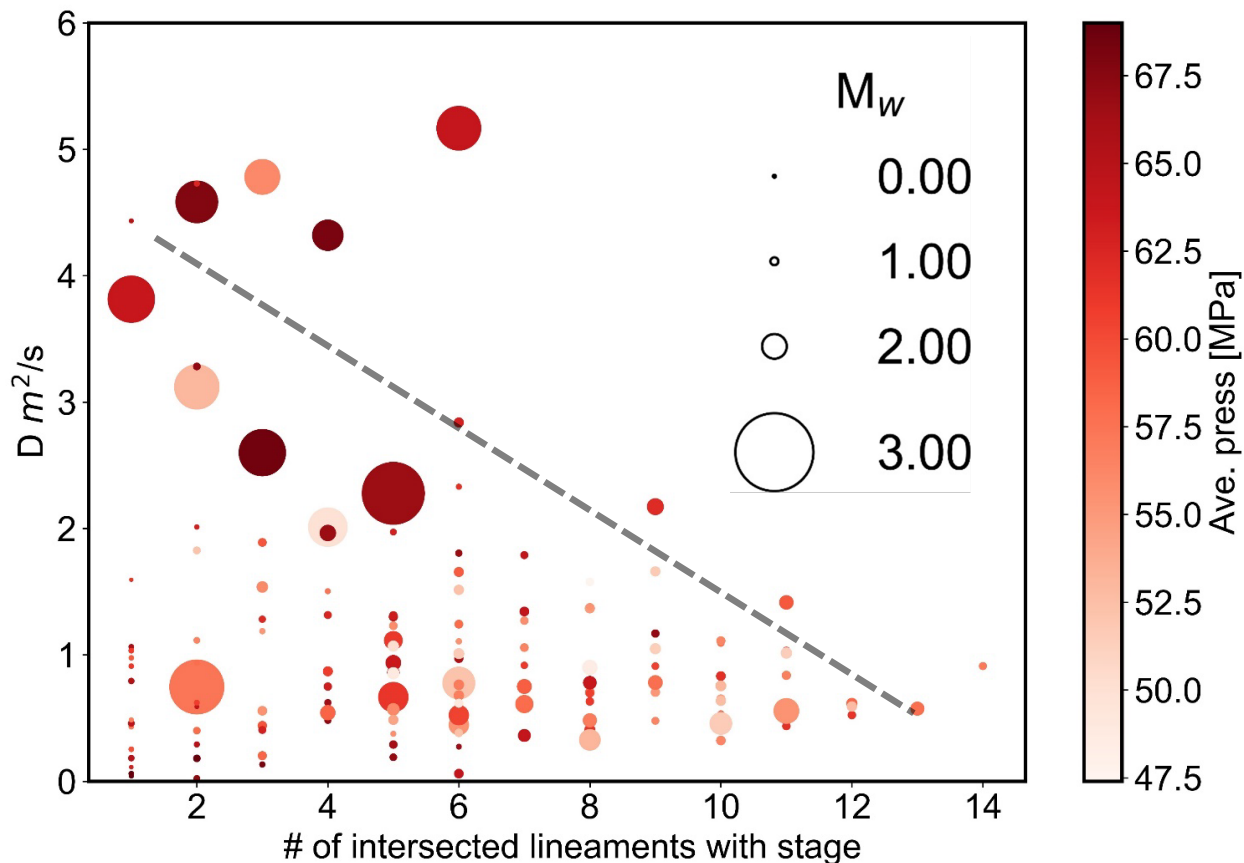


Figure 49: Relationship between hydraulic diffusivity, the connectivity of the structures with each corresponding stage, seismic event magnitude and the average injection pressure for OP1. The grey line shows the inverse relationship between hydraulic diffusivity and the number of connected structures with the hydraulic fracture.

5.0 NUMERICAL SIMULATION OF HYDRAULIC FRACTURING AND INDUCED EVENTS

5.1 Introduction

Idealized hydraulic fracture propagation within a homogenous continuum occurs in simple tension, parallel to the direction of maximum horizontal stress. However, in naturally fractured rock masses such as those present in the Montney, the propagation of hydraulic fractures can be a far more complex process as a result of their interaction with the natural fractures. Simple tensile fracture propagation occurs where the fluid pressure exceeds the sum of the minor principal stress and the tensile strength of the material.

Assuming a known horizontal extent of a hydraulic fracture (e.g., vertically constrained within confining beds) the horizontal extent of hydraulic fractures can be estimated based on a mass balance principle. That is the total volume of injected frac-fluid (V_i) must match the volume of the opened hydraulic fracture (V_f), plus the volume (V_L) of leak-off to the natural fracture network (and to the rock matrix, in the case of permeable rock). As an alternative to complex and time-consuming numerical simulations of hydraulic fracture growth and interaction, the FracMan Discrete Fracture Network (DFN) based approach has been applied to model and predict hydraulic fracture development, within a network of existing natural fractures, WSP 2023. FracMan uses a simplified geomechanics scheme based upon a mass balance approach above, allowing a complex definition of the natural fracture geometry to be tested, Dershowitz et al. 2010, Rogers et al. 2014.

For the purposes of this study, there are a number of critical aspects that need to be investigated:

- What is the approximate shape of the hydraulic fractures (both length and height)?
- How does the hydraulic fracture interact with interpreted other natural structures?
- Does a diffusive network of connected structures allowing pressure communication between active stages/hydraulic fractures and faults explain the observed patterns of seismicity?

Table 5: Summary of Key Inputs for FracMan Hydraulic Fracture Simulations

Data Class	Key Properties	Constrained by
Well & Stage Geometry	<ul style="list-style-type: none"> ■ Well geometry ■ Stage locations & perf locations where appropriate 	<ul style="list-style-type: none"> ■ Engineering data, measurements ■ Engineering data, measurements
Injection scheme	<ul style="list-style-type: none"> ■ Rates, durations, pressures etc. 	<ul style="list-style-type: none"> ■ Recorded during treatments
Mechanical Earth Model	<ul style="list-style-type: none"> ■ 3D grid of stresses (S1, S2 and S3(magnitudes and directions)) ■ Layer cake elastic stratigraphy or Static Young's Modulus and Poisson Ratio 	<ul style="list-style-type: none"> ■ Interpreted from DFIT data and calculated using Eaton Equation ■ Derived from elastic logs and converted from dynamic to static properties
Natural Structures	<ul style="list-style-type: none"> ■ Deterministic structures ■ Stochastic structures 	<ul style="list-style-type: none"> ■ Derived from the interpretation of induced events/seismic data ■ Interpreted from observed data and inferred at a scale below the deterministic structures

The purpose of the FracMan simulations is to investigate key controls on the frac geometry, fracture interaction and induced seismicity. Validation of the hydraulic fracture propagation and interaction typically comes from the reproduction of observed seismic events during stimulation because of shear reactivation during hydraulic fracturing.

5.2 Hydraulic fracture Simulations – OP1

5.2.1 Model Set Up

A FracMan model was developed around the pad in question for Operator 1 using the key inputs listed in Table 5:

- The wells, stages, and perfs were set up along with the treatment schedule
- A modelling grid of dimensions 3,500 m x 2,000 m x 250 m around the six well pad was constructed, Figure 50. This grid was populated with stress properties based upon the Eaton equation (Eaton 1969), using static elastic properties and a regionally derived strain calibration, Figure 51.

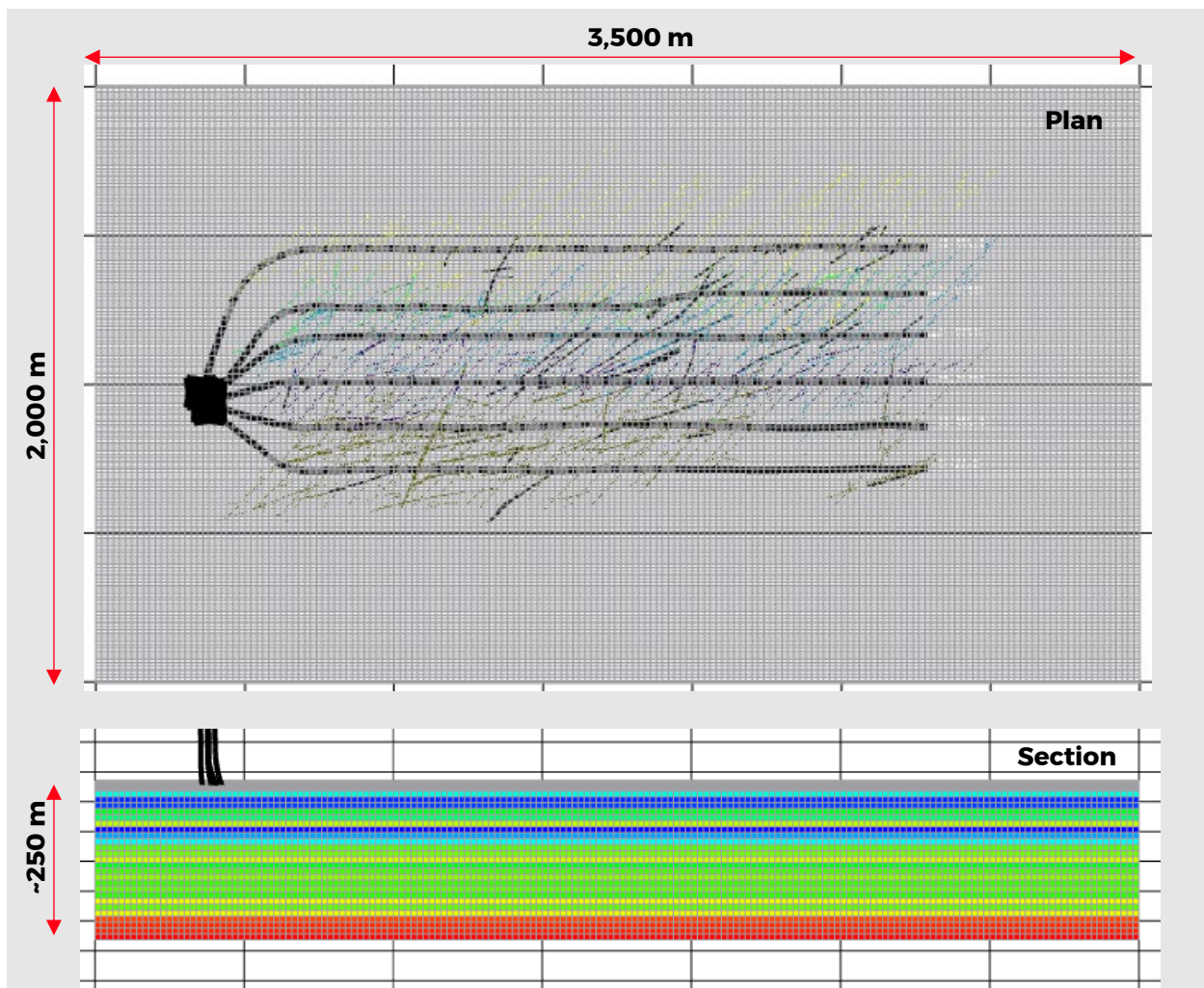


Figure 50: Plan and section view of OP1 grid with stress properties.

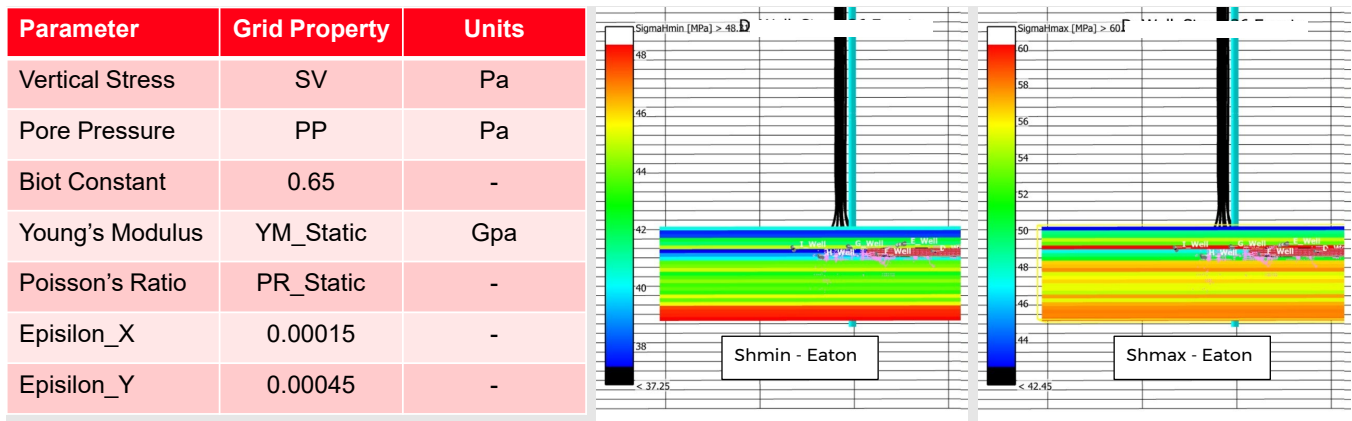


Figure 51: Scale of modelling grid and population of stress properties using the Eaton equation.

The location of the six wells is shown more clearly in Figure 52 with the SHmin property displayed along with the Montney unit boundaries. This does show that the Upper Montney unit can be broadly divided into a lower low stress zone, where the lower bank of wells are developed and an upper higher stress zone, where the upper bank of wells are developed.

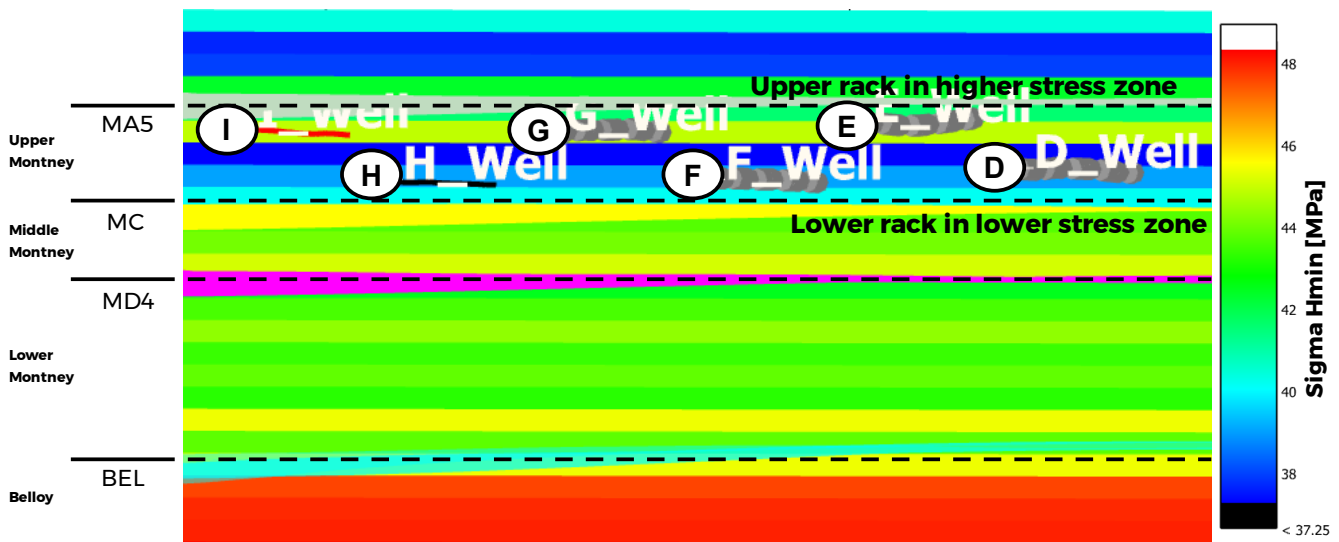


Figure 52: View of the upper and lower bank of wells within the Upper Montney, displayed against the SHmin property showing the variable stress in the Upper Montney.

Injection from the six wells is sequential from well D to I, with the stresses updated every stage. FracMan tracks the size and shape of the hydraulic fracture, identifies any natural structures that may be inflated during injection (i.e., take fluid) as well as identifying which structures may be stimulated through a hydro shearing process. Hydro-shearing occurs when the pore pressure increases as a result of nearby stimulation results in the drop of effective normal stresses on a fault/fracture, resulting in shear failure, slip and the generation of seismicity. The results of the simulations are described below.

5.2.2 Modelling Results

The focus of the hydraulic fracture simulations is to understand the general patterns of frac generation and shape and their interactions with natural structures. The modelling is considered to be reasonably accurate, but it is not possible to calibrate the properties for every well. Proppant has been included in the simulation but has not been considered in the results.

The key findings of the simulations are as follows:

5.2.2.1 Frac Shape

A key observation from the modelling is the different frac shape developed by the wells, depending upon whether the stimulation is the upper rack of wells (wells E, G, I) or in the lower rack (wells D, F, H), Figure 53. Note how the lower wells appear to be producing long skinny fracs within a well-defined layer whereas the upper rack of wells appears to produce more elliptical frac shapes, with no clear containment of the fracs. This appears to be associated with the difference in stresses and stiffnesses observed in the upper Montney. As can be seen in Figure 52, the lower wells are contained within a lower stress/lower stiffness zone which means that as the frac propagates, it remains contained in the same zone by the overlying and underlying higher stiffness/stress layers. This results in ribbon shaped fracs approximately 50 m high (defined from the low stress layer) and extending approximately 500 m away from the well in an NE-SW direction. In contrast, wells drilled in the higher stress layer of the upper Montney are prone to propagate out of zone, notably going downwards as well as upwards, with a more radial frac shape.

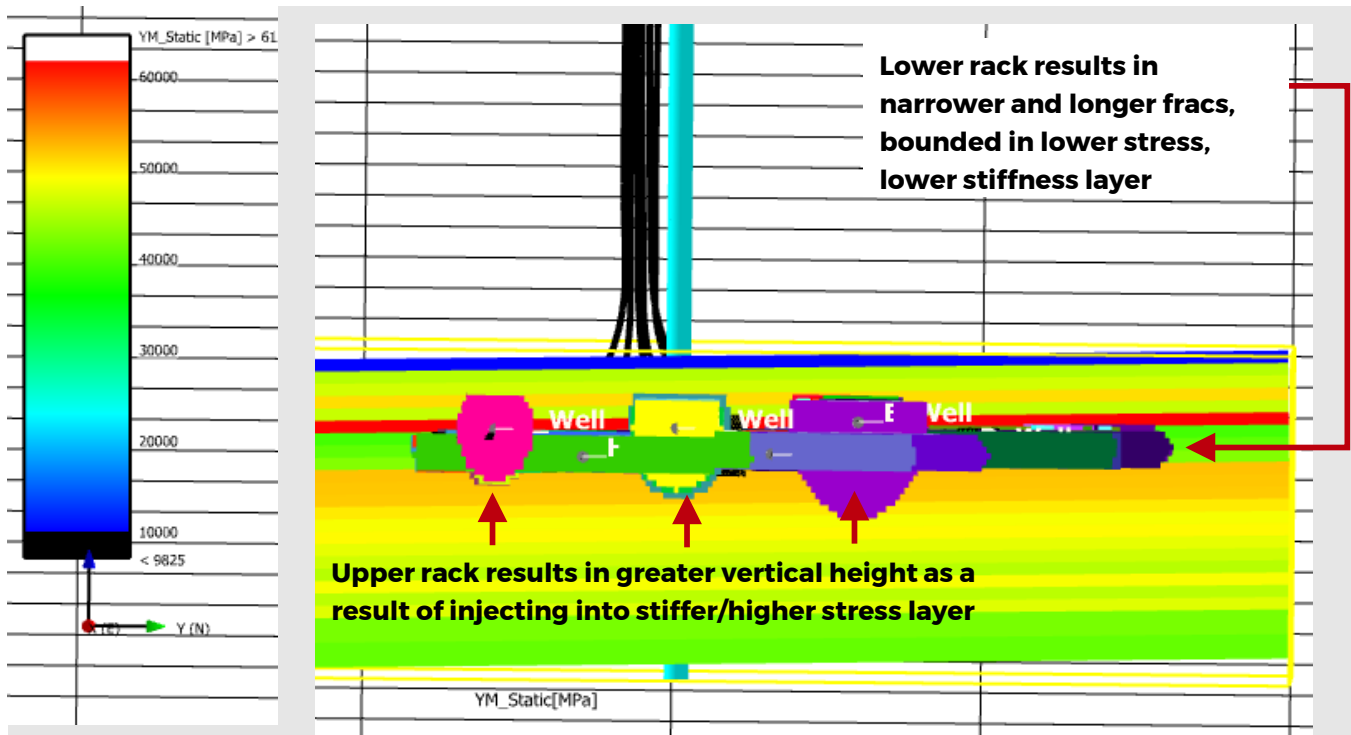


Figure 53: Wellbore axial view of hydraulic fracture shape showing the long skinny fracs forming in the lower stiffness layer from the lower bench of wells and the more radial fracs forming from the upper bench stimulation into the higher stiffness layer. Coloured property shows static Young's Modulus.

One way to validate these observations is to look at the distribution of induced events relative to which the wells triggered them. Figure 54 shows a cross sectional view from the south, with events coloured by their triggering well and differentiated into upper and lower wells. The figure shows how the seismicity is primarily downwards with the G and I well both being associated with considerable seismicity. A histogram of event frequency shows that there are more than twice as many events associated with the upper wells than lower wells, Figure 54. This is consistent with the observations shown in Figure 53 with the upper bench wells driving fracs deeper.

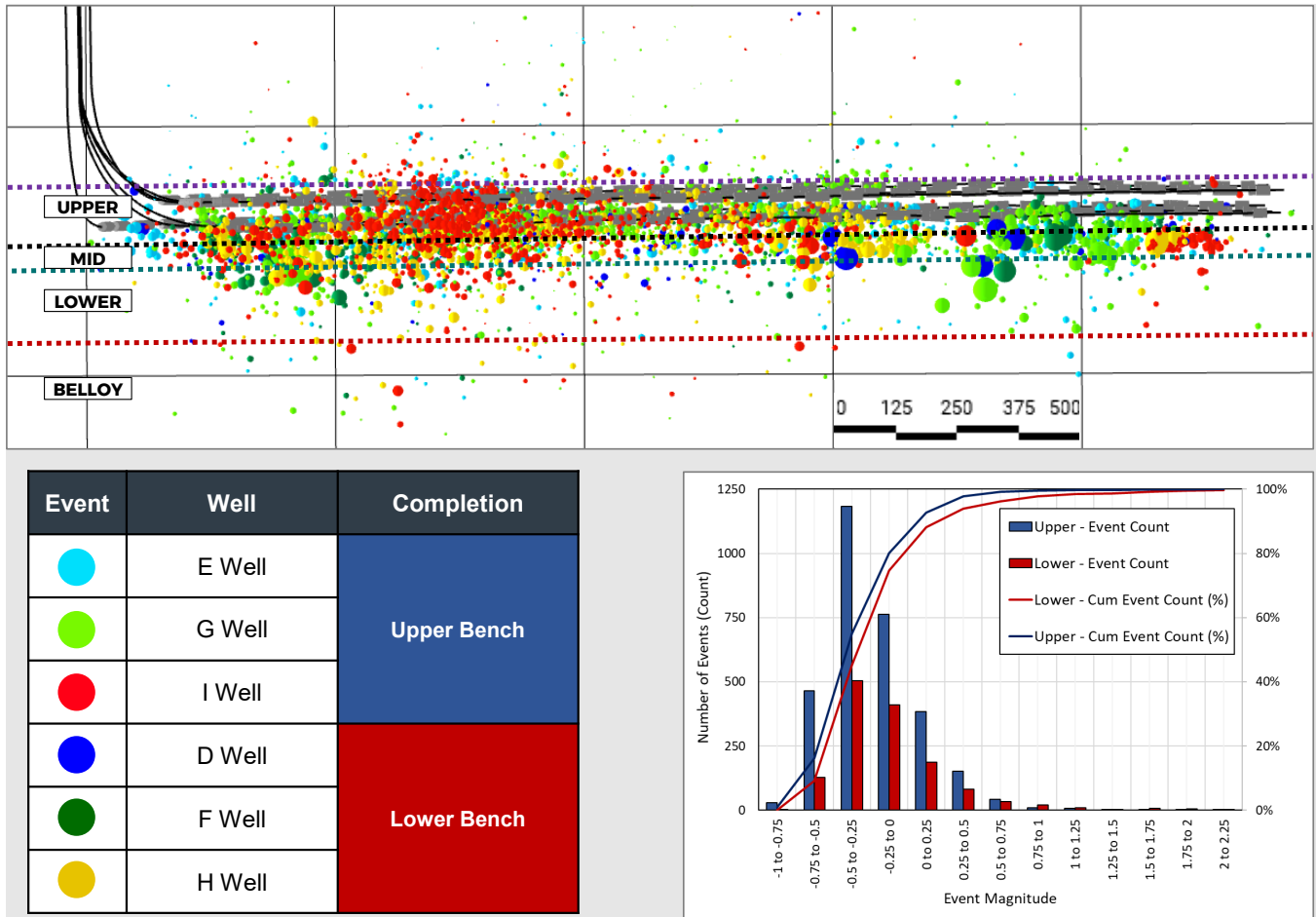


Figure 54: Cross sectional view from the south, with events coloured by their triggering well and differentiated into upper and lower wells. Histogram of event frequency also differentiated into upper and lower wells.

5.2.2.2 *Frac Length*

The length of the longer bounded fracs from the lower wells was modelled at approximately 500 m long, Figure 55. This length can easily be adjusted by increasing or decreasing the net pressure to shorten or lengthen the frac. As such, we don't consider this as a calibrated property.

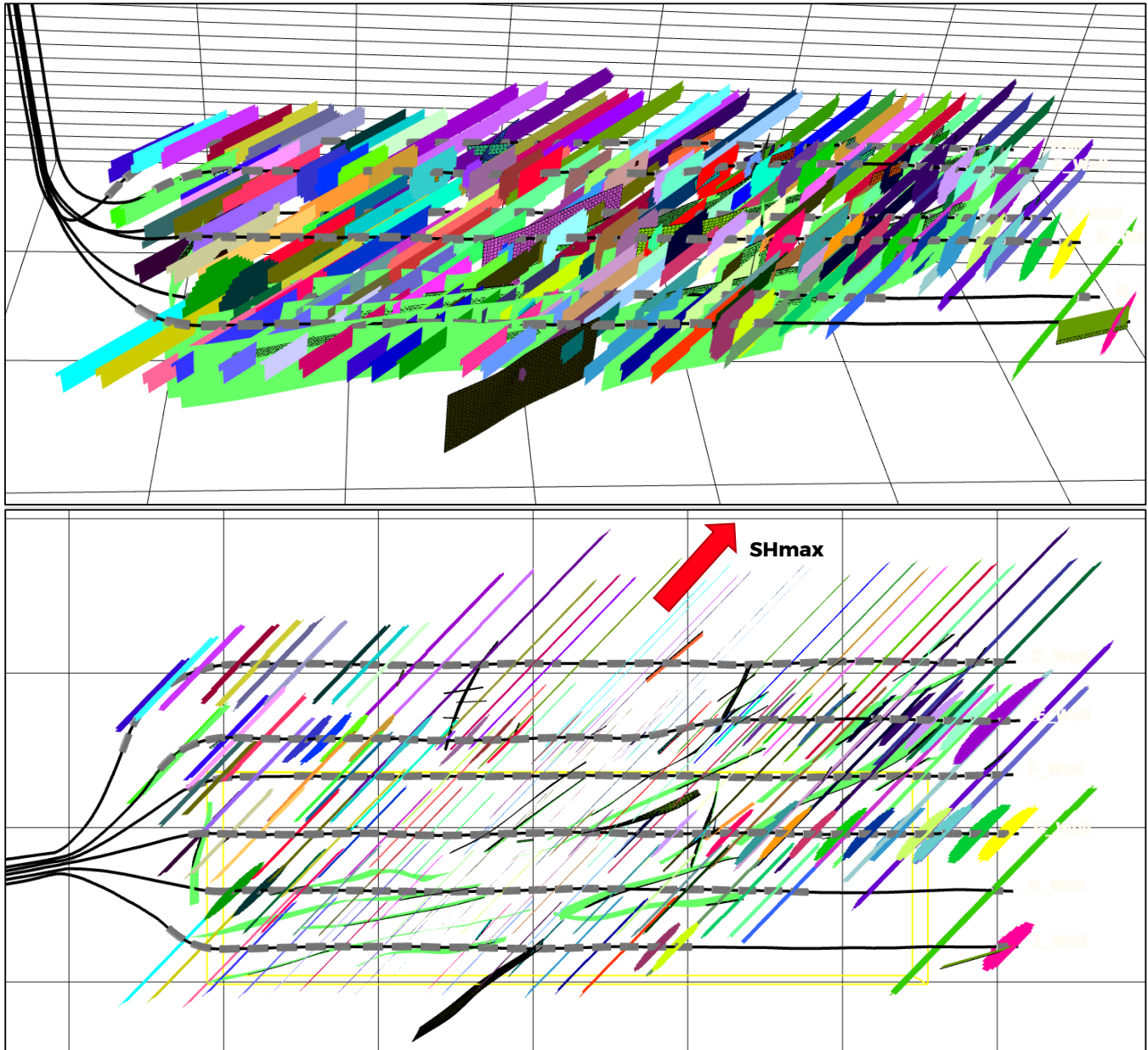


Figure 55: View of the FracMan hydraulic simulation results. Upper view oblique view from the south and Lower view, plan view. The direction of SHmax is shown on the lower image, with the aligned fractures being the induced hydraulic fractures. The other fractures are inflated natural structures and are discussed below.

5.2.2.3 Interaction with existing structures

Injection of pressurised fluid into the well will initiate a hydraulic fracture that propagates away from the well. If this frac intersects natural structures such as faults or fractures and the frac pore pressure is greater than the closing stresses on the structures, they can dilate and receive fluid and potentially proppant. This can be shown on Figure 56 (Modified from Figure 16). The zone indicated by No. 4 on the figure represents the zone on the Mohr circle where natural structures would inflate as the injected pore pressure is greater than the normal stresses experienced by the structures. These fractures would be orientated approximately $\pm 25^\circ$ to SHmax.

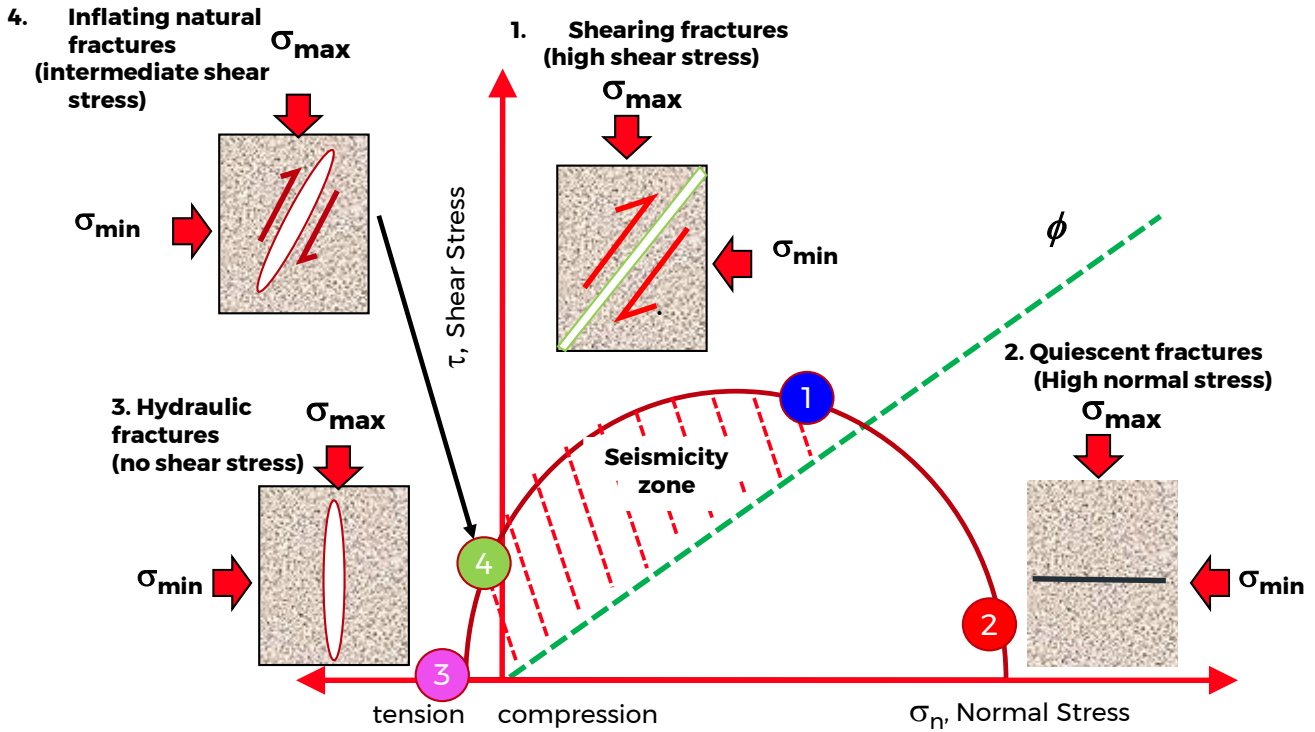


Figure 56: Basic geomechanics of injection (modified from Figure 16) to include inflated natural structures (No 4).

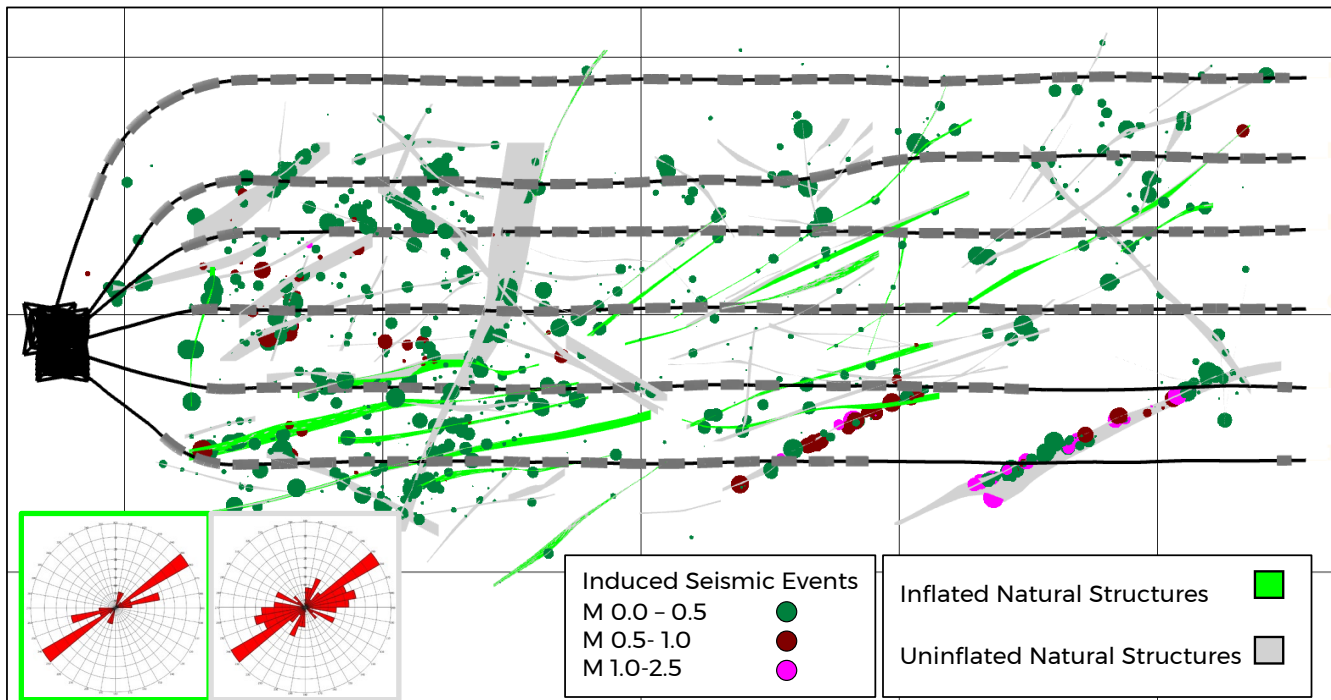


Figure 57: Plan view showing those natural structures that were inflated during stimulation (green) and the total population of interpreted structures (grey). The rose diagrams show the orientation trends for the top populations as indicated by the colour of the outline. Induced seismic events greater than $M=0$ is also shown.

The FracMan simulations track which fractures inflate and take fluid, Figure 57. The figure shows those inflating natural structures in green with the total population of interpreted structures from the induced seismic events shown in light grey. The inflated structures appear to be a sub-set of the total population being strongly SHmax -aligned. Whilst some of the uninflated natural structures are orientated unfavourably to the stress field (e.g., the NNE-SSW structure in the centre of the west part of the pad), there and also many favourably orientated structures that fail to connect to the active stage or propagating hydraulic fracture. As structures are typically not all fully through going, the probability of connection with the well is reduced and that results in the seemingly random involvement of these structures within frac development and associated induced seismicity generation.

Figure 57 also shows the larger induced seismic events ($M > 0.0-2.5$) displayed on the structures. What is clearly shown is that the larger two faults in the southeastern portion of the pad associated with the largest events are not inflated fractures and so are not taking significant fluid during stimulation. The operator deliberately skipped stages on the H and I wells in an attempted to reduce fault reactivation and so the induced events on these structures are not either from direct fluid connection.

5.2.2.4 *Hydro-shearing structures*

The Mohr circle presented in Figure 56 shows the response of a number of structure types to elevated pore pressures within the in-situ stress field. Fracture type No 1 shows fractures that are critically stressed and experience the process of hydro-shearing. That is when they receive sufficient pore pressure to exceed the shear failure criterion, they can experience slippage and the generation of seismic events. This is in contrast to hydrofracturing, where new tensile fractures are generated when the fluid pressure exceeds the minimum tensile stress s_3 and the tensile strength of the rock. Given that the large faults in the southeast of the pad didn't receive direct injection (due to skipped stages) and also a high proportion of the mapped seismic structures didn't inflate (see Figure 57), the triggering of seismic events by a diffusive pressure front moving through a connected network of structures appears to be one of few remaining options.

The FracMan simulation tracks all structures that are connected back to the active stages, identifying all parts of these structures that are critically stressed, assuming pressure diffusion from the limit of the active stimulation (hydraulic fractures and inflated fractures). Figure 58 shows the results for each individual well, compared to the observed induced seismic events for that well. There are a number of observations that can be drawn for these results:

- The simulations have represented the main distribution of induced events for each well very well
- The distribution of reactivated structures shows a variety of responses. At one end, the response is highly distributed with a low density of events across the entire pad (e.g., D well). At the other end, the response shows tight clustering around the well with much less dispersion away from it. This is suggestive that the distribution structures in the subsurface is highly heterogeneous, even locally, and that is why the seismic response of one pad is different to another
- To explain the pressure communication, structures other than critically stressed ones appear to be involved. For instance, the large NE-SW structure in the southeast corner of the pad that is activated during stimulation of the D well (the most northern), is best explained by a NW-SE structure that connects the E well to the H well. This structure would have high induced normal stresses on it, suggesting that it has preserved fracture permeability, despite its unfavourable orientation.

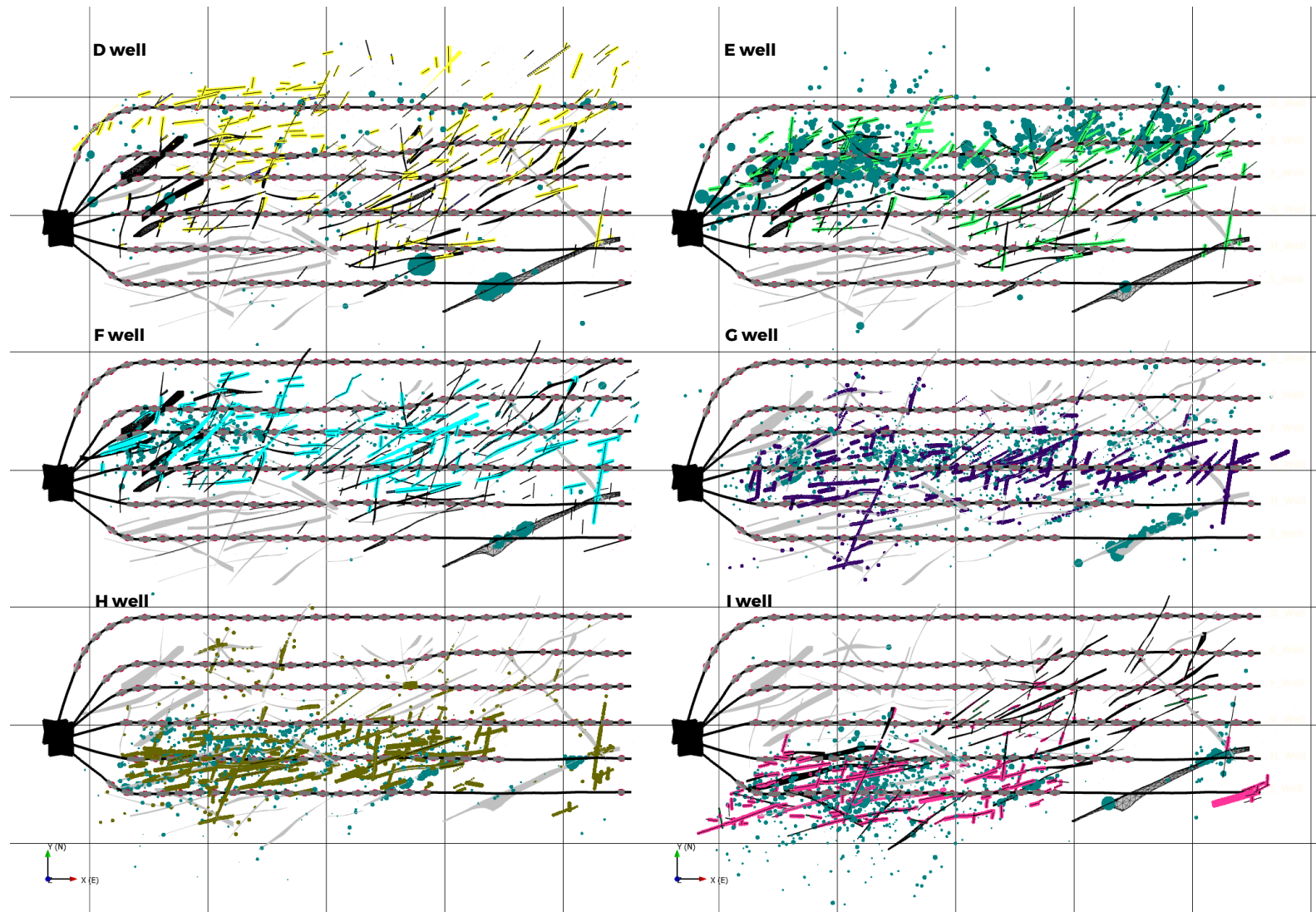


Figure 58: Hydro-shearing results for each well. The dark green dots represent the observed induced seismic events for the specific well. The light grey structures represent the total set of interpreted structure.

5.3 FracMan Simulation of Hydraulic Fracture Operations – OP3

To further test which structures participate in active stimulation during hydraulic fracturing, a FracMan model was developed around the Operator 3 pad using the same key inputs listed in Table 5. A modelling grid of dimensions 3,000 m x 3,000 m x 500 m around the 3 well Lower Montney wells was constructed, Figure 59. This grid was populated with stress properties based upon the Eaton equation (Eaton 1969), using static elastic properties and the same regionally derived strain calibration, Figure 51.

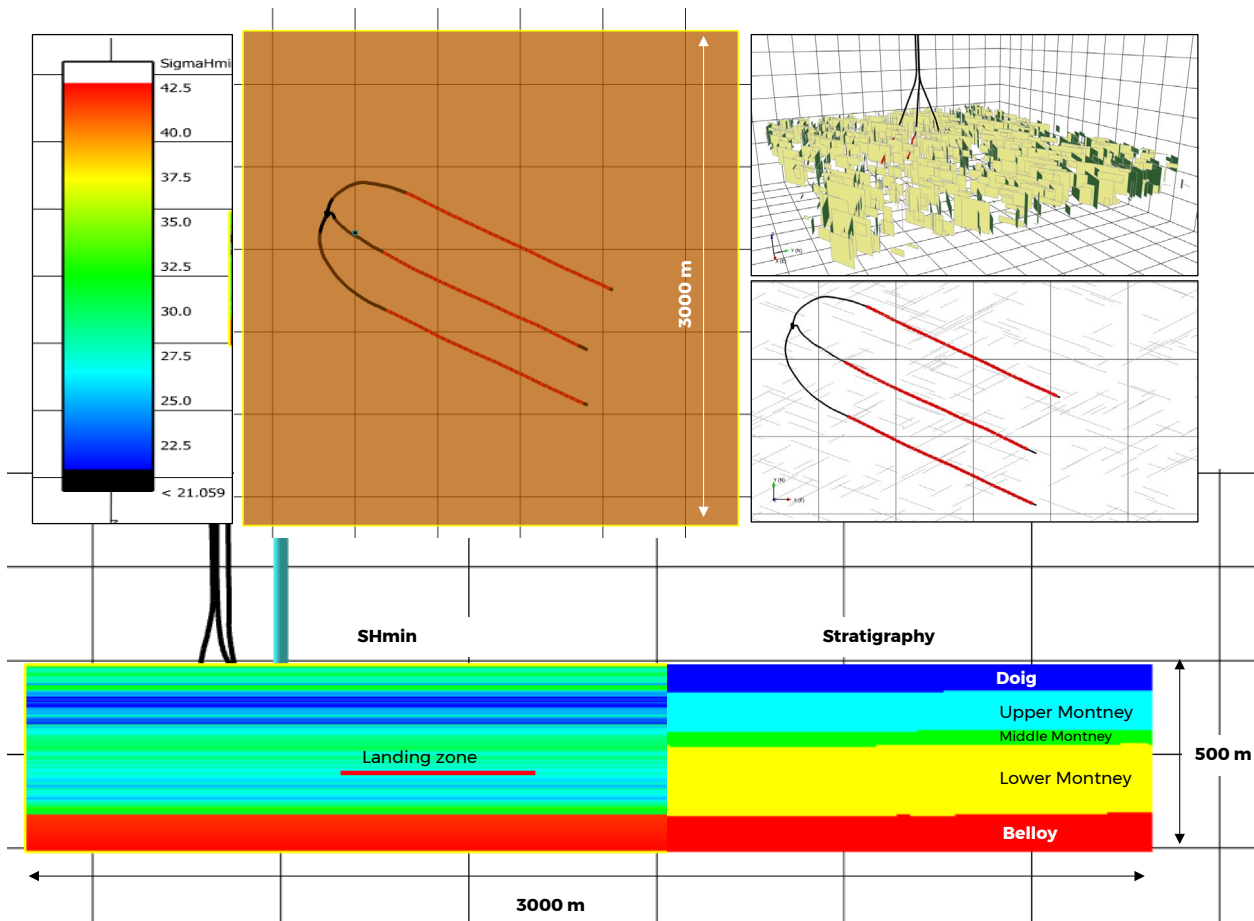


Figure 59: Plan and section view of OP3 grid with stress properties & stratigraphy. The grid displays SHmin property. Top right shows views of the Lower Montney DFN model described more fully in Section 3.2.2.

Unlike the OP1 pad with a highly interpreted fault network, the OP3 pad had a network of structures inferred and developed stochastically (Section 3.2.2). The FracMan simulation was run four times with a different stochastic fault network in each case. Injection was only carried out into the most northern well, Well_A2. The objective is to examine how these interpreted structures behave during injection in comparison to the OP1 pad. The simulations reveal the following:

- The hydraulic fractures that develop, extend out approximately 500 m on either side of the well and have a height of ~ 20 m. The presence of a lower stress layer in the Lower Montney appears to ensure the frac height remains relatively small.

- No DFN elements appeared to take fluid (i.e., inflate under injection conditions) as seen in the OP1 simulations. This suggests that the orientation of structures was such that they do not directly influence frac development.
- In contrast, hydro-shearing is seen to be a dominant mechanism, with a high number of NE-SW structures being reactivated by communicated pressure. These are seen as simulated seismic events on the structures, Figure 60. The four equi-probable examples show the modelled seismicity as well as the observed seismicity as red dots.

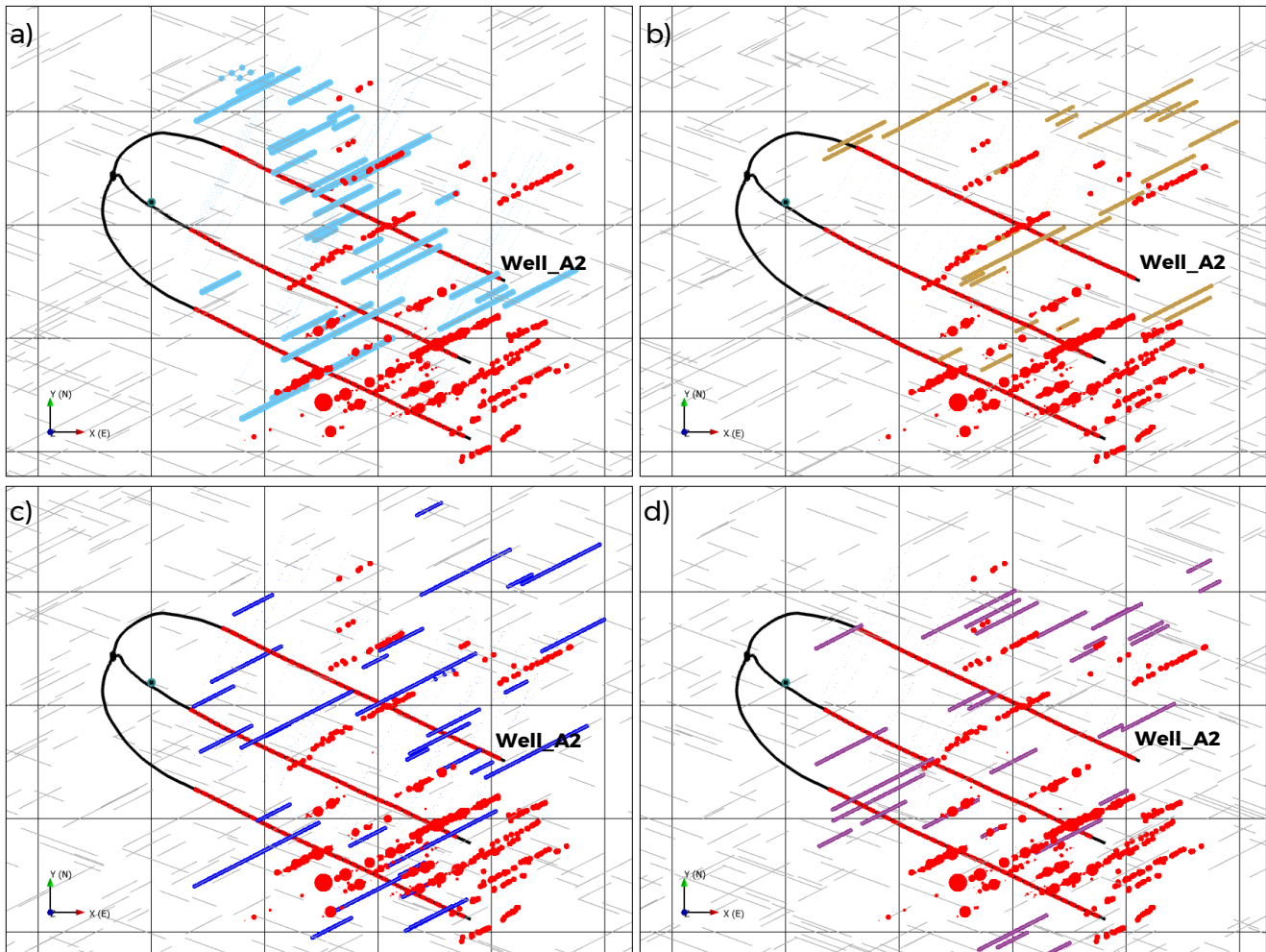


Figure 60: Simulated seismicity associated with fault reactivation for 4 realisations of the OP1 developed DFN model. Actual events are coloured in red. The smaller more regular points represent the simulated events.

There are a number of important learnings that can be drawn from these hydro-shearing observations:

- The OP3 pad shows that the simple geomechanical scheme presented in Figure 16, used for the stochastic simulations described in Section 3.2.2.
- The broad spatial distribution of events generated from a stochastic model shows good agreement with the observed seismic events. This suggests that even though the DFN model uses a simple Poisson process to generate the locations of the structures, the corresponding networks of connected structures result in a highly probable structural description of the subsurface structures.
- As was seen with the OP1 simulations, there is a need for pressure diffusion through NW-SE structures, with their relatively high normal (closing stresses). This does suggest that these structures have preserved permeability that is not necessarily dependent on orientation.
- Owing to uncertainty with regards to the vertical location of the induced events, it is not possible to conclude much about vertical connectivity of structures. However, it is entirely reasonable to conclude that vertical diffusion of pressure through large Lower Montney scale structures that may extend down in the Belloy, is a reasonable extension of these observations.

6.0 ANALYSIS TO SUPPORT EVENT MITIGATION

6.1 Stochastic simulation to Test Completion Styles

The stochastic simulations of OP3, described in Section 3.2, showed that the connectivity of large (>50 m scale) structures back to the well could explain the distribution of induced seismic events. These wells have an open hole completion, and so do encourage connection of the well to the wider network of structures. Tests were carried with this model to consider the impact of switching from an open hole system to a cased hole completion where the connectivity of the well is primarily through the hydraulic fracture and not the whole open hole interval. To achieve this, the model was switched from ~50 m open hole stages to 50 cm open hole stages to represent a perf entry completion, Figure 61.

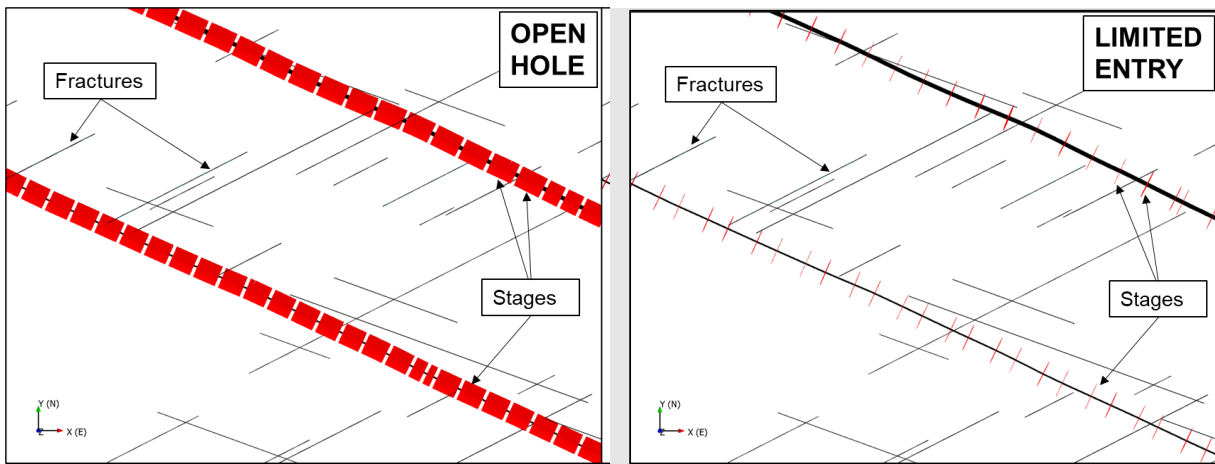


Figure 61: Comparison between left) open hole completions and right) limited entry completions.

Connectivity of the well to the wider structural network is provided by both the wellbore opening and also the hydraulic fractures. We have considered 4 different frac length cases to understand their impact on the overall connectivity in addition to completion style. The results are shown in Figure 62.

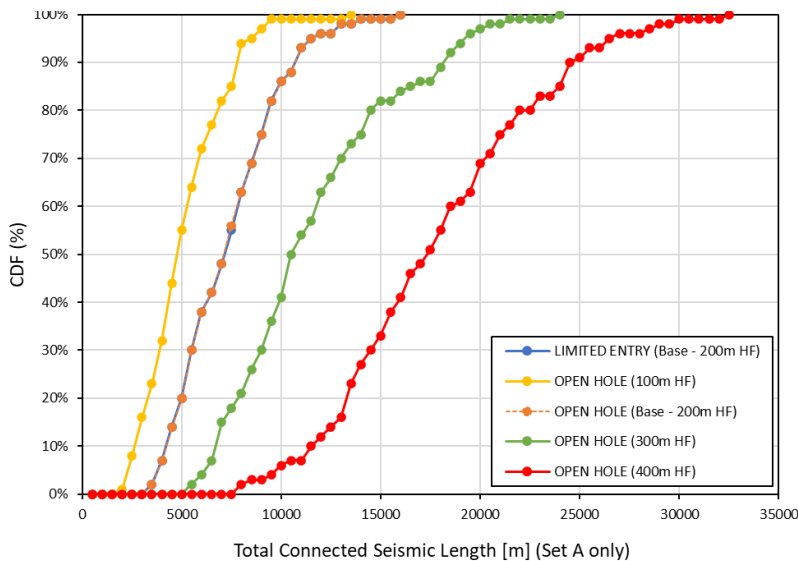


Figure 62: Total connected seismic fault length for limited entry and 4 hydraulic frac length scenarios (2xX_f).

The direct comparison between the 200 m frac lengths, with either open hole or limited entry show identical results, Figure 62. In the case modelled, total connectivity is driven by the presence of the frac extending away from the well. This has been further explored by the cases with different frac lengths ($2 \times X_f$) that show a direct relationship between frac length and connected seismic length. With increasing frac length there is increasing total connectivity.

When the distance of actual events between the two completion types are considered (OP1 v OP3), the distance that events occur from the open hole completion are found to extend further than the cased hole case, Figure 62, right. Whilst not seen directly in the simulations, this is thought to be associated with the probability of directly connecting to reservoir structures. This has been considered further by simulating the likely number of natural structures (>100 m long, Set A and Set B) that would intersect an open hole or cased wellbore completion. Using the calibrated fracture intensity properties for the pad, with the openhole completion, an average of 11 structures intersected the well. Changing to a cased holes with 100 times less open length, resulted in 0-1 structures intersecting any of the three wells on the pad, Figure 63.

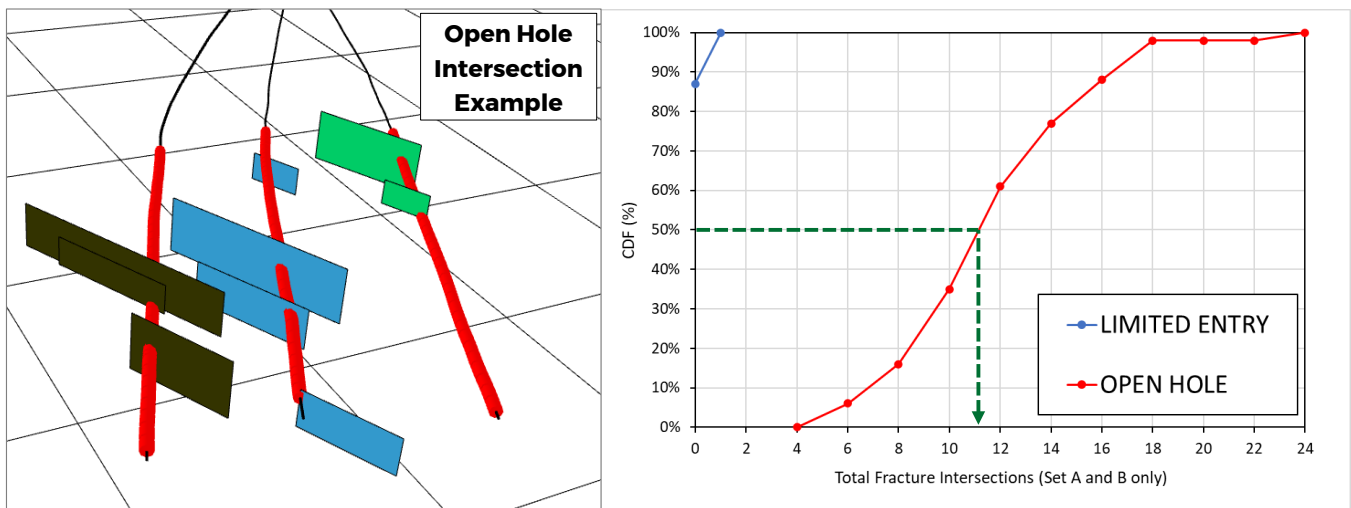


Figure 63: Comparison between left) open hole completions and right) limited entry completions.

In summary, the stochastic simulations show a number of different behaviours:

- Changing from an open hole to cased hole completion has not reduced the overall connectivity of the well to the wider fracture network, with the same connected seismic length in both cases.
- Switching from an open hole to cased completion did significantly reduce the connectivity of larger natural structures from the well bore, reducing the number from ~11 for the lower Montney wells on the pad to ~1.

We cannot conclude that open hole completions are more problematic than cased hole completions when considering the need to reduce induced seismicity. Subsequent to this analysis being undertaken, operations at an adjacent pad to Operator 3's, resulted in a very similar pattern of seismicity, despite using a cased hole completion. Further investigation is required to establish whether switching to cased completions in highly structured areas could provide an effective mitigation strategy.

6.2 Numerical Simulation of Hydraulic Diffusivity

6.2.1 Hydraulic Diffusivity of a Single Fracture (FracMan Hydraulic Model)

Building on the analyses of the characterisation of the fluid pathway and relationship between hydraulic diffusivity and seismic event magnitude in Section 4.0, we have tried to first understand the case of a large hydraulic diffusivity value by simulating fluid injection into a simple fracture geometry. To this end, the model was developed in FracMan. Model geometry and the pressure distribution results after two hours of fluid injection simulation are shown in Figure 64a and b. The fracture is 1000 m long, 25 m tall, and 0.001 m thick (i.e., aperture of 1 mm). The injection well is indicated with the red colour and the observation wells are marked by the blue colour to monitor the pressure front propagation. These wells are located at 150 m distance increments up to 600 m away from the injection well (note that most of the events from the field data are within 600 m distance from the injection source, e.g., Figure 4); Table 6 lists the input parameters for the model. The simulation results are shown in Figure 64c and d. After two hours of injection the pressure changes by 4 MPa at 600 m distance from the injection well. Assuming a pressure perturbation of 1 MPa is adequate to cause shear slip on a fault, a diffusivity value in the range of 3 to 12 m²/s can be estimated, depending on the distance from the injection source (i.e., 150 to 600 m, respectively). Despite its simplicity, this hydraulic model confirms that observation of large hydraulic diffusivity values in a reservoir with partial hydraulic connectivity (i.e., low fracture intensity; see the data analyses in Section 4.0), is reasonable and supports the fact that the dominant mechanism of induced seismicity in such reservoirs can be triggered directly by fluid pressure perturbation.

Note that the distribution of hydraulic diffusivity values is not only dependent on the distance of the event hypocenter from the injection source, but also a function of the shear strength of the ruptured path of the fault which requires a certain amount of pressure perturbation for slip to occur. In other words, if the shear strength along a structure varies due to differences in asperities (friction) and/or rock bridges (cohesion), then failure and slip may occur across different fault segments (or patches) in response to a range of possible pressure perturbations.

Table 6: Input properties used for the FracMan model simulation of hydraulic diffusivity in a single fracture.

Parameter	Value	Units
Compressibility	10 ⁻⁵	Psi
Injection Rate	1.5 × 10 ⁻⁴	m ³ /min
Kh ^(a)	100,000	mD.m
Viscosity	1	cP
Initial fluid pressure	30	MPa

(a) Kh = Fracture Transmissivity

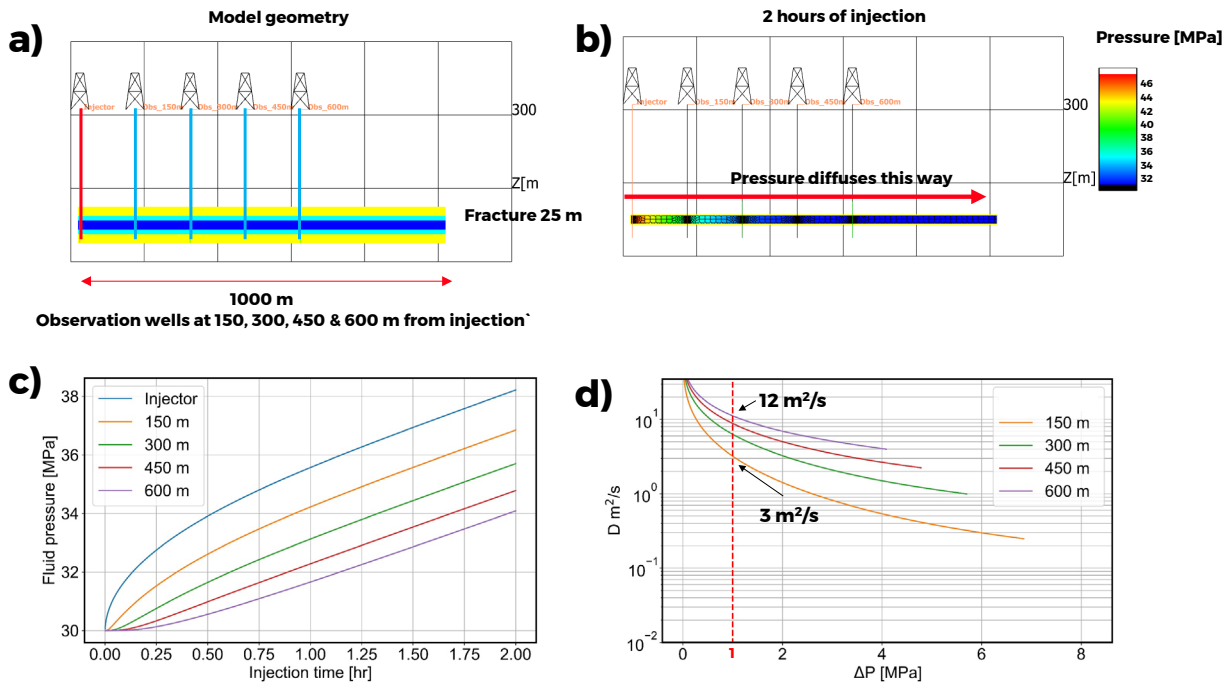


Figure 64: FracMan well test modelling, studying the physical concept of hydraulic diffusivity values for injection along a single fracture. a) Model geometry and the location of the observation wells (blue) relative to the injection well (red). b) Pressure distribution along the fracture after two hours of injection simulation. c) Pressure profile during the injection time at each well. d) Plots of the hydraulic diffusivity as a function of pressure perturbation.

6.2.2 Fracture Intensity Impact on Hydraulic Diffusivity Modelling (XSite™)

To more rigorously investigate the observed empirical analyses in Section 4.0, in particular the seismic event distribution in $r - t$ space, and to understand the connection between hydraulic diffusivity and injection induced seismicity in the Kiskatinaw area, we have performed a series of numerical simulations using the commercial hydraulic fracture simulation program XSite™ (Itasca, 2022). This program employs a fully-coupled hydro-mechanical bonded-lattice modeling technique, the assumptions and formulation for which are described in detail by Damjanac et al. (2020). The XSite™ model was set up to investigate the effect of fracture intensity on the spatio-temporal distributions of induced events, as well as to study the corresponding dominant event mechanisms.

6.2.2.1 Model set up

Two model geometries were developed based on the interpreted structures of OP1 (see Section 3.0); this is shown in Figure 65. These correspond with the two distribution patterns observed in $r - t$ space (Figure 42). Instead of propagating a hydraulic fracture to intersect a pre-existing fracture network which is computationally demanding, we created a model that represents our inferred system; i.e., hydraulic fractures intersecting a fracture corridor that transfers pressure increases. The simplifications adopted in the model were judged to be reasonable relative to the primary aim of modelling fluid and pressure propagation along a pre-existing fracture corridor under stressed conditions, as opposed to simulating the hydraulic fracture propagation itself. For these simulations the focus was placed on capturing the physics of fluid pressure perturbation and stress transfer due to fluid injection operations into different geological structures, to gain understanding of the mechanisms behind the observed seismic event distribution patterns.

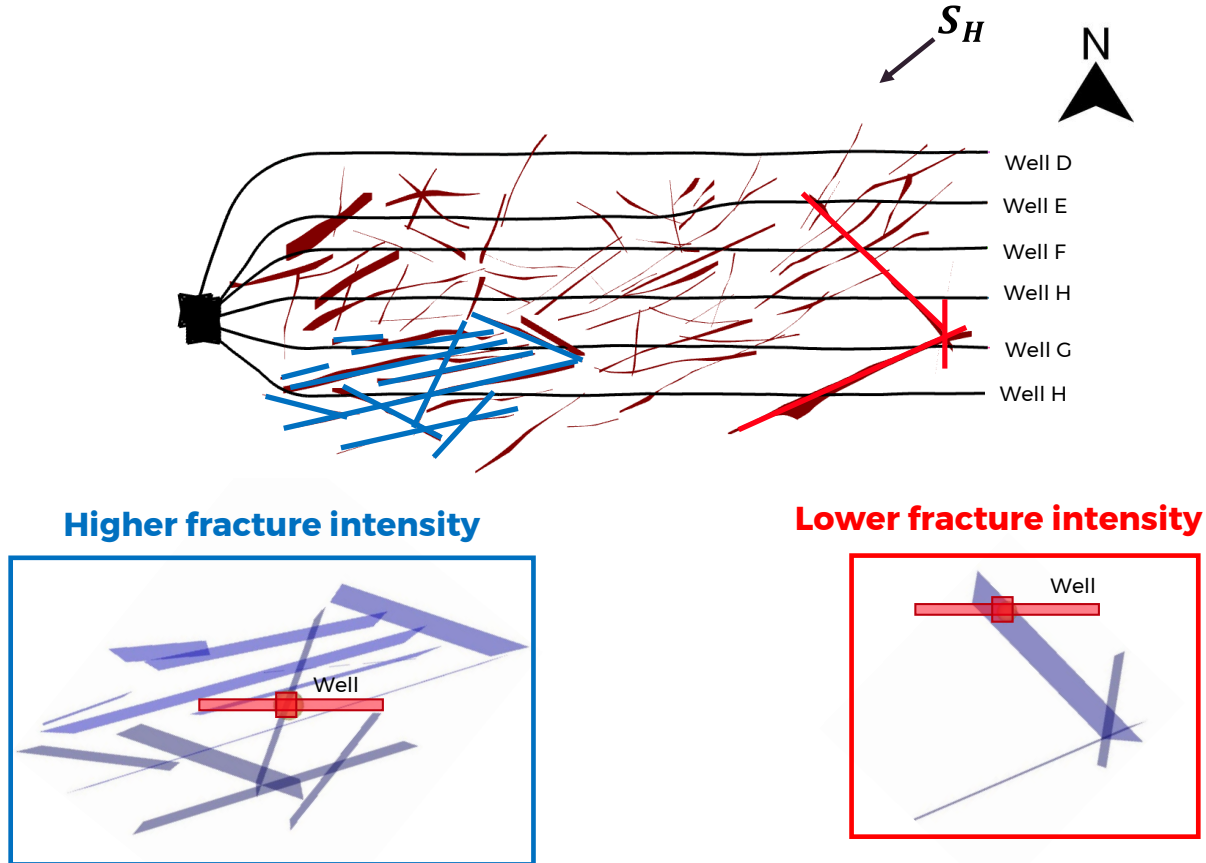


Figure 65: Representation of the fracture intensity connection with the active stage used to construct the XSite™ models. The blue box represents the high fracture intensity area of the reservoir, where the structures are well connected. The red box illustrates the low fracture intensity area of the reservoir, which incorporates only a few connected structures.

The model was setup using the input properties listed in Table 7. The top of the model is at 1.6 km depth; the initial stress and fluid pressure conditions are calculated accordingly. One hour of fluid injection was simulated at a rate of 5 m³/min. To facilitate comparison, all models were subjected to the same fluid injection volume. The reservoir domain is represented by a lattice of bonded particles whose generation requires the assignment of contact properties at each bond. These are calibrated to arrive at the reservoir-scale properties (as listed in Table 7), but also allow for strength heterogeneity to be assigned through groupings of individual contacts as patches or segments along a structure. This introduces a more realistic behaviour as most faults are not perfectly planar (as represented in the model) and would have varying frictional properties due to geometrical or asperity variability (e.g., see Scholz 2019). Note that Figure 65 only represents a zoomed in snapshot of the model where the fracture and the injection well are shown for illustration purposes; however, the boundaries of the model are much larger to ensure no numerical artifacts due to boundary effects. Throughout the Section 6.2.2, we use red and blue colors to indicate the low fracture intensity model (LFIM) and high fracture intensity model (HFIM), respectively. This also corresponds with the previously presented empirical analyses and conceptual model shown in Figure 47.

Table 7: Input properties for XSite™ models used to investigate fluid-injection-induced seismicity sensitivity to reservoir fracture intensity.

Property	Value
S_{Hmax} (S_y) gradient (Azimuth 44°)	35 MPa/km
S_{Hmin} (S_x) gradient (Azimuth 134°)	20 MPa/km
S_v (S_z) gradient	25 MPa/km
Pore pressure gradient	14 MPa/km
Injection rate and duration	0.08 m ³ /s for 60 minutes
Fault frictional properties	$\mu = \tan(30^\circ)$, Cohesion = 1 MPa
Formation mechanical properties	E = 55 GPa, $\nu=0.22$
Model dimension	X = 1.6 km, Y = 1.8 km, Z = 1.5 km

6.2.2.2 Results and Discussion

Figure 66a shows a plan view of the pressure perturbation after one hour of fluid injection simulation. As can be seen, the same volume of injected fluid into the LFIM scenario results in a higher pressure buildup in the structures than that for the HFIM. This agrees with observations of higher-pressure buildup in the east side of the OP1 reservoir which entails a lower fracture intensity (see Figure 48a and Figure 25b). The higher-pressure buildup results in a larger cumulative seismic moment release, as shown in Figure 66b, and this aligns with the conceptual model explained in Section 4.4. Additionally, the seismic efficiency (Figure 66c) at the beginning of the fluid injection for the LIFM (red box) shows that most of the hydraulic energy input is used for Mode-I tensile fracture opening. The corresponding values are within an order of magnitude of those reported for hydraulic fracturing operations (i.e., $I_{eff} < 10^{-5}$; see Maxwell et al., 2008; Goodfellow et al., 2015). These are likewise dominated by Mode-I tensile fracturing. As the pressure gradient in the lower fracture intensity network builds up, its more contained nature (i.e., lower storativity) results in a more elongated pressure front propagating away from the injection point until it activates the distal structure it intersects. The more intense interaction between the pressure front and structure in this case causes a slip event where the seismic efficiency grows by a factor of ~100.

For the HFIM scenario (blue box), the pressure buildup within a larger and more diverse and connected fracture network initially results in a large number of small shear slip events closer to the injection source. The hypocentral cloud of seismicity grows as the pressure front travels away from the injection source, as can be seen in the seismic energy efficiency curve for the HFIM model (Figure 66c). The corresponding seismic energy efficiency values are more than an order of magnitude larger than the typical values for hydraulic fracturing, suggesting that a higher percentage of the input hydraulic energy is being used to trigger shear slip (i.e., activation of shear events) along seismogenic-susceptible structures.

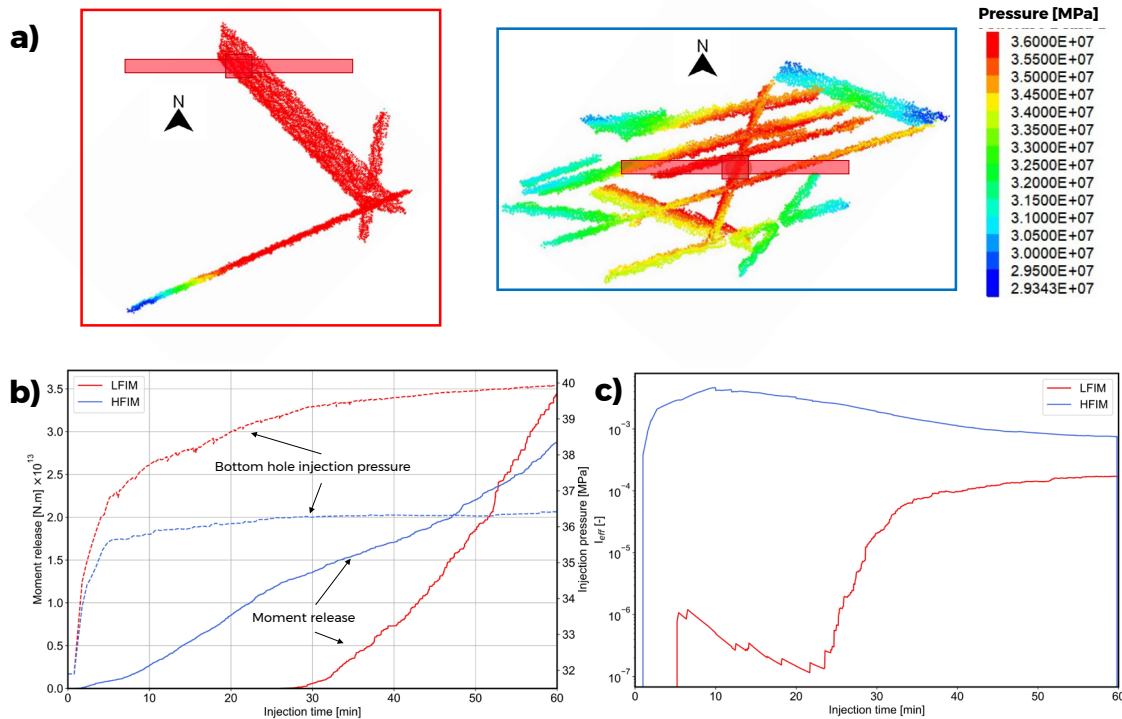


Figure 66: Impact of fracture intensity on XSite™ modelling of fluid-injection-induced seismicity. a) Pressure distribution after 1 hour of injection into the low fracture intensity model (LFIM), left, and high fracture intensity model (HFIM), right. b) Comparison of the bottom hole injection pressure and cumulative seismic moment release during fluid injection for both models. c) Seismic energy efficiency for both models during the full injection time record.

Figure 67 compares the $r - t$ plot, hydraulic diffusivity, and the magnitude distributions of the induced seismic events for both the LFIM and HFIM XSite™ models. First, it can be seen that the LFIM and HFIM numerical output reproduce the same observed non-parabolic and more typical parabolic signatures, respectively, for the seismic event distribution as observed in the field data (compare Figure 67 with the field data in Figure 42 and Figure 47). Next, comparison of the hydraulic diffusivity distributions show an average of 8 m²/s for the LFIM and 1 m²/s for the HFIM. These values are in good agreement with our empirical analyses results from Section 4.0, and show the same relationships between the hydraulic diffusivity values and number of connected fractures (see Figure 49). Furthermore, similar to the results obtained from the FracMan modelling of hydraulic diffusivity for a single fracture (Section 6.2.1), the XSite™ simulations show that the large hydraulic diffusivity values for fracture networks observed in the data are not only reasonable, but also physically understandable. Analyzing the event distribution of the models in Figure 67, one can see (as explained in Section 4.4) that a larger interconnected fracture network (HFIM) results in a more radial distribution of the injection pressure, which in turn influences a larger number of structures with varying orientations (i.e., more geometrically complex) at a lower pressure buildup (Figure 66a). This results in a seismic moment release through many small events. Figure 66b and c show for the first half of the fluid injection, a larger cumulative seismic energy release as well as seismic energy efficiency for the HFIM scenario (blue curve), but where these are primarily released through many small seismic events ($M_w < 1$). In contrast, the more intense pressure buildup along the more restricted fracture travel path in the LFIM model resulted in more relatively large seismic events ($M_w > 1$). The low fracture intensity of the reservoir resulted in higher pressure buildup, larger hydraulic diffusivity, and bigger seismic events (see also Section 4.4).

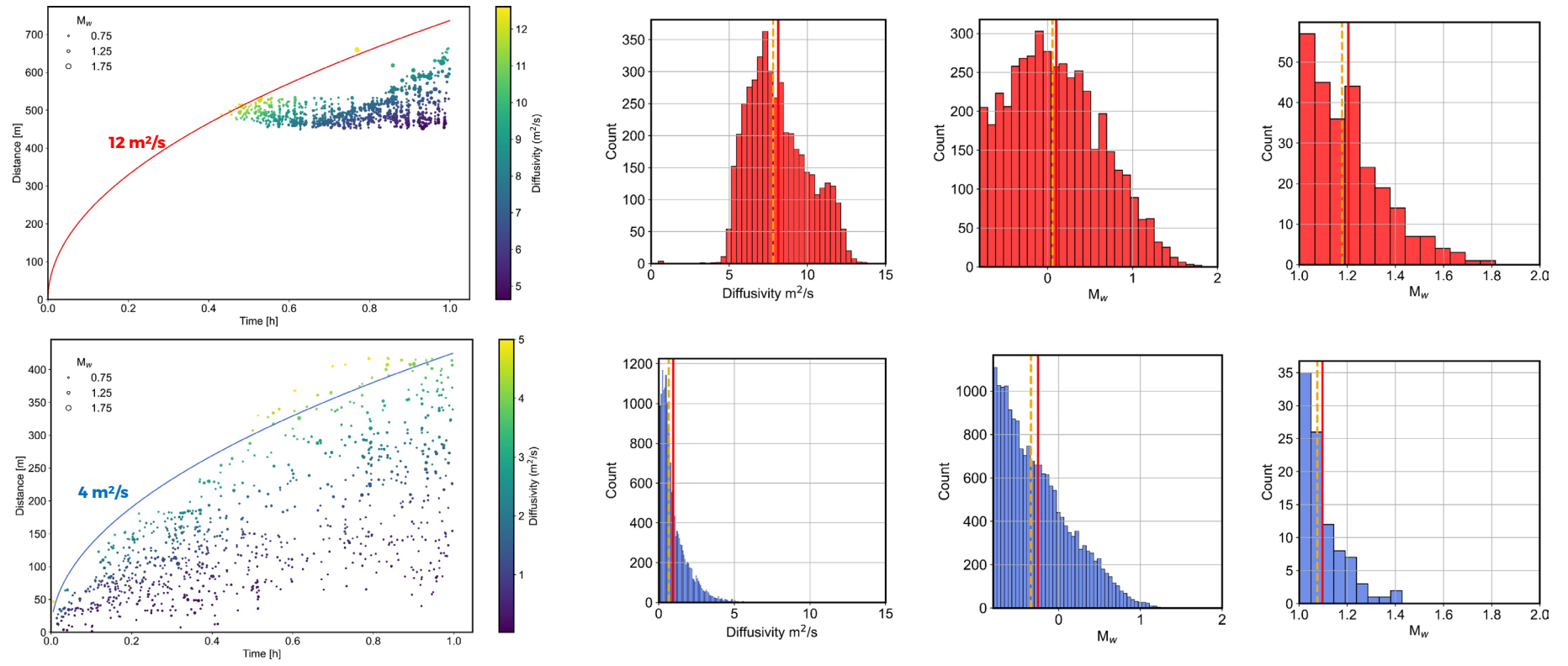


Figure 67: $r - t$ plot, hydraulic diffusivity and induced seismicity magnitude distributions for the LFIM (top row) and HFIM (bottom row) models. The solid red and dashed orange lines indicate the mean and median values, respectively.

6.3 Simulation studies of potential mitigation strategies

The mechanistic learnings from the empirical analyses (Section 4.4) and numerical modelling (Section 6.2.2) suggest that injection into a lower fracture intensity area of a reservoir can be associated with higher hydraulic diffusivities causing larger cumulative moment release and consequently larger induced seismicity event magnitudes. Using the LFIM XSite™ numerical model from Section 6.2.2, we investigated the effect of fluid injection rate on the seismic response of the reservoir. For this, three different mitigation controls were numerically simulated and are presented in the following sub-sections.

6.3.1 The Impact of Injection Rate Ramp-up on Seismicity

Two different fluid injection ramp-up rates to a targeted rate of $\sim 5 \text{ m}^3/\text{min}$ were modelled. One represented a rapid injection ramp-up rate over 5 minutes, and the other a slow injection ramp-up rate over 15 minutes. These are shown in Figure 68a. Both models maintained the same total fluid injection volume (276 m^3).

By analyzing the bottom hole pressure at the end of the injection simulation (dashed curves in Figure 68b), one can see that a similar pressure is reached after 35 minutes of injection. However, the cumulative seismic moment release during the same time is larger for the rapid injection ramp-up. This can also be observed by comparing the seismic energy efficiency for the models (Figure 68c), where after 20 minutes of injection, most of the input hydraulic energy is transformed into seismic energy when the injection ramp-up occurs in a shorter amount of time. In the first 20 minutes of the simulation, the rapid injection ramp-up results in a larger bottom hole pressure. The larger pressure buildup in this case is mostly seen to drive mode-I tensile fracture opening (Figure 69, top row), and hence the seismic energy efficiency is smaller. However, the larger bottom hole pressure buildup also causes a larger pressure gradient in the fracture, and thus promotes a larger pressure perturbation propagating a farther distance away from the injection source (Figure 69 bottom row).

This can be further investigated by analyzing the hypocentral growth rate (i.e., the hydraulic diffusivity; see Section 4.0), radial distance of the hypocenters relative to the injection source, the delay time of seismic event occurrence since the start of injection, and large event magnitude distributions (Figure 70). Comparing the mean value for the hydraulic diffusivity (solid red line), it can be seen that the rapid injection ramp-up resulted in hydraulic diffusivity values almost 2-fold larger than those of the slow injection ramp-up. The analysis of the pressure diffusion distance for both models shows that the pressure perturbation has propagated farther away from the injection source for the case of rapid injection ramp-up. The time delay is slightly shorter for this case, and therefore the pressure perturbation diffusion in the system is faster.

It should also be noted that at end of the stimulation, the cumulative seismic moment for both models are almost the same; however, more induced events with larger magnitudes are observed for the rapid injection ramp-up. This might suggest that even though the overall moment release and shear slip is almost the same at the end of both simulations, the seismic moment release for the rapid ramp-up is through larger induced events instead of many small event magnitudes as was the case for the slow ramp-up.

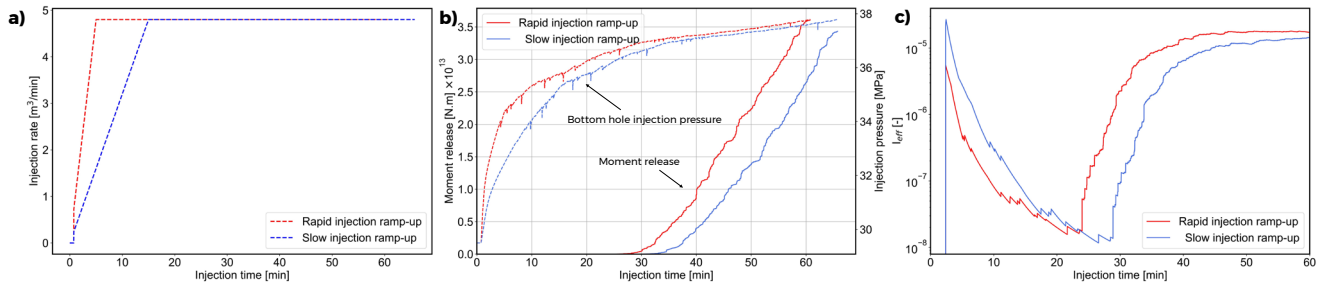


Figure 68: a) Simulated injection rate inputs for the rapid and slow ramp-up models. b) Injection pressure and cumulative seismic moment release over the injection time. c) seismic energy efficiency for each model.

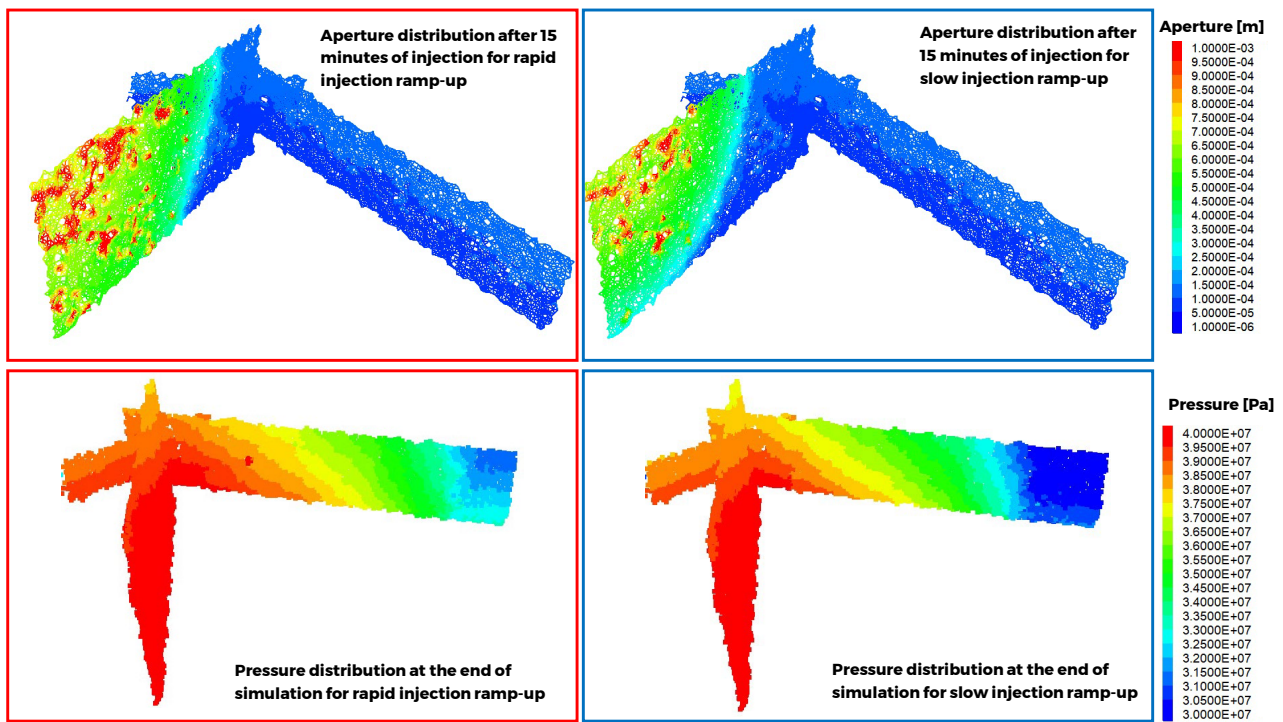


Figure 69: Aperture distribution after 15 minutes of fluid injection (top row) and pressure propagation at the end of injection simulation (bottom row), for the rapid (left column) and slow (right column) ramp-up scenarios.

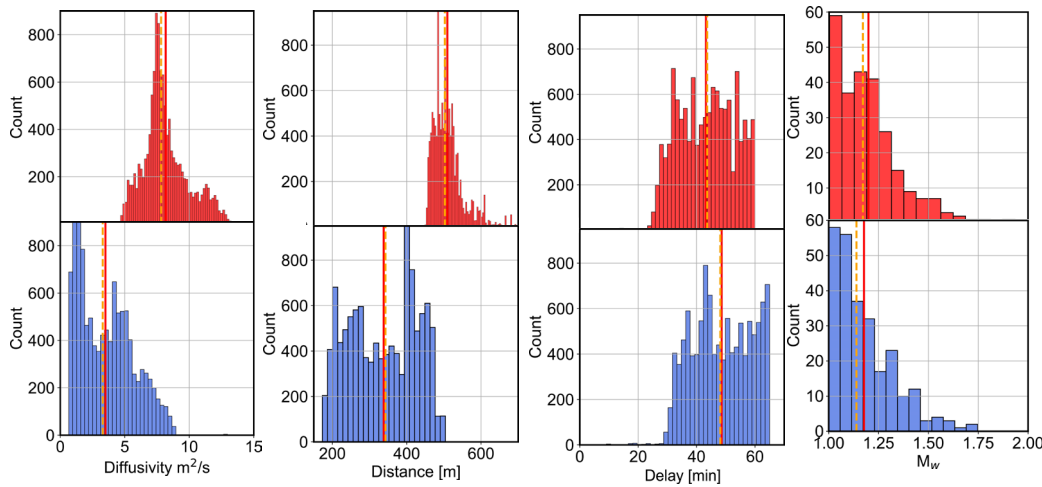


Figure 70: From left to right: hydraulic diffusivity, hypocenter distance from injection source, event occurrence delay since the injection start, and seismic event magnitude distribution, for the rapid (top) and slow (bottom) ramp-up models. The solid red and dashed orange lines indicate the mean and median values, respectively.

6.3.2 Impact of Alternating Injection Rates on Seismicity

The impact of alternating fluid injection rates, between high and low, on the seismic response of the reservoir was tested using the previously described low fracture intensity model (LFIM). The simulated alternating injection rate patterns are shown in Figure 71a. Similar, but less systematized, injection rate variations are observed in the OP3 dataset (Figure 71b), where the pressure perturbation associated with the open hole completion for the first 13 stages activated the same structures repeatedly (note that the injection data for OP1 is not similarly detailed enough to allow similar plots to be constructed).

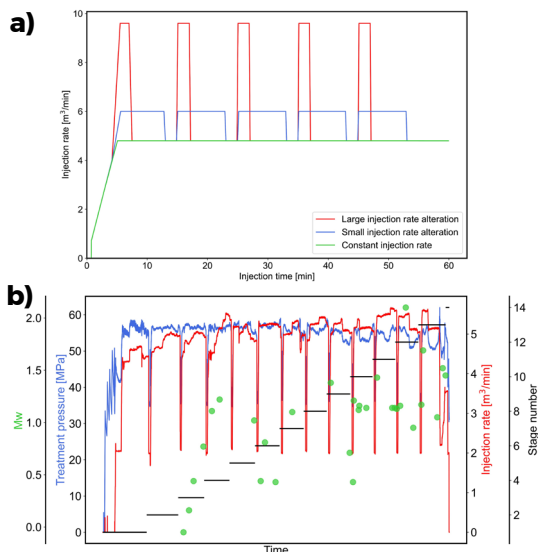


Figure 71: a) Shows the injection scheme in all three simulation cases, note that the same amount of fluid was injected (300 m^3) and the injection time therefore is varying (the longest injection time is for the constant injection pressure). b) Illustrates the injection in the first 13 stages of OP3 well A2. Each stage duration is shown by the black horizontal segmented line, the color of the curve matches its corresponding axis.

For all three models, 300 cubic meters of fluid was injected. The bottom hole pressure data as a function of injection time are shown by the dashed curves in Figure 72a. The two models simulating large and small alternating injection rates (indicated by the red and blue colours, respectively) generated bottom hole injection pressure pulses, while the constant injection rate did not cause any significant pressure changes. By analyzing the cumulative seismic moment release (the solid curves in Figure 72a), it was found that both models simulating alternating injection rates experienced pressure pulses that resulted in larger seismic release compared to the constant injection rate scenario. The almost identical cumulative seismic moment release for these two models suggests that even a small alternating injection rate (and consequent pressure pulses) into seismogenic structures may cause larger cumulative moment release. This can also be observed in the seismic energy efficiency curves where the alternating injection rate models have a larger hydraulic energy input into the system, and most of this energy is converted into seismic energy release (recall I_{eff} is the ratio of cumulative radiated seismic energy release to input hydraulic energy; see Maxwell et al., 2008).

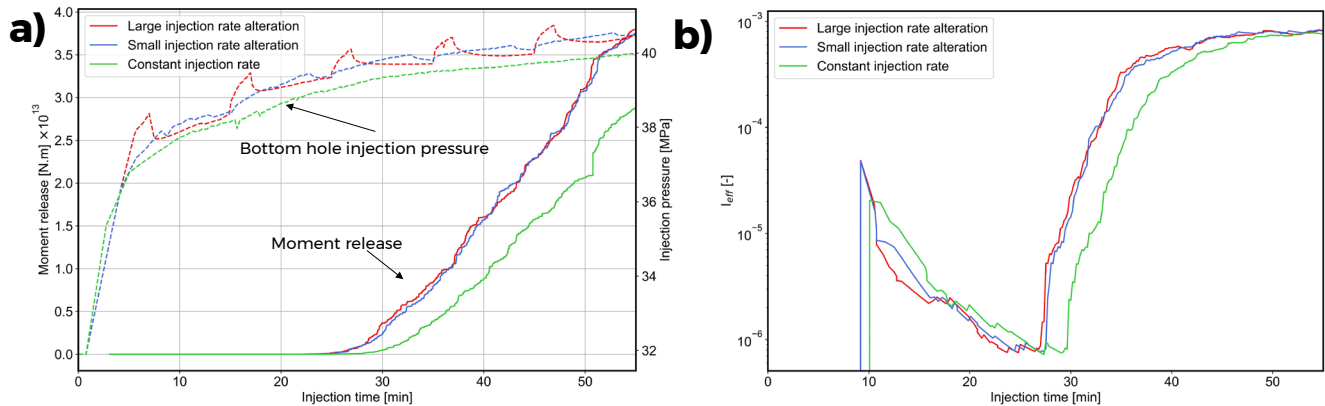


Figure 72: a) Bottomhole pressure and cumulative seismic moment release during fluid injection for three cases: small versus large alternating injection rates versus constant injection rate. b) Seismic energy efficiency during the same simulated injections.

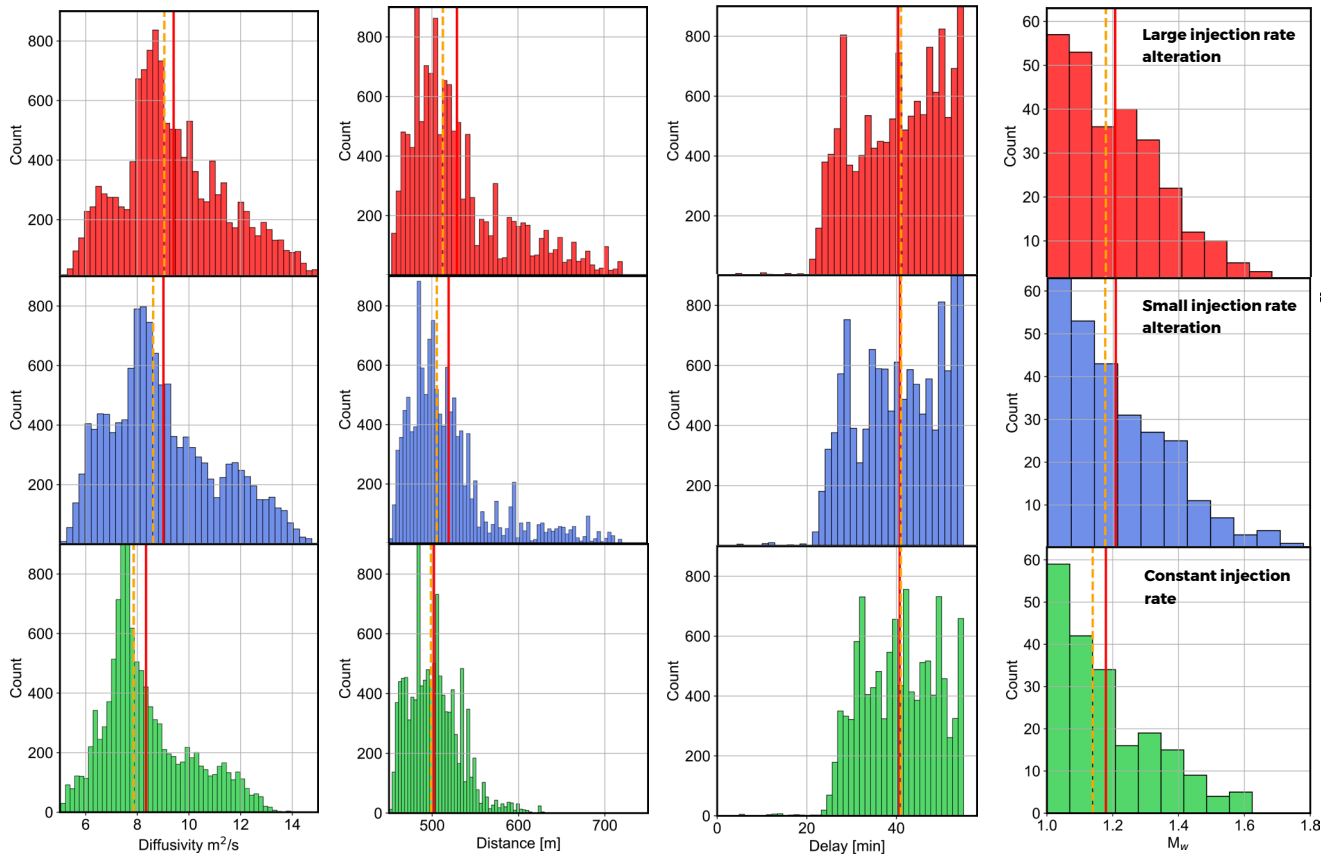


Figure 73: a) Bottomhole pressure and cumulative seismic moment release during fluid injection for three cases: small versus large alternating injection rates versus constant injection rate. b) Seismic energy efficiency during the same simulated injections.

Comparing the hydraulic diffusivity values for all three models (Figure 73; left column), we found that generally the hydraulic diffusivity values are the largest for the large alternating injection rate followed by the small alternating injection rate and then the constant injection rate. By analyzing the radial distance distribution of the seismic events relative to the injection source and the time delay since the start of injection, it can be seen that these larger hydraulic diffusivity values are mostly due to larger hypocentre distances from the injection source (recall $D \propto r^2/t$; see Section 4.0). This means that the pressure perturbation has reached a greater distance along the fracture network for the cases simulating an alternating injection rate. Moreover, given that the fracture geometry, stress state and frictional strength are the same for all three cases, the larger pressure buildup caused by the alternating injection rate and subsequent farther distance travelled by the pressure front from the injection source, results in a larger shear stimulated area and therefore a larger cumulative moment release (Figure 72a). This in turn results in larger magnitude events (Figure 73).

Thus, the model results suggest that even a small alternating rapid fluid injection rate and its consequent pressure pulse, can result in both more and larger induced seismicity events.

6.3.3 Model Calibration of Stage 12 of OP3 Well A2

To further advance the numerical investigation, we developed a calibrated XSite™ model based on the data for stage 12 from OP3's well A2 (A full view of the event distribution in 3D and in r-t space is shown in Figure 36b). The geometry of this model is shown in Figure 74, and the input properties are similar to those in Table 7 except that the shear strength properties of the fault (i.e., NF2 in Figure 74) were modelled as: $\mu = \tan(37^\circ)$, cohesion = 7 MPa, and a dilation angle of 7 degrees was set so that any excessive fluid pressures can dissipate after shear slip. The calibration of these properties was achieved through iteration until a good match between the simulation and the observed field data was observed. Agreement in fit was based on generating the same event magnitudes at the same times as recorded in the field data (Figure 75). Since no other structures appeared to be activated during the field injection, stronger frictional properties were assigned to the pre-existing fracture corridor (NF1 in Figure 74).

Similar to the reasons explained in 6.2.2.1, we did not propagate a hydraulic fracture but instead inserted one with reasonable dimensions. Also, a higher pore pressure gradient was selected for the model calibration (i.e., 17 MPa/km versus 14 MPa/km used in Section 6.2.2.1). This is due to the open hole completion used for OP3. In fact, we observed that stages 9 to 11 also caused seismicity on the same structure, which means that the structures are mostly connected and the elevated pressure due to prior injection should be considered as an initial condition for stage 12. Therefore, we injected for 3 hours (the duration of injection stages 9 to 11) prior to simulating stage 12, and this resulted in an elevated pore pressure gradient of about 17 MPa/km. Stage 12 was then simulated using the field-based injection time (56 minutes) and average injection rate (5.3 m³/min). The model calibration targeted the largest seismic event with a magnitude of 2.1, which was recorded after 26 minutes from the start of fluid injection for stage 12. The best fit numerical result was the simulation of a magnitude 2.5 event after 23 minutes of fluid injection (Figure 75). We believe that the result of this model is in good agreement with the field data. The added confidence in having a reasonably well calibrated model allows for sensitivity analyses to be run to test the impacts of changing key operational factors.

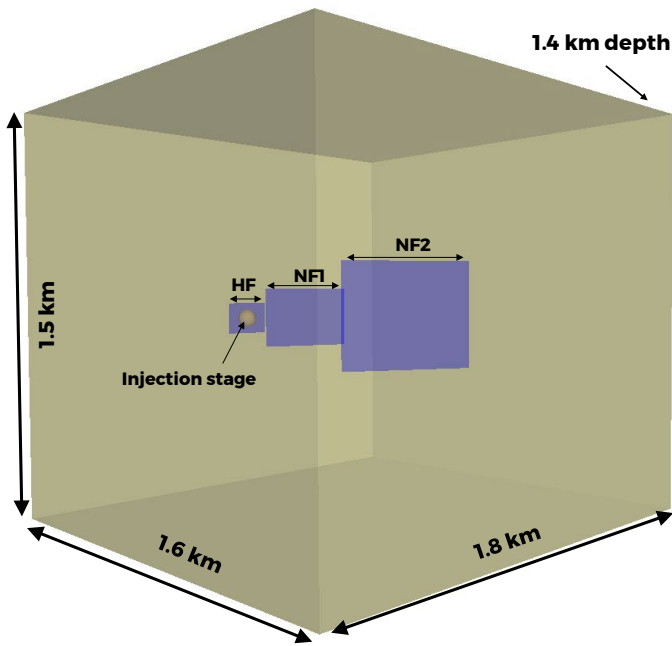


Figure 74: XSite™ model for Stage 12 of OP3 well A2 used for calibration exercise. In this scenario, a hydraulic fracture (HF) is connected to natural fractures NF1 and NF2 in series. The dimension of the model is shown, and the top of the model is located at 1.4 km depth.

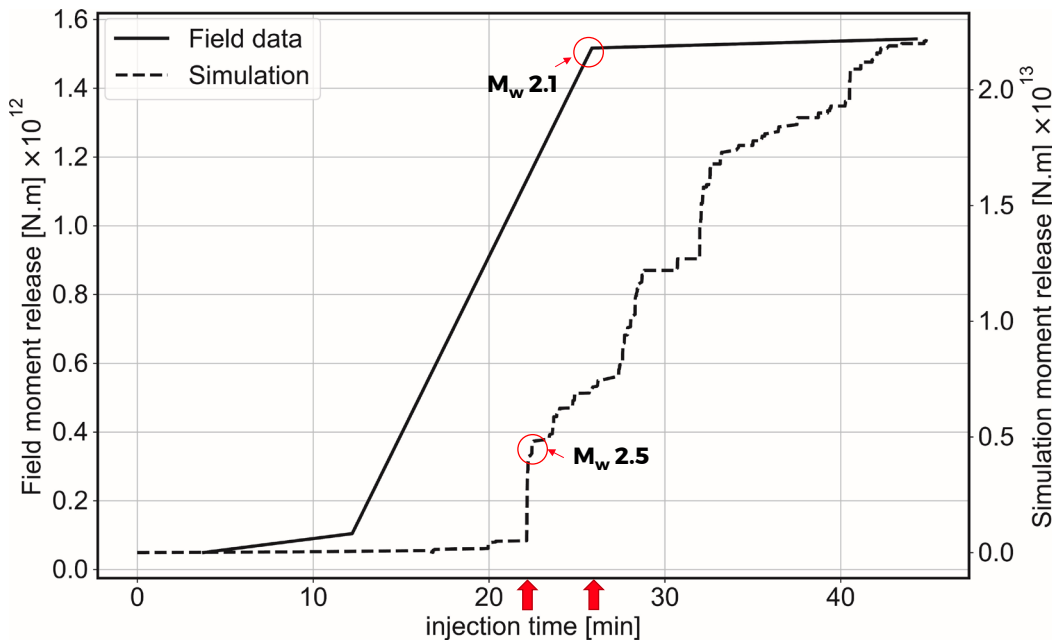


Figure 75: Comparison of the field-measured cumulative seismic moment release for stage 12 of OP3's well A2 and that achieved in the calibrated model. The red circles show the event magnitude, and the red solid arrows indicate the occurrence time for each event.

Building on the calibrated base model, the influence of injection rate ramp-up to the target injection rate of 5.3 m³/min (Figure 76a) was tested, comparing those for a rapid (15 minutes) and slow (1.5 minutes) ramp-up to the base case (5 minutes). We analyzed the cumulative seismic moment release, bottom hole pressure, and the seismic energy efficiency for these models in Figure 68b and c. Note that since the injection volume is the same for all three models, the rapid injection ramp-up results in a shorter injection time. Similar to previous results testing the injection ramp-up rate for the LFIM models (Figure 68), the seismic moment releases for all three models are almost identical at the end of the injection simulation. By comparing the pressure and cumulative seismic moment release curves after 30 minutes of injection, one can see that even when the bottom hole pressure is higher for the slow injection ramp-up, this model generated less seismic moment. This is also reflected in the seismic energy efficiency results for the slow injection ramp-up; despite having a larger bottom hole injection pressure and the same injection rate, it has a lower I_{eff} .

The sharp increase in cumulative seismic moment release seen in the curves for all three cases can be interpreted as sudden large shear slips (identified by the dashed magenta ellipses in Figure 76b). For the case of the slow injection ramp-up, the cumulative seismic moment release increases more gently with fewer and smaller sudden moment releases. For instance, the ellipse shown by the red arrow in Figure 76b compares the sudden seismic moment release for an event seen in all three models during which the bottom hole pressure is almost the same. However, it can be seen that the seismic moment release for the slow injection ramp-up is smaller than those for the other two models.

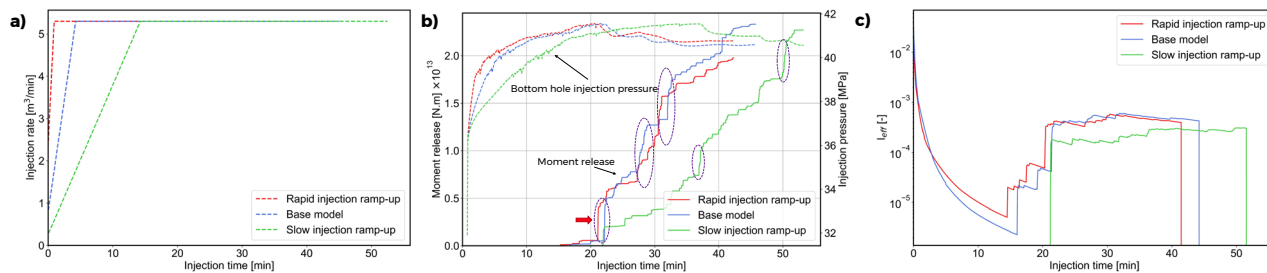


Figure 76: a) Injection volume ramp-up rates implemented in models comparing a fast and slow injection ramp-up to that for the calibrated base case. b) Injection pressure and cumulative seismic moment release over the injection time. The dashed magenta-coloured ellipses on the cumulative moment release curves identify sudden moment seismic releases in the form of large slip events. c) seismic energy efficiency curves for each of the three models. Note that the base model refers to the calibrated model.

The larger shear slip events can explicitly be observed by plotting the shear slip displacements on the sesimogenic structure for each model (Figure 77; top row). The pressure perturbation front for each model is indicated by the red vertical arrow in the bottom row of Figure 77. The pressure front in the slow injection ramp-up has not invaded an extensive area of the fault, and therefore activates only a smaller area relative to the other two models. In other words, similar to the interpretation of the LFIM analysis presented earlier, the slow injection ramp-up releases the stored elastic energy of the structure through numerous small events rather than a few large magnitude events (see magnitude distributions in Figure 78). This can also be seen in the diffusion of the seismic events in Figure 78, where despite events showing almost the same radial distance distribution from the injection source, the delay time distribution is longer for the slow injection ramp-up. This means that it takes longer for this gradual pressure buildup to exceed the critical shear strength of the fault. However, such differences in event magnitude and the sudden moment release are not significant, and it seems that the injection rate ramp-up may have moderate effect on the magnitude of the induced seismic events. It should be noted nonetheless that the alternating injection rate may have a significant effect on the induced seismicity response of the reservoir. This might be related to the consequent pressure pulse and therefore it should be studied for more definitive assessment. Related to this, in the next section, we will study the effect of injection pressure rate on seismicity.

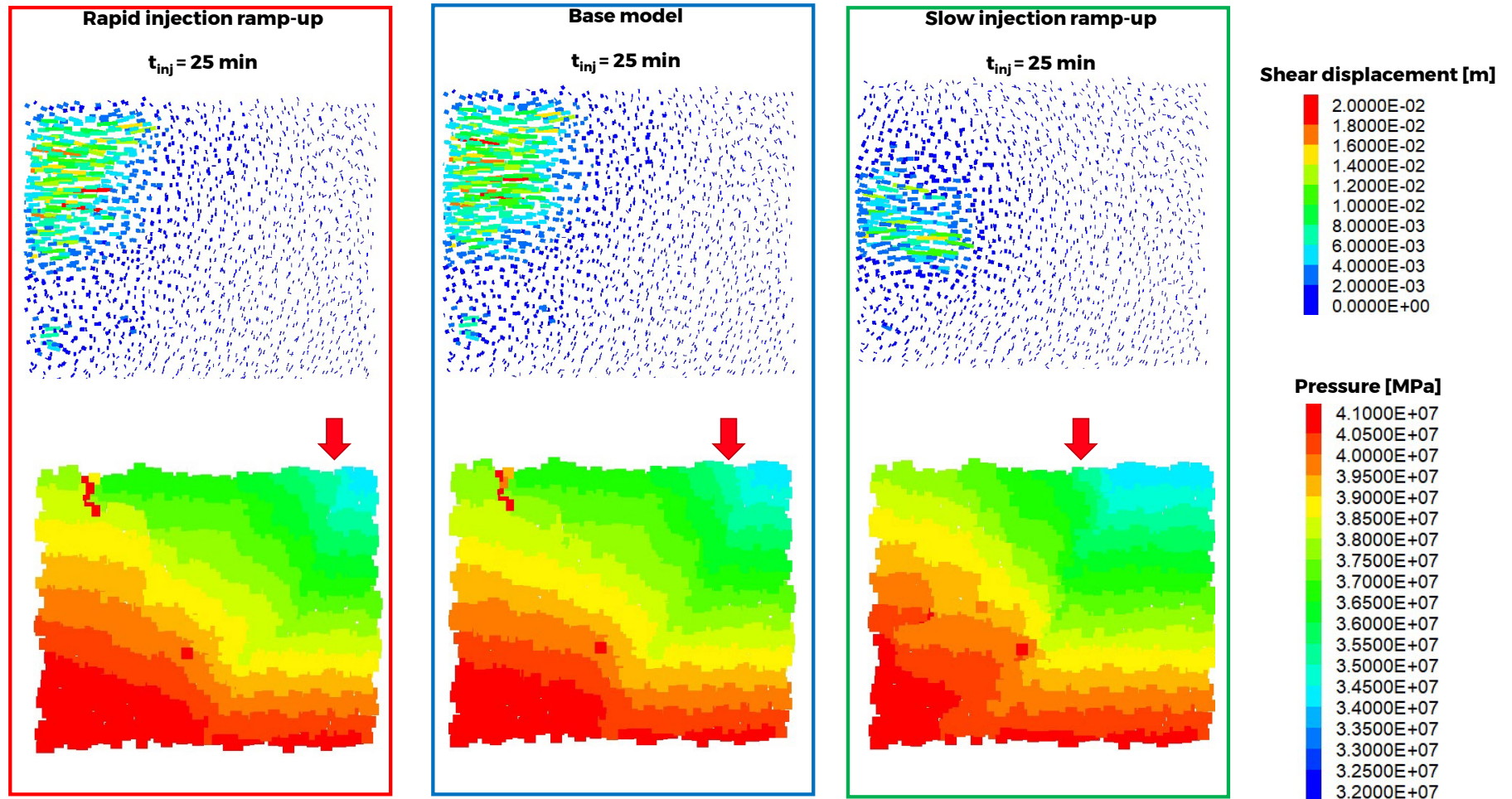


Figure 77: Plan view of the shear slip magnitudes (top row) and pore pressures (bottom row) on the fault after 25 minutes of fluid injection for the rapid (left column) and slow (right column) ramp-up volume rates relative to the calibrated base model (middle column). The location of the pressure perturbation front is shown by the red arrows.

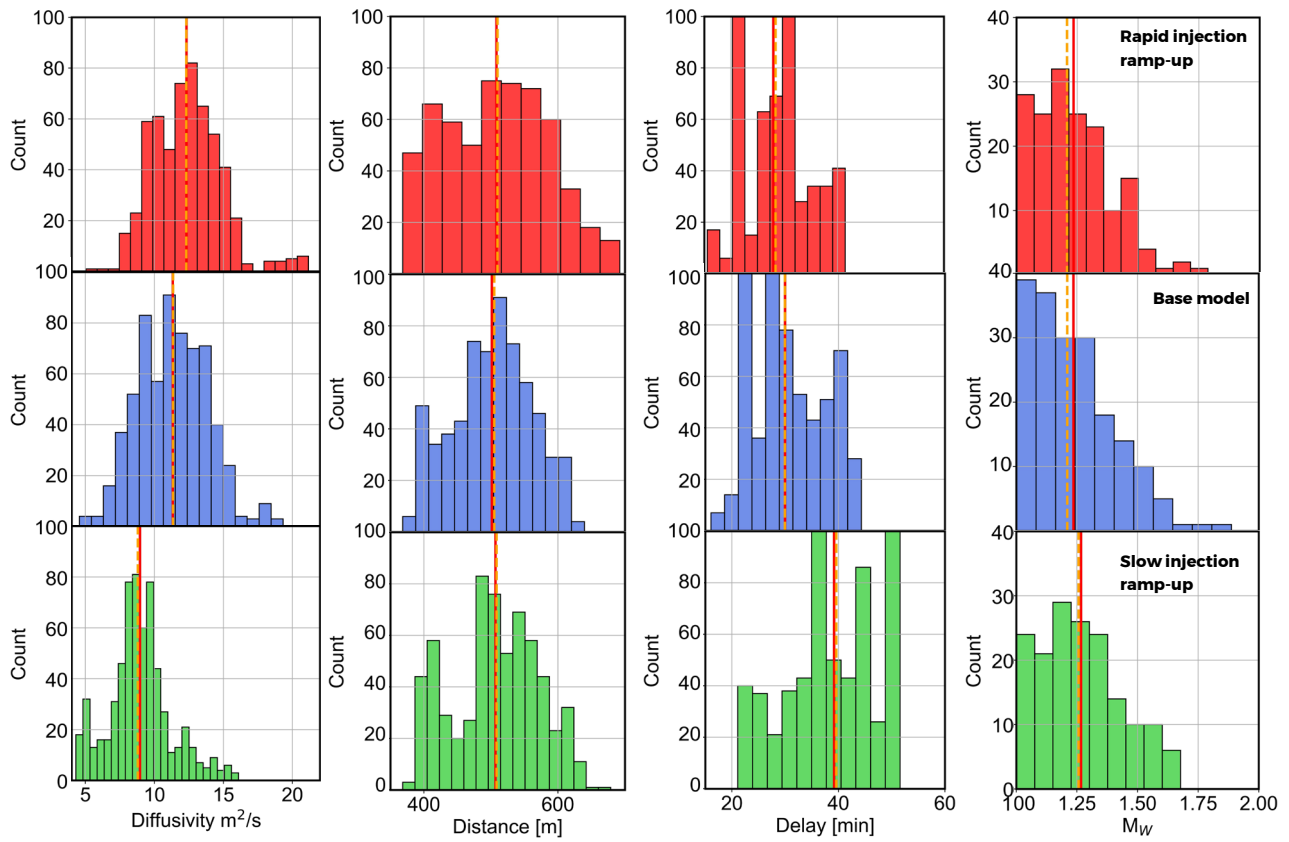


Figure 78: Results for the rapid (top row), calibrated (middle row) and slow (bottom row) injection volume ramp-up rate models, showing from left to right, hydraulic diffusivity, hypocenter distance from injection source, event occurrence delay since the injection start, and seismic event magnitude distribution. The solid red and dashed orange lines indicate the mean and median values, respectively.

6.3.4 The Impact of Pressurisation Rate on Seismicity

The results of the empirical analyses (Section 4.4) and numerical modeling (Section 6.2.2) suggest that there might be a relationship between the injection pressure rate and the consequent seismic response. Laboratory studies of injection into a saw-cut fracture (Wang et al, 2020) as well as numerical simulations of dam reservoir impoundment induced seismicity events (Talwani et al., 2007), suggest that the pressurization rate (i.e., the rate of pressure change over time) have a profound impact on the seismic response of the system. To test whether similar observations can be extended to field-scale hydraulic fracturing fluid injection, we used the calibrated model to investigate the pressurization rate effect on induced seismicity. (Note that the calibrated model was achieved using the injection volume rate).

The injection pressure (pressurization) rate along with the corresponding cumulative seismic moment release are shown in Figure 79. By analyzing the cumulative seismic moment release behavior, we found that at any given time, the seismic moment release is clearly largest for the rapid injection pressure ramp-up. This can also be seen by comparing the shear slip of the seismogenic fracture at the same injection time. Figure 80 for instance shows that the largest shear slip area is associated with the rapid pressurization rate.

Rapid pressurization results in a faster pressure diffusion. This is clearly reflected in the hydraulic diffusivity, radial distance and the delay time derived from the seismic data in Figure 81. Moreover, unlike the marginal differences observed in the injection rate sensitivity analysis (Figure 70 and Figure 78), there is a relatively significant difference in terms of the number of seismic events (the counts) and their magnitudes with the given pressurization rates. In fact, there are more events with $M_w \geq 1$ for the rapid pressurization rate in comparison with the other two models.

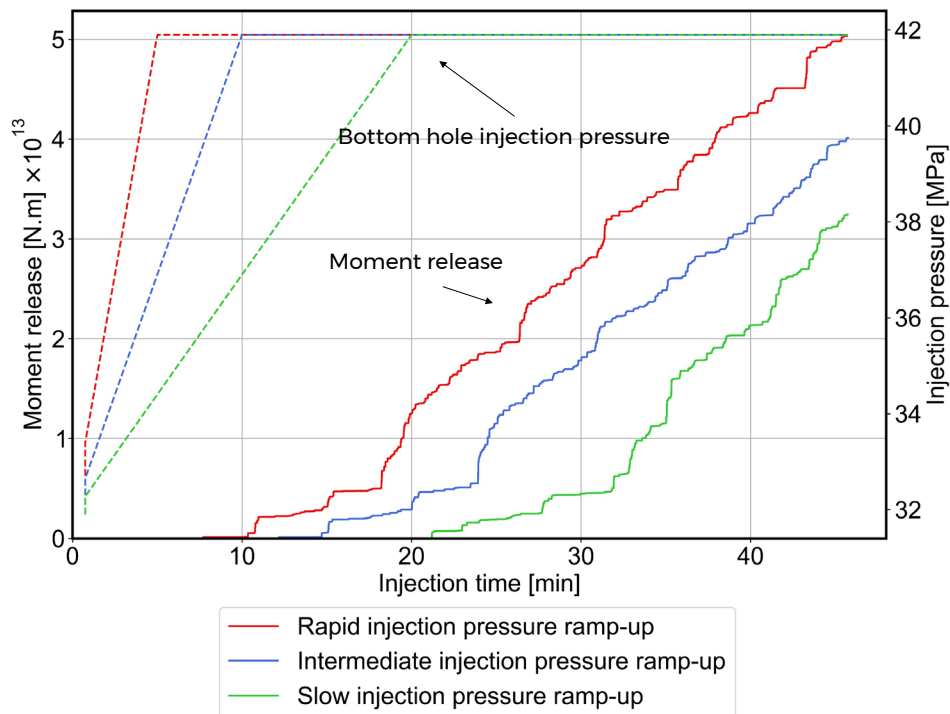


Figure 79: Bottom hole injection pressure and moment release for different injection pressure rates tested using the calibrated model.

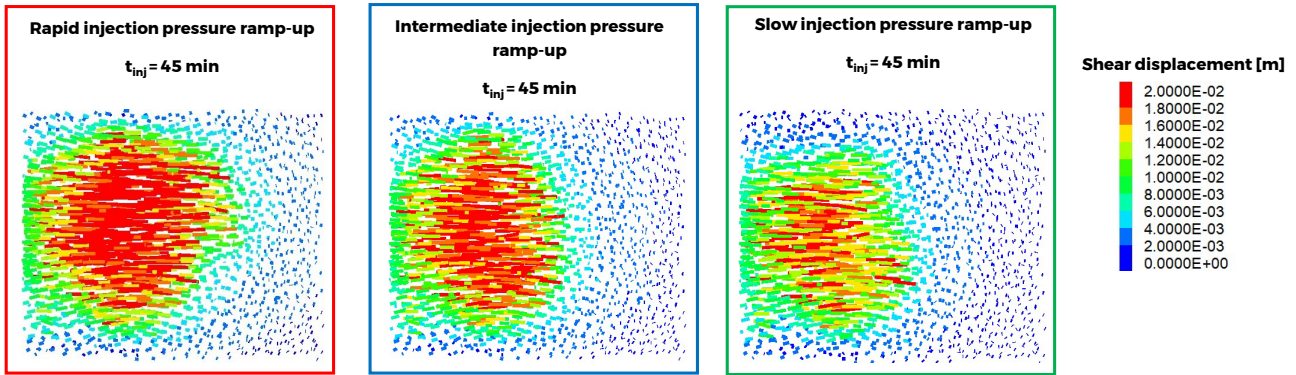


Figure 80: Plan view of the shear slip magnitudes on the seismogenic structure after 45 minutes of fluid injection for the different injection pressure rates tested using the calibrated model.

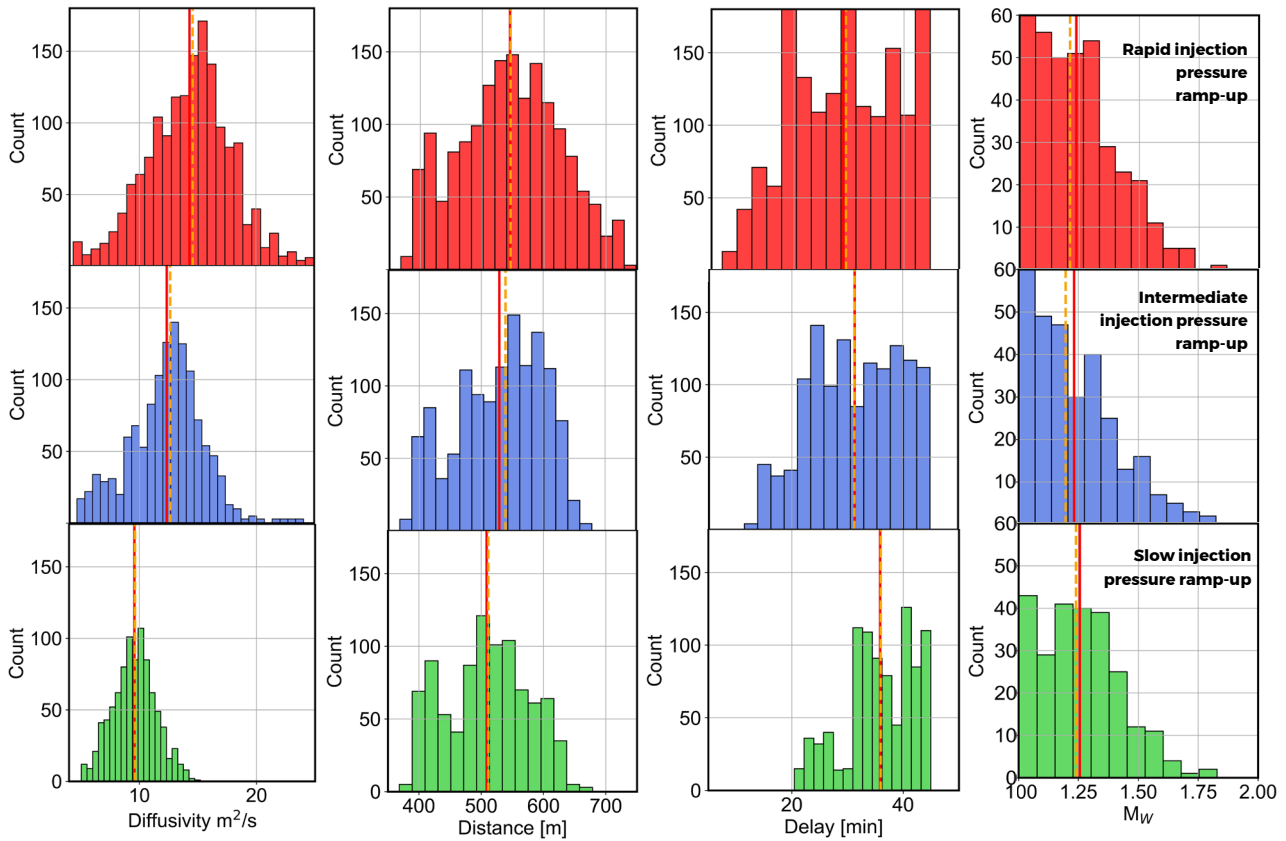


Figure 81: Results for the rapid (top row), intermediate (middle row) and slow (bottom row) injection pressure ramp-up rates, showing from left to right, hydraulic diffusivity, hypocenter distance from injection source, event occurrence delay since the injection start, and seismic event magnitude distribution. The solid red and dashed orange lines indicate the mean and median values, respectively.

Figure 82 presents a conceptual interpretation of the seismic response mechanism to the pressurization rate. We consider two cases: one with a high pressurization rate, HPR (or rapid injection pressure ramp-up) and the other with a low pressurization rate, LPR (or slow pressure ramp-up). The bottom of the illustration shows a pressure-time curve where the injection reaches the final designed injection pressure (P_{inj}) at time t_R for HPR and t_S for LHR. We can assume $t_S = 4 t_R$. The same fluid volume is injected into the same vertical fault but with different patches of shear strength heterogeneity on along the fault. These represent differences in asperities, geometric irregularities or rock bridges encircled and labelled as high (h), intermediate (i), and low (l) shear strength, respectively. The injected fluid pressure distribution at time t_{inj} is shown by the transparent red colour superimposed on the fault in the middle schematic. The grey curve shows the starting point of the pressure gradient front, and the intensity of the red colour illustrates the pressure gradient (from red being the highest to white being the lowest). The pressure gradient front length is proportional to the time taken for each injection scenario to ramp-up and reach P_{inj} from the initial reservoir pressure, P_{iny} . We assume the shear strength patches fail once the corresponding pressure perturbation reaches them and exceeds their respective strengths. For this, if the pressure perturbation is defined by $\Delta P = P_{inj} - P_{iny}$, then we assume H, I, L patches fail at ΔP , $0.5 \Delta P$, and $0.25 \Delta P$, respectively. Looking at the middle schematic and comparing the HPR and LHR fluid pressure front cases, one can see that the short and sharp (i.e., intense) pressure gradient front of the HPR case causes the shear strength patches to fail over a relatively shorter time span in a back-to-back manner. This is able to cause a cascading co-seismic growing event, the clustered ruptured area for which, is shown in the top illustration enclosed by the blue dashed line. Whereas for the case of the LHR, due to its longer gradual pressure gradient front buildup, the shear strength patches fail more gradually with a delay between the seismic events. Hence, this results in the occurrence of two smaller, separated shear rupture areas. Overall, these point to the fact that when the fluid injection pressure gradient front is longer and less intense (more gradual), the stored elastic energy may be released gradually in the form of many smaller events instead of fewer large events. The latter point to the potential for clustered or co-seismic events, and consequently a larger shear rupture area and shear displacement.

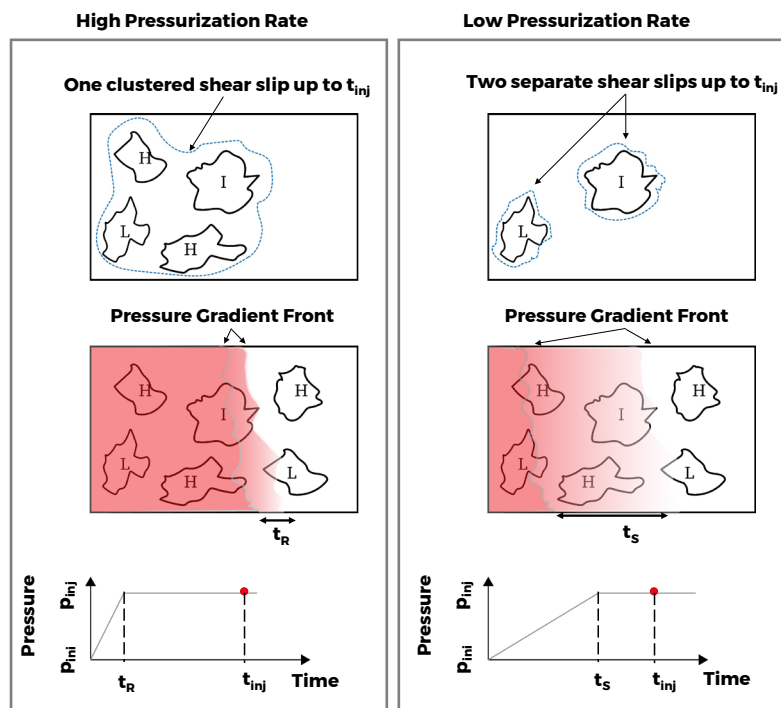


Figure 82: Schematic illustration of the pressurization rate and its effect on seismic energy response along a vertical fault. The graphs on the bottom show the injection ramp-up from initial pressure, P_{iny} , to the targeted injection pressure, P_{inj} , for rapid and slow pressurization rates.

6.3.5 The Impact of Fluid Viscosity on Seismicity

Based on the previous analyses, the results suggest that reservoirs with low fracture intensities are more susceptible to larger magnitude induced seismicity events. This relates to conditions where the structures present have limited or partial hydraulic connectivity, resulting in a higher hydraulic diffusivity directing a more intense pressure perturbation to distal seismogenic structures (see Section 4.4). Recalling Eq. (4) (see Section 4.1), a sensitivity analysis was performed on the hydraulic diffusivity value using XSite™, assuming a given permeability of 10⁴ mD and a fracture porosity of 10% (see Section 4.2 for more details). In addition, we further considered different system compressibility values as well as fluid viscosities. By doing so, we can understand the impact of each parameter on the overall hydraulic diffusivity.

Figure 83 illustrates the XSite™ sensitivity analysis results for hydraulic diffusivity by changing the compressibility and viscosity of the fluid. Note that in Eq. (4), the total compressibility of the system is dependent on the injection fluid, initial saturating fluid in the fracture, and the compressibility of the fracture itself. For the sensitivity analyses carried out, we use as end members the compressibility of gas and water under typical reservoir conditions for the WSCB. Keeping the compressibility of the system constant and varying the viscosity of the saturating fluid in the fracture, one can see by comparing the intersection of each fluid viscosity curve with the overall compressibility in Figure 83 (indicated by red circles), that as the viscosity increases, the overall diffusivity value decreases. Higher viscosities can be achieved by increasing the concentration of certain additives to the fracking fluid (e.g., viscosifying friction reducers). This could potentially decrease the possibility of the pressure perturbation front traveling farther past the designed hydraulic fracturing zone.

Similarly, if fixing the viscosity of the fluid to 1 cP (blue curve in Figure 83) and varying the compressibility of the system from pure water (blue dashed line) to the overall compressibility of the system (black dashed line), the hydraulic diffusivity value (shown by green triangles) decreases as the system becomes more compressible. This may equate to the injection of gases into the reservoir or a mixture of gas and fracking fluid. However, since current hydraulic fracturing practices favour using slick water, adding additives for the purpose of increasing the fracking fluid viscosity to potentially reduce seismicity is likely more feasible than altering the compressibility of the system by gas injection.

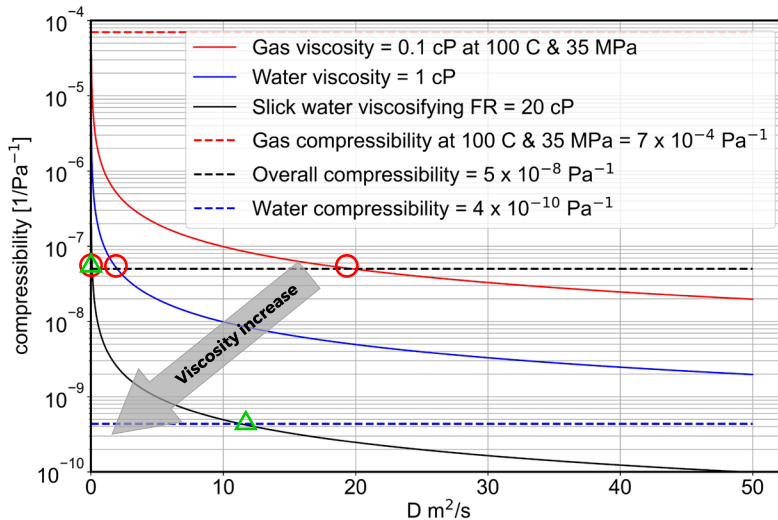


Figure 83: Sensitivity of hydraulic diffusivity in parameter space for the given fracture permeability and porosity of 10⁴ mD and 10%, respectively. FR stands for “Friction Reducer” additive. Red circles compare the diffusivity values by fixing the compressibility of the system (5x10⁻⁸ Pa⁻¹; see black dashed line) and varying the viscosity. Green triangles show the diffusivity values for keeping the viscosity constant (20 cP; see solid black curve) and changing the compressibility.

To further study the effect of injection fluid viscosity on the seismic response of the modelled reservoir, we employed the XSite™ model calibrated to stage 12 from OP3’s well A2 (see Section 6.3.3). Using the base model with a fluid viscosity of 1 cP, we used the same model and only changed the viscosity of the injected fluid to intermediate (30 cP) and high (60 cP) values. Figure 84 illustrates the bottom hole injection pressure and the corresponding cumulative seismic moment releases for each case. These show the injection of a more viscous fluid resulting in a higher-pressure buildup around the injection source. At the same time, the seismic moment release is considerably smaller. In fact, by comparing the shear slip and the pressure front propagation along the seismogenic structure, one can see that despite the larger bottom hole pressures and related pressure gradient in the fracture network, the flow impedance does not allow the fluid pressure front to reach distal structures. This avoids reducing the effective strength and triggering shear slip in areas beyond the designed hydraulic fracturing zone. This is shown clearly in Figure 85 and Figure 86 where the shear slip and the pressure fronts are shown after 25 and 45 minutes of injection time, respectively. These figures show that increasing the viscosity of the injection fluid significantly reduces the pressure perturbation front propagation, which in turn reduces the shear slip and seismic moment release. The effect of viscosity is also clearly reflected in the hydraulic diffusivity, radial distance, and delay time in Figure 87. As shown in Figure 83, the hydraulic diffusivity significantly decreases with an increase of viscosity. Moreover, the number of events and their magnitude are considerably smaller, which suggest that higher viscosity injection fluids could potentially reduce the seismic response and hazard.

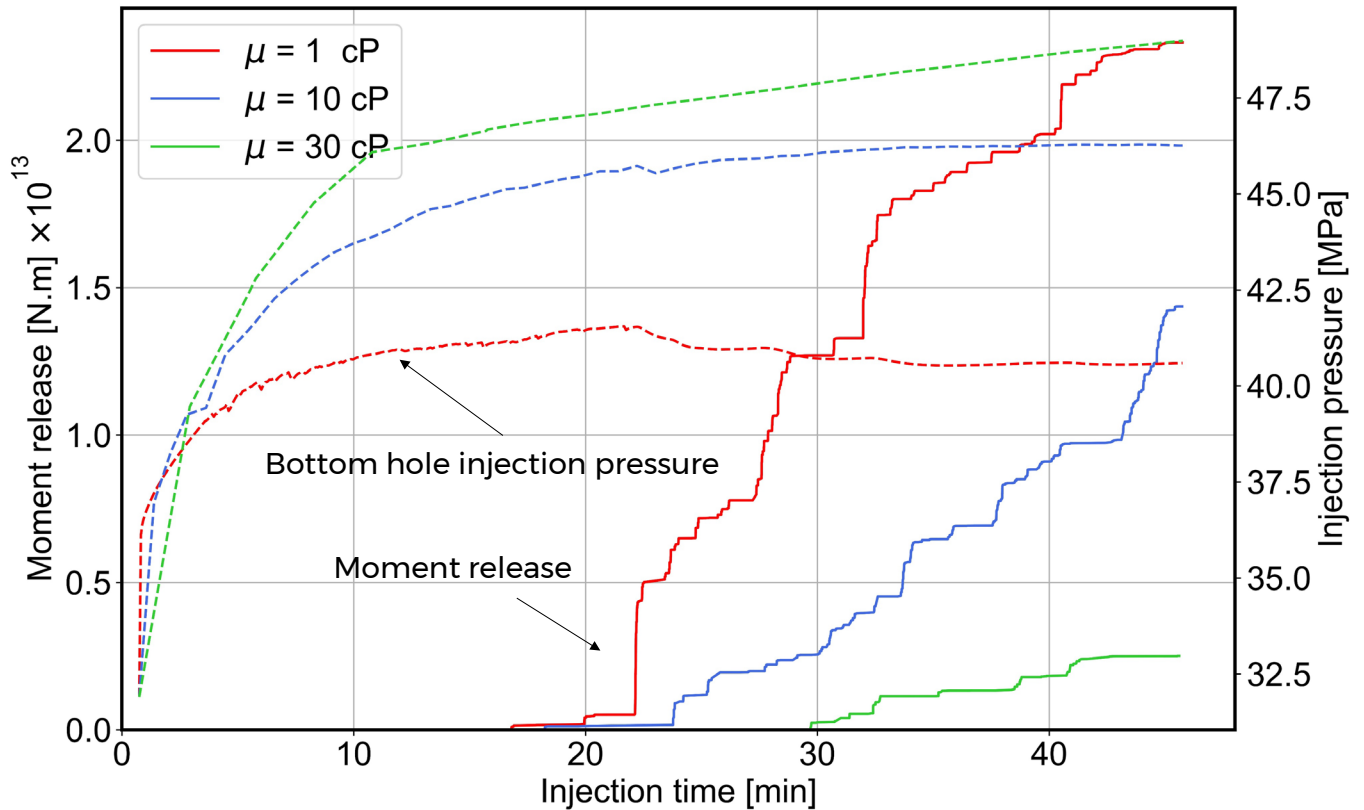


Figure 84: Bottom hole injection pressure and moment release for the injection fluid viscosity sensitivity analysis using the XSite™ calibrated model.

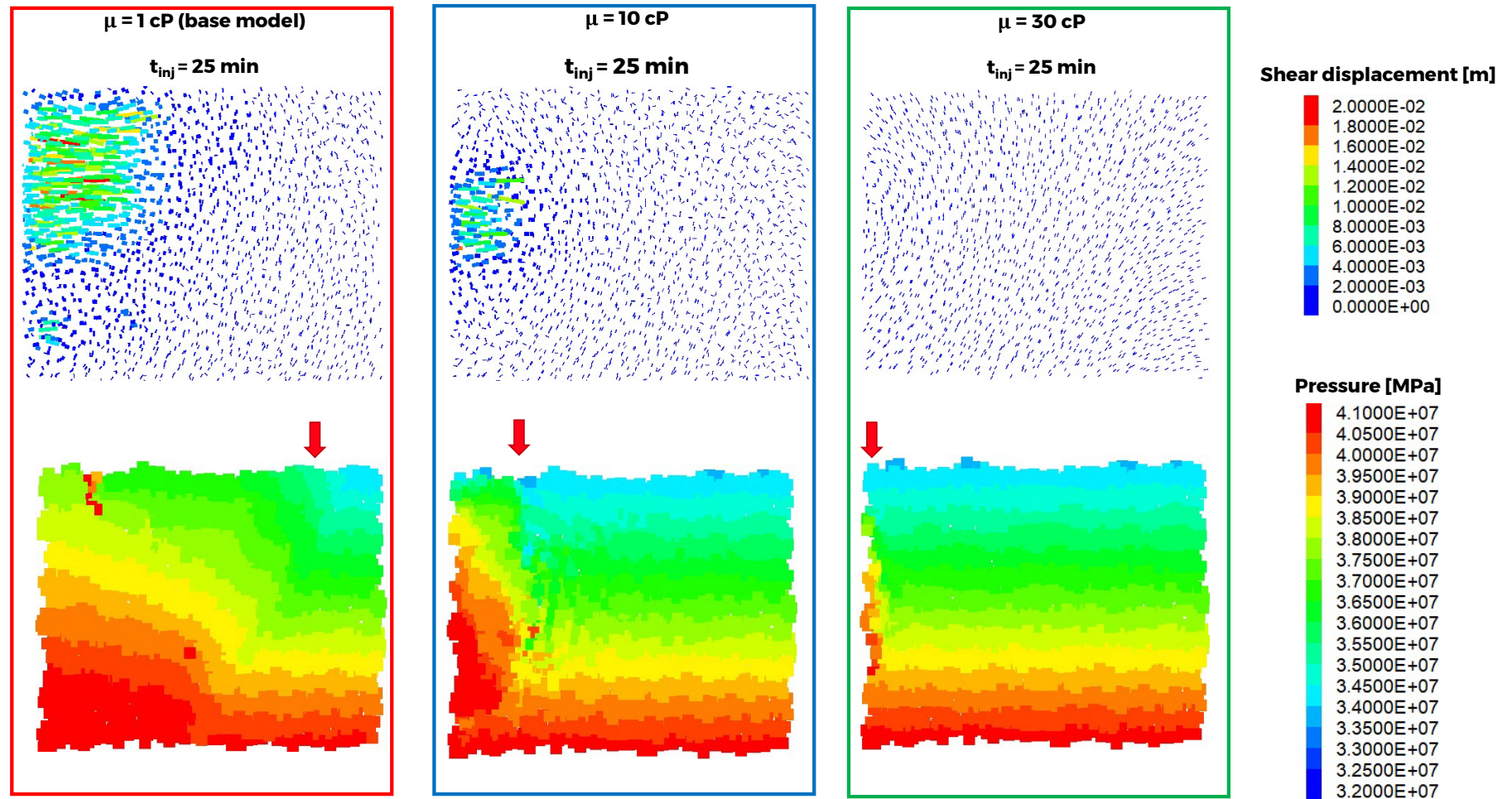


Figure 85: Plan view of the shear slip magnitude (top row) and pressure (bottom row) on the fault after 25 minutes of fluid injection for scenarios based on the XSite™ calibrated model using different injection fluid viscosities. The red arrows show the pressure front location.

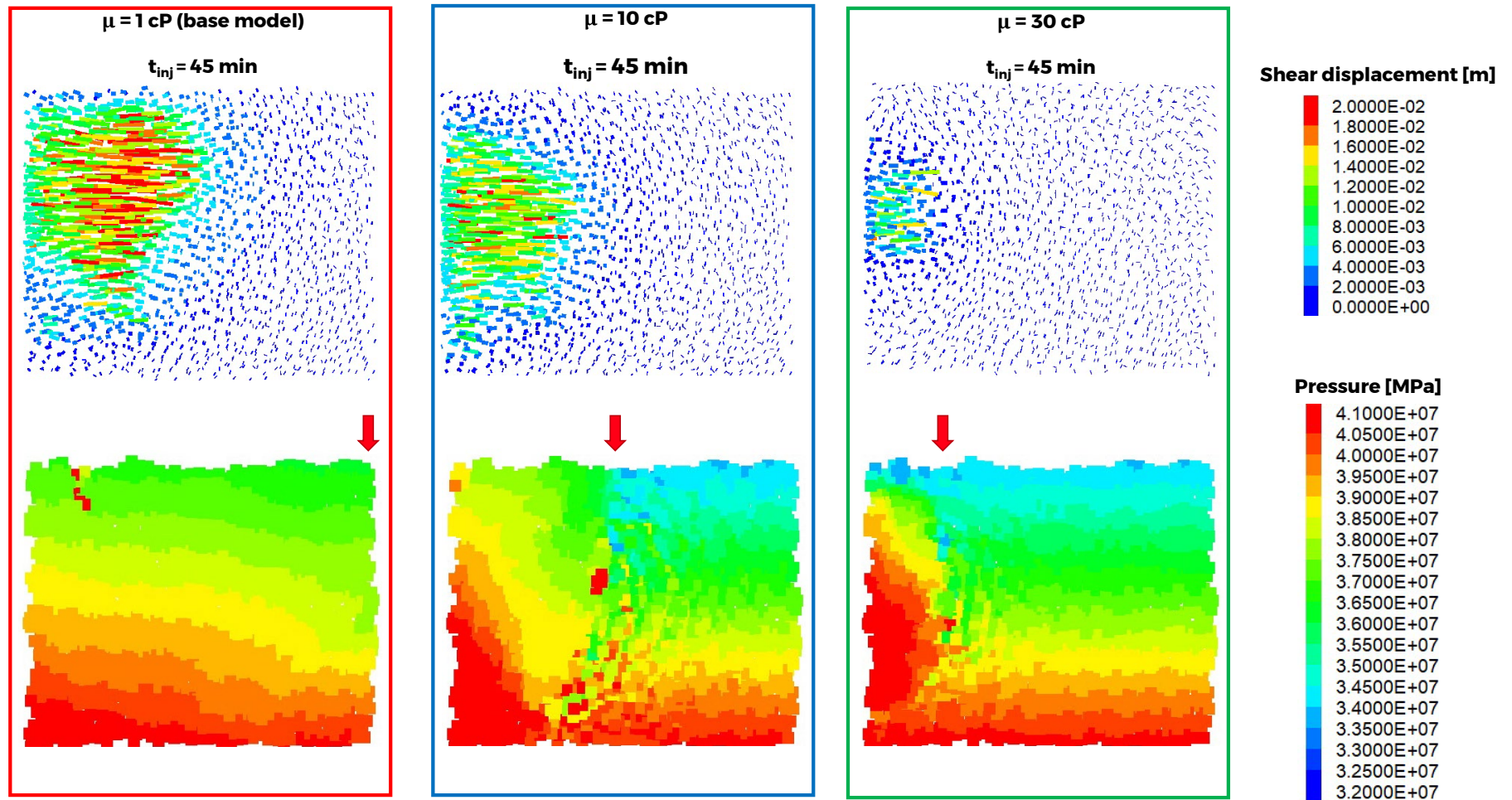


Figure 86: Plan view of the shear slip magnitude (top row) and pressure (bottom row) on the fault after 45 minutes of fluid injection for scenarios based on the XSite™ calibrated model using different injection fluid viscosities. The red arrows show the pressure front location.

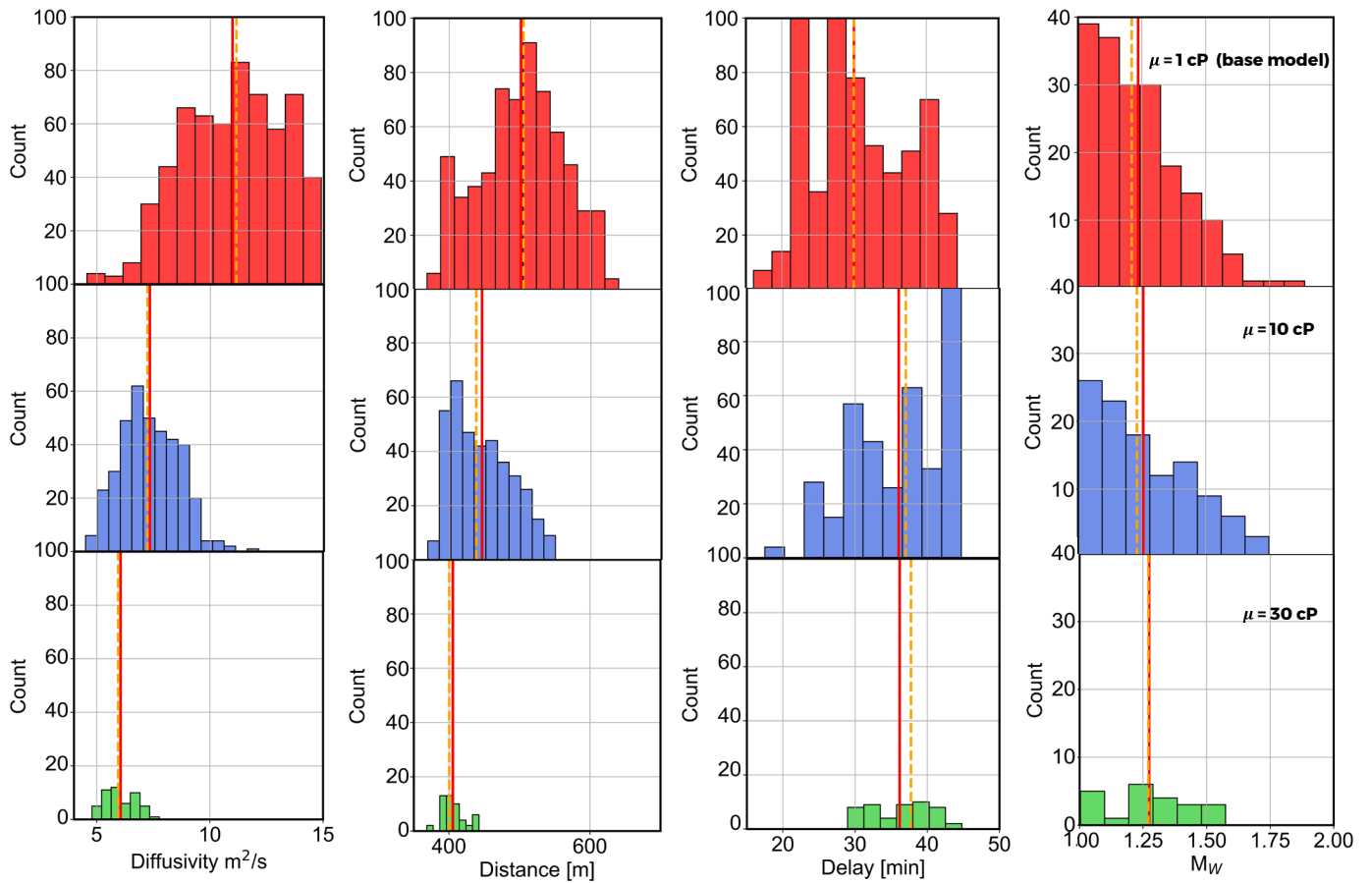


Figure 87: Results testing different injection fluid viscosities using the calibrated base model, showing from left to right, hydraulic diffusivity, hypocenter distance from injection source, event occurrence delay since the injection start, and seismic event magnitude distribution. The solid red and dashed orange lines indicate the mean and median values, respectively.

7.0 KEY LEARNINGS & CONCLUSIONS

The key learnings from this study have been summarised by section below.

Structural Connectivity

- Analysis of the induced seismic data from OP3 shows that seismogenic structures (structures imaged by induced events) identified in the Lower Montney can be processed to infer their geometric properties.
- The exact nature of these structures is not possible to derive, but it is likely given their size, that they most likely represent faults. However, given this uncertainty, discontinuity is a better term.
- Within the OP3 data set, direct evidence from connection paths between events and active stage, points to both a seismic NE-SW fracture set and also an aseismic NW-SE fracture set.
- The use of “aseismic structure” within this work refers to structures that may conduct fluid and or pressure, but either show no or low levels/magnitudes of induced seismicity, relative to the main critically stressed set, with its broadly NE-SW trend.
- The identified structures have a minimum length of approximately ~50 m, with modelling suggesting that below this, the inferred connectivity of the fracture network becomes too high to explain the pattern of induced events. Both datasets show a range of structure lengths in the range of 50-600m.
- The length distribution of interpreted structures from both OP1 and OP3 pads both show very similar power law distributions and intensities, and it is thought that this common size distribution may be a characteristic of the seismically active KSMMA area.
- By reproducing the observed and inferred structures and identifying those structures that connect back to active stages, the observed length of seismogenic faults (NE-SW fracture set) can be matched, with the distance of simulated and actual seismic events from the well showing very good agreement.
- This connectivity analysis (without any actual flow simulation) provides direct evidence for the importance of reservoir structures carrying pressure over considerable distance.
- Pressure contained within these highly diffusive structural elements can result in the reactivation of structures and the generation of seismic events when their shear failure criteria is exceeded.
- In the OP3 data set, there appears to be a relatively strong isolation between the Upper Montney and the Middle/Lower Montney, with virtually no seismicity generated from the upper Montney wells. This is structurally consistent with the observations of Rogers 2018.
- The OP1 data set shows an example where a more sensitive seismic array allowed the more accurate mapping of illuminated reservoir structures through the whole Montney Formation. These identified pressure diffusion pathways can be reasonably mapped between the active pumping stages and events with reasonable confidence.
- Like the OP3 data set, there is a clearly dominant NE-SW structural set with minor NW-SE and NNE-SSW sets. It is important to understand that as the NE-SW set is the most seismically susceptible, it's possible the relative intensity of the different sets may be influenced by this detection bias on the less susceptible structures.

- Interpretation of the induced events from OP1 allowed the generation of both deterministic structures associated with high magnitude events and also the definition of the geometric properties of small structures, associated with smaller magnitude events, that could be generated stochastically. The larger deterministic structures had a minimum length of ~100 m, with the stochastic structures being generated in the 40-100 m long structure range. These properties are quite similar to those derived for the OP3 dataset.
- By searching the DFN network for structures that connect to the wells and adjusting the threshold for the number of fracture connections away from the well, it was found that the connected networks of structures surrounding each well were consistent with the distribution of induced seismic events associated with that well. Like the OP3 analysis, this provides strong evidence for the role of connected structure pathways for pressure diffusion and fault reactivation.
- In contrast to OP3 dataset, the OP1 dataset shows induced seismicity from wells drilled in the Upper Montney, with a considerable number of events being generated within the Middle and Lower Montney. It has often been assumed that seismicity is primarily associated with the Lower Montney.
- The vertical connectivity of the OP1 pad is very different to OP3 where there was only limited apparent connection between the Middle Montney and the Upper Montney. In contrast, all the Upper Montney wells induced seismicity in the Middle, Lower and to some extent, the Bellboy. This represents two distinctive fracture architectures between these two pads.

Hydraulic Diffusivity

- Analysis of the induced seismic events in terms of their straight-line distance from an active stage and the time taken for a triggering pressure to arrive at that location allows the hydraulic diffusivity of that pathway to be determined, providing insight into the characteristics of reservoir scale fractures within the Montney Formation.
- For the hydraulic diffusivity analysis, it is not possible to determine the exact triggering pressure as it is a function of many different parameters. However, we believe that a pressure increase in the order of 1 MPa is a reasonable approximation.
- The range of hydraulic diffusivity values calculated is consistent with those reported elsewhere from fractured reservoir and fracture aquifer studies where pressure pulses have been measured over some distance. The majority of smaller events have a diffusivity of <5 m²/s with the larger magnitude events typically being in the range of 5-15 m²/s. A small number of events are found in the 20–25 m²/s range.
- Injection of pressurised water into a partially connected network of structures (i.e., relatively few) resulted in a high hydraulic diffusivity characterised by rapid pressure diffusion, a higher-pressure build-up and the potential for a large seismic event.
- In contrast, injection into a higher intensity of structures showing higher connectivity resulted in a lower hydraulic diffusivity, characterised by slower pressure diffusion, a lower build-up of pressure and typically the release of seismic energy through a higher number of smaller events.
- This is seen clearly when the number structures (indirectly) connected to a stage, the diffusivity associated with the pathways mapped by the events and their associated magnitudes are considered. All of the largest events are associated with fewer stage connections.

- Hydraulic diffusivity derived permeability and aperture values give average fracture kh (transmissivity) values of the order 1-10 mD.m. In the data from the open hole completion appears to give higher values with the peak kh in the order of 1000 mD.m. All of these values are consistent with fracture kh (permeability x aperture) values experienced in conventional fractured reservoir systems. These observations were further confirmed by simple simulation of injection into a long single fracture with regularly spaced observation wells. Hydraulic properties used in the simulation were similar to those derived from the diffusivity analysis.
- The seismic energy efficiency in hydraulic fracture operations is typically less than 10^{-5} , however the data for both operators showed a range of 10^{-4} to 10^{-3} (10 to 100 times higher). These higher observed values are within the range reported for hydro-shearing associated with pressurized injection, specifically targeting pre-existing structures.

FracMan Hydraulic Fracture Simulations

- The FracMan hydraulic fracture simulations for the OP1 pad into the Upper Montney showed that the hydraulic fracture stimulation results in the generation/reactivation of three key elements:
 - Induced hydraulic fractures with a maximum (half) length of ~500 m. These are dependent upon the layer that is stimulated as the lower bank of wells in the lower stress/stiffness layer resulted in the generation of long skinny fracs whereas injection into the higher stress/stiffness layer of the upper bank, results in rounder fracs with a notable downward component. This is consistent with the observed seismicity distribution that showed deeper seismicity associated with the higher bank of Upper Montney wells. This suggests that the downward driving fracs are consistent with vertical pressure communication.
 - A subset of the interpreted structures show that they can receive fluid directly and are known as inflated natural structures. These structures are typically NE-SW, with an orientation close to SHmax, with limited closure stresses on them.
 - The majority of the seismicity appears to be associated with structures connected back to the well, that receive pressure (but not fluid) from the main hydraulic fracture or inflated natural structures. This elevated pressure takes fractures from “close to”, to critically stressed structures by inducing stresses that exceed a Mohr-Coulomb failure criteria, resulting in shear slip.
- The FracMan hydraulic fracture simulations for the OP3 pad showed that the stimulation is comprised of two key elements:
 - Induced tensile fractures with a maximum length of ~500 m and a limited height in order of approximately 20 m high, contained within a relatively lower stress zone.
 - The majority of the seismicity appears to be associated with structures connected back to the well, that receive pressure from the main hydraulic fracture or inflated natural structures. For this data set, only NE-SW structures are seismogenic, with the inferred NW-SW structures aseismic. This is believed to be because they are probably normal to SHmax and therefore will experience high normal stresses and a resultant low susceptibility to shear slip.
 - However, the NW-SE structures are needed to provide network connectivity and so whilst these structures may be aseismic, it is believed that they have preserved permeability despite the high normal stresses.
 - Unlike the OPA dataset, none of the mapped structures resultant in direct fracture inflation as their orientation is too far from SHMax, resulting in high closure stresses.

Mitigation of Induced Seismicity

- Stochastic DFN simulations were carried out to see if switching from open hole to cased hole completions could reduce connectivity to the wider reservoir structures. However, these tests suggest that in the scenario modelled, connectivity was dominated by hydraulic fracture length, with increasing frac length correlating to an increase in network connection.
- Additionally, it was found that using the calibrated fault intensity properties from OP3, resulted in an average of ~12 structures >100 m long intersecting the three Lower Montney wells. Considering a cased hole resulted in effectively no structures connecting directly with well.
- Whilst there is insufficient evidence to recommend not using open hole completions, there is sufficient anecdotal information to encourage further investigation of completion type on seismicity. It is recommended that the BCER (BC Energy Regulator) maintains a database on event distance from active stage and also magnitude distribution, such that a comparison can be made between completion types in the future.
- A number of potential mitigation options were tested through XSite numerical simulations:
 - Injection Rate: Numerical simulation studies suggest that higher injection rates can result in higher induced events magnitude. Lowering the injection rate can instead cause the seismic moment release in the form of many small events.
 - Variable Injection Rate: Numerical modeling shows that varying the pumping rate during the injection resulted in a larger seismic energy release. However, this is more likely due to consequent pressure pulses. Such injection rate alterations and pressure pulses are more common during open hole completion.
 - Pressurisation Rate: Simulation analyses revealed that the pressurization rate of the fracture showed a significant impact on the seismicity response of the reservoir. This agrees with the laboratory studies and numerical simulation studies of the water impoundment induced seismicity.
 - Fluid Viscosity: Numerical simulation of increasing frac fluid viscosity could potentially decrease the potential seismic hazard and reduces the fluid pressure propagation to unfavorable areas outside the designed HF zone.

Key Residual Uncertainties

There are a number of key uncertainties:

- The depth location of the OP3 seismic event catalogue was somewhat uncertain. The events have been placed largely in the Lower Montney based on which wells were active at the time.
- With the numerical simulation results presented in this study, it was found that the increase of fluid viscosity may reduce the seismic potential of the system. However, this result is limited to the assumptions and capabilities of the numerical simulators used in this study. The numerical simulators in this study (3DEC and XSite) are not fully capable of simulating the two-phase fluid flow. These initial promising results indicate that this should be studied further with other simulators designed for such applications. However, this observation is consistent with anecdotal unreported field observations.
- The data received operators is considered reliable. No attempts have been made to verify third party interpretations.
- The analysis and modelling within this report has been carried out to understand patterns and processes, rather than specifically reproduce the exact performance of a well. The report should be interpreted as such.

8.0 RECOMMENDATIONS FOR FUTURE WORK

A number of areas of work are recommended for further study.

- 1) **Can we predict maximum event magnitude?** Based on the analysis contained within this report, key geometric characteristics of the seismogenic structures have been constrained and found to be largely consistent between the two pads. Further work is recommended to explore these geometric properties and how they relate to observed event magnitude distributions and in particular max event magnitudes. This will need to also consider variations in insitu stresses and stiffnesses.
- 2) **What controls or influences the Montney vertical connections? Can they be influenced or avoided?** Further work is recommended to better understand the reservoir scale structural geology of the seismically susceptible fault systems present in KSMMA, with a view to improving the predictability of pre-stimulation risk assessment and analysis. As part of this, further study is also needed to better understand vertical connectivity patterns in the Montney and how the Montney layers are structurally connected
- 3) **Can we better characterise Montney structures using hydraulic diffusivity?** The use of hydraulic diffusivity to characterise reservoir flow paths has proved highly useful. It is recommended that this is taken further with flow simulations being used to better calibrate hydraulic properties and to better understand how the isotropic diffusivity results relate to the highly anisotropic fracture system. Additionally, methodologies should be developed to allow the constant calculation of diffusivity values from hydraulic fracturing to allow a constant reporting framework.
- 4) **In-depth comparison of open-hole and cased hole completions and the influence on IS.** Further work comparing open hole v cased hole completions should be considered. Whilst this work showed similar results with the two completion types, anecdotal experience suggests that case hole completions do provide a more controlled stimulation environment. This should be explored further.
- 5) **Confirming completion fluid viscosity mitigations and other options for similar frac ops mitigations.** Preliminary geomechanics modelling showed that increasing fluid viscosity reduced the seismic hazard. This is supported by anecdotal field observations. Further modelling with fully coupled multi-phase flow simulations to better capture the physics of the system and constrain the range of useful viscosity adjustments. Other operational mitigation strategies should be considered further as well.

9.0 CLOSURE

The reader is referred to the Study Limitations section (after Executive Summary), which precedes the text and forms an integral part of this report.

If you have any questions or comments, please contact the undersigned.

9.1 Collaboration

This work was carried out in collaboration with a research team at the University of British Columbia (UBC). The following individuals contributed extensively to the investigations in this study:

- Dr. Erik Eberhardt, P.Eng (BC) – Research Advisor
 - Professor of Geological Engineering/EOAS, University of British Columbia
- Ali Mehrabifard – Researcher
 - PhD Candidate of Geological Engineering/EOAS, University of British Columbia

Signature Page

WSP Canada Inc.



Ciara Byrne
Senior Geological Consultant



Steve Rogers, P. Geo (BC)
Senior Principal Geoscientist



12th May 2023

CB/SR/AM/hp/ss/anr

[https://goldeassociates.sharepoint.com/sites/163566/project files/6 deliverables/02_issued/2252864-005-r-rev0-1000 final report - public/2252864-005-r-rev0-1000-ksmma final report 12may_23.docx](https://goldeassociates.sharepoint.com/sites/163566/project%20files/6%20deliverables/02_issued/2252864-005-r-rev0-1000%20final%20report%20-%20public/2252864-005-r-rev0-1000-ksmma%20final%20report%2012may_23.docx)

PERMIT TO PRACTICE #1000200
Engineers & Geoscientists BC

REFERENCES

- Amini, A., & Eberhardt, E. (2019). Influence of tectonic stress regime on the magnitude distribution of induced seismicity events related to hydraulic fracturing. *Journal of Petroleum Science and Engineering*, 182(June 2019). <https://doi.org/10.1016/j.petrol.2019.106284>.
- Amini, A., Eberhardt, E., Rogers, S., Venables, S., & Gaucher, M. (2022). Empirical and numerical investigation into the influence of fluid injection volume and rate on induced seismicity in the Montney Formation, northeastern British Columbia. *Journal of Petroleum Science and Engineering*, 213(January), 110423. <https://doi.org/10.1016/j.petrol.2022.110423>.
- Babadagli, T., Raza, S., Ren, X., & Develi, K. (2015). Effect of surface roughness and lithology on the water–gas and water–oil relative permeability ratios of oil-wet single fractures. *International Journal of Multiphase Flow*, 75, 68–81. <https://doi.org/10.1016/J.IJMULTIPHASEFLOW.2015.05.005>.
- BC Oil and Gas Commission (2018): Order 18-90-001 (Amendment #2) – Kiskatinaw Seismic Monitoring and Mitigation Area Special Project Order; BC Oil and Gas Commission. Report 2021. 11p.
- Biot, M. A. (1962). Mechanics of deFormation and acoustic propagation in porous media. *Journal of Applied Physics*, 33(4), 1482–1498. <https://doi.org/10.1063/1.1728759>.
- Cesca, S., Stich, D., Grigoli, F., Vuan, A., López-Comino, J. Á., Niemz, P., ... Ellsworth, W. L. (2021). Seismicity at the Castor gas reservoir driven by pore pressure diffusion and asperities loading. *Nature Communications 2021 12:1*, 12(1), 1–13. <https://doi.org/10.1038/s41467-021-24949-1>.
- Chen, Y. F., Wu, D. S., Fang, S., & Hu, R. (2018). Experimental study on two-phase flow in rough fracture: Phase diagram and localized flow channel. *International Journal of Heat and Mass Transfer*, 122, 1298–1307. <https://doi.org/10.1016/J.IJHEATMASSTRANSFER.2018.02.031>.
- Dershowitz, W.S & Herda, H.H 1992. Interpretation of fracture spacing and intensity. : ARMA-92-0757.
- Eyre, T.S., Eaton, D.W., Garagash, D.I., Zecevic, M., Venieri, M., Weir, R. and Lawton, D.C., 2019. The role of aseismic slip in hydraulic fracturing–induced seismicity. *Science advances*, 5(8).
- Damjanac, B., Detournay, C., & Cundall, P. (2020). Numerical Simulation of Hydraulically Driven Fractures. In *Modelling Rock Fracturing Processes* (pp. 531–561). Springer International Publishing. https://doi.org/10.1007/978-3-030-35525-8_20.
- Fox, A. McKean, N. Watson 2019. Statistical Assessment of Operational Risks for Induced Seismicity from Hydraulic Fracturing in the Montney, Northeast BC. Geoscience BC Report 2020-12.
- Gasparrini, M., Lacombe, O., Rohais, S., Belkacemi, M. and Euzen, T., 2021. Natural mineralized fractures from the Montney-Doig unconventional reservoirs (Western Canada sedimentary basin): Timing and controlling factors. *Marine and Petroleum Geology*, 124.
- Goebel, T. H. W., & Brodsky, E. E. (2018). The spatial footprint of injection wells in a global compilation of induced seismic event sequences. *Science*, 361(6405), 899–904. https://doi.org/10.1126/SCIENCE.AAT5449/SUPPL_FILE/AAT5449_GOEBEL_DATA-S1.XLSX.
- Hummel, N., & Shapiro, S. A. (2013). *Analysis and Interpretation of Hydraulic Fracturing Induced Seismicity From the Horn River Basin*.

- Igonin, N., Verdon, J. P., Kendall, J. M., & Eaton, D. W. (2021). Large-Scale Fracture Systems Are Permeable Pathways for Fault Activation During Hydraulic Fracturing. *Journal of Geophysical Research: Solid Earth*, 126(3). <https://doi.org/10.1029/2020JB020311>.
- Jaeger, J. C., Cook, N. G. W., & Zimmerman, R. W. (2007). *Fundamentals of rock mechanics* (4th ed.). Blackwell Pub.
- Odling, N.E., 1997. Scaling and connectivity of joint systems in sandstones from western Norway. *Journal of Structural Geology*, 19(10), pp.1257-1271.
- Riazi, N., Eaton, D.W., Aklilu, A. and Poulin, A., 2020. Application of focal-time analysis for improved induced seismicity depth control: A case study from the Montney Formation, British Columbia, Canada. *Geophysics*, 85(6), pp. KS185-KS196.
- Rogers, S., Moffitt, K.Mm, & Kennard, D.T. 2006. Probabilistic slope and tunnel block stability analysis using realistic fracture network models. ARMA 06-1052
- Rogers, S., McLellan, P. and Webb, G., 2014, October. Investigation of the effects of natural fractures and faults on hydraulic fracturing in the Montney Formation, Farrell Creek Gas Field, British Columbia. In International Discrete Fracture Engineering Conference, Vancouver.
- Rogers, S., 2018. What can discrete fracture network analysis tell us about induced seismicity in the Montney Formation? GeoConvention abstract.
- Rogers, S., Cottrell, M., Hughes, R., Squires, C. 2020. Using Discrete Hydraulic Fracture Simulations to Inform Stimulation Optimization in the Montney. GeoConvention abstract.
- Salvage, R.O., Dettmer, J., Swinscoe, T.H.A., MacDougall, K., Eaton, D.W., Stacey, M., Aboud, M., Kang, T.S., Kim, S. and Rhie, J., 2021. Real-time monitoring of seismic activity in the Kiskatinaw area, northeastern British Columbia (NTS 093P, 094A). *Geoscience BC Summary of Activities 2020: Energy and Water*, Geoscience BC, Report 2021, 2, pp.17-30.
- Scholz, C. H. (2019). *The Mechanics of Seismic events and Faulting* (3rd ed.). Cambridge University Press. <https://doi.org/10.1017/9781316681473>.
- Sequent 2023. Leapfrog Geo modelling software.
- Shapiro, S. A., Audigane, P., & Royer, J. J. (1999). Large-scale in situ permeability tensor of rocks from induced microseismicity. *Geophysical Journal International*, 137(1), 207–213. https://doi.org/10.1046/J.1365-246X.1999.00781.X/2/M_137-1-207-EQ021.JPEG.
- Shapiro, S. A., Huenges, E., & Borm, G. (1997). Estimating the crust permeability from fluid-injection-induced seismic emission at the KTB site. *Geophysical Journal International*, 131(2), F15–F18. <https://doi.org/10.1111/J.1365-246X.1997.TB01215.X>.
- Shapiro, S. A., Rothert, E., Rath, V., & Rindschwentner, J. (2002). Characterization of fluid transport properties of reservoirs using induced microseismicity. *Geophysics*, 67(1), 212–220. <https://doi.org/10.1190/1.1451597>.
- Talwani, P., & Acree, S. (1985). Pore Pressure Diffusion and the Mechanism of Reservoir-Induced Seismicity. *Seismic event Prediction*, 122, 947–965. https://doi.org/10.1007/978-3-0348-6245-5_14.

- Talwani, P., Chen, L., & Gahalaut, K. (2007). Seismogenic permeability, ks. *Journal of Geophysical Research: Solid Earth*, 112(B7), 7309.
- Vishkai, M. and Gates, I.D., 2018, June. Geomechanical Characterization of Naturally Fractured Formation, Montney, Alberta. In 52nd US Rock Mechanics/Geomechanics Symposium. OnePetro.
- Wang, L., Kwiatek, G., Rybacki, E., Bonnelye, A., Bohnhoff, M., & Dresen, G. (2020). Laboratory Study on Fluid-Induced Fault Slip Behavior: The Role of Fluid Pressurization Rate. *Geophysical Research Letters*, 47(6). <https://doi.org/10.1029/2019GL086627>.
- WSP 2023. FracMan 8.1 Manual.
- Zhang, F., Damjanac, B. and Maxwell, S., 2019. Investigating hydraulic fracturing complexity in naturally fractured rock masses using fully coupled multiscale numerical modeling. *Rock Mechanics and Rock Engineering*, 52(12), pp.5137-5160.

wsp

wsp.com